

Non-Linear Scale Interactions in a Forced Turbulent Boundary Layer

Thesis by

Subrahmanyam Duvvuri

In Partial Fulfillment of the Requirements

for the Degree of

Doctor of Philosophy

The logo for the California Institute of Technology (Caltech), featuring the word "Caltech" in a bold, orange, sans-serif font.

California Institute of Technology

Pasadena, California

2016

(Defended January 8, 2016)

© 2016

Subrahmanyam Duvvuri

All Rights Reserved

To my family

तस्याहं निग्रहं मन्ये
वायोरिव सुदुष्करम् ॥

*Its control I consider
as hard as controlling the flowing wind.*

Bhagavad-Gītā 6:34

Acknowledgments

It gives me great pleasure to express my gratitude to the people who helped me in a wonderful journey, the culmination of which is this thesis. First and foremost, I am very thankful to my advisor Beverley McKeon for introducing me to the *fascinating* world of wall turbulence, and her mentorship. The constant support and encouragement I received from her, through the highs and lows of graduate school, is deeply appreciated. I am also thankful to Mory Gharib, Dale Pullin, and Tim Colonius for serving on my thesis committee, and for constructive comments and discussion.

For the last five years I've enjoyed the good company of several members, past and present, of the McKeon group – including Jeff LeHew, Ian Jacobi, Jean-Loup Bourguignon, Rebecca Rought, Rashad Moarref, Mitul Luhar, Reeve Dunne, Esteban Hufstedler, Jonathan Morgan, Kevin Rosenberg, Tess Saxton-Fox, Sean Symon, Simon Tödli, David Huynh, and Ryan McMullen. I've pestered most of them for help with my wind tunnel set up on various occasions that I needed an additional pair of hands in the lab, and they gladly obliged! The research discussions I've had with them, particularly with Rashad and Mitul, gave rise to ideas that eventually played an important role in shaping this thesis. The group administrative assistants, Jennifer Stevenson previously and Jamie Sei at present, have been very resourceful. I am thankful to all the group members for their help and support.

The fine machining of various components of the experimental set up by Joe Haggerty, Ali Kiani, Bradley St. John, and Matt Zargarian at the GALCIT shop, and Merih Eken at the Physics shop greatly aided in the smooth functioning of the experiment; I am thankful to them for their cooperation and help. I am also thankful to Bahram Valiferdowsi for his help with the maintenance of the Merrill wind tunnel, and for ensuring that it remained in good operational condition.

I am grateful to the Resnick Institute at Caltech for their support through a generous graduate fellowship. My association with the institute has been a fruitful one; I am thankful to Neil Fromer and Heidi Rusina at the institute for organizing and coordinating various events for the fellows.

During my time at Caltech, I've received support from many people in ways not directly related to my research work, but was nonetheless essential in enabling it. Among them are Christine Ramirez and Dimity Nelson at GALCIT, Felicia Hunt and Natalie Gilmore at the Graduate Dean's office, and Laura Flower-Kim at the International Students Program; I am thankful to them for all the assistance and help.

I am fortunate to have had some fantastic teachers through my student years. I am thankful to all of them, collectively and individually, for their encouragement and guidance that got me this far. In particular, I would like to express my sincere gratitude to the person I consider to be my *guru* – Prof. Roddam Narasimha. I had the incredible opportunity to work with him during my undergraduate years, and he has taken a keen interest in my progress since then. I will cherish for a long time the discussions we've had, which on many occasions extended well beyond fluid dynamics and into the realms of general science, technology, history, art, politics, and philosophy; I look forward to many more such discussions with him in the years to come! He is a role model to me, and a great source of inspiration.

Lastly, I would like to acknowledge my family – my parents Padmavathi and Venkata Ramana Murthy, my sister Neelima, and my wife Sivani. I am deeply grateful for their love, affection, and support, without which none of this would have been possible.

Abstract

This thesis explores the dynamics of scale interactions in a turbulent boundary layer through a forcing-response type experimental study. An emphasis is placed on the analysis of triadic wavenumber interactions since the governing Navier-Stokes equations for the flow necessitate a direct coupling between triadically consist scales. Two sets of experiments were performed in which deterministic disturbances were introduced into the flow using a spatially-impulsive dynamic wall perturbation. Hotwire anemometry was employed to measure the downstream turbulent velocity and study the flow response to the external forcing. In the first set of experiments, which were based on a recent investigation of dynamic forcing effects in a turbulent boundary layer, a 2D (spanwise constant) spatio-temporal normal mode was excited in the flow; the streamwise length and time scales of the synthetic mode roughly correspond to the very-large-scale-motions (VLSM) found naturally in canonical flows. Correlation studies between the large- and small-scale velocity signals reveal an alteration of the natural phase relations between scales by the synthetic mode. In particular, a strong phase-locking or organizing effect is seen on directly coupled small-scales through triadic interactions. Having characterized the bulk influence of a single energetic mode on the flow dynamics, a second set of experiments aimed at isolating specific triadic interactions was performed. Two distinct 2D large-scale normal modes were excited in the flow, and the response at the corresponding sum and difference wavenumbers was isolated from the turbulent signals. Results from this experiment serve as an unique demonstration of direct non-linear interactions in a fully turbulent wall-bounded flow, and allow for examination of phase relationships involving specific interacting scales. A direct connection is also made to the Navier-Stokes resolvent operator framework developed in recent literature. Results and analysis from the present work offer insights into the dynamical structure of wall turbulence, and have interesting implications for design of practical turbulence manipulation or control strategies.

Contents

Acknowledgments	v
Abstract	vii
1 Background and Motivation	1
1.1 A Brief Historical Sketch of Turbulence	1
1.2 The Turbulent Boundary Layer	3
1.2.1 Mean Flow Description	3
1.2.2 Coherent Flow Structures	4
1.3 Large-Scale Influences and Scale Interactions	5
1.3.1 Evidence of Large-Scale Influences	6
1.3.2 Recent Developments	6
1.4 Forcing-Response Analysis	8
1.4.1 Targeted Forcing of Wall Turbulence	9
1.4.2 Resolvent Operator Framework	10
1.5 Approach	10
2 Experimental Setup	12
2.1 Flat-Plate Boundary Layer Facility	12
2.2 Dynamic Wall Perturbation	14
2.2.1 Single-Frequency Oscillations	15
2.2.2 Double-Frequency Oscillations	16
2.3 Velocity Measurements	17
2.3.1 Hotwire Anemometry and Data Sampling Parameters	18
2.4 Canonical Flow Statistics and Power Spectrum	19
2.4.1 Mean Velocity and Turbulence Intensity	20
2.4.2 Velocity Power Spectrum	21

3	Single-Mode Forcing of the Turbulent Boundary Layer	23
3.1	Flow Statistics and Power Spectrum	23
3.2	Synthetic Mode Characterization	26
3.2.1	Normal Mode Wavenumbers	27
3.2.2	Critical Layer	29
3.2.3	Synthetic Mode as a VLSM Proxy	30
3.3	Modified Large- and Small-Scale Phase Relations	31
3.3.1	Skewness	31
3.3.2	Amplitude Modulation Coefficient	32
3.3.3	Connection between Skewness and Amplitude Modulation Coefficient	35
3.3.4	Synthetic Large-Scale Effects on Small Scales	37
3.4	Organization of Directly-Coupled Small Scales	38
4	Double-Mode Forcing of the Turbulent Boundary Layer	42
4.1	Flow Statistics and Power Spectrum	42
4.1.1	Triadic Responses in Frequency Space	45
4.2	Synthetic Modes Characterization	47
4.2.1	Normal Mode Wavenumbers and Triadic Responses in Wavenumber Space	51
4.2.2	Wavespeeds and Critical Layers	52
4.3	Phase Relations in Scale Interactions	53
4.3.1	Large- and Small-Scale Interactions	54
4.3.2	Isolated-Scale Interactions	55
4.3.3	Phase Relations at Various Levels in the Interaction Hierarchy	56
4.4	Rank-1 Resolvent Operator Model	62
5	Concluding Remarks	68
	Bibliography	70
	Appendix A	76
A.1	Skewness and Amplitude Modulation Coefficient	76
A.2	Triadic Small-Scale Envelope	79
	Appendix B	81
B.1	Forcing from Two-Mode Interactions	81

List of Figures

2.1	An annotated photograph of the Merrill wind tunnel test section	13
2.2	A schematic of the flat-plate setup	14
2.3	Line drawings of the plate insert and the rib	15
2.4	Line drawings of the two motors used in the experiments	16
2.5	Time-resolved wall perturbation amplitude samples obtained from encoder data in the first and second set of experiments	18
2.6	2D line drawing of the hotwire traverse setup	19
2.7	Mean velocity and turbulence intensity profiles for the canonical flow	21
2.8	Power spectral density of velocity fluctuations for the canonical flow	22
3.1	Mean velocity and turbulence intensity profiles for the flow with single-mode forcing	24
3.2	Power spectral density of velocity fluctuations for the flow with single-mode forcing .	25
3.3	Phase and amplitude maps of the synthetic mode	28
3.4	A schematic of the wavenumber line showing the large- and small-scale regions	32
3.5	Example of a signal with three triadically consistent Fourier components	33
3.6	Skewness and amplitude modulation coefficient profiles for the flow with single mode forcing	37
3.7	Comparison of the synthetic mode shape and the triadic envelope	39
3.8	Correlation coefficient between the synthetic large scale and triadic small-scale envelope	39
4.1	Mean velocity and turbulence intensity profiles for the flow with double-mode forcing	43
4.2	Power spectral density of velocity fluctuations for the flow with double-mode forcing	44
4.3	Power spectral density of velocity fluctuations for the flow with double-mode forcing in temporal wavenumber space	45
4.4	Raw line spectrum of velocity fluctuations for the flow with double-mode forcing at $y = 0.2\delta$	46
4.5	Phase and amplitude maps of the two synthetic forcing modes	49

4.6	Phase and amplitude maps of the two triadic response modes	50
4.7	Skewness and amplitude modulation coefficient profiles for the flow with double-mode forcing	54
4.8	Correlation coefficient between the synthetic large scale and directly coupled triadic scales	56
4.9	Block diagram of interactions among the four synthetic scales	57
4.10	Phase in scale interactions of the two triadic response modes	58
4.11	Phase in scale interactions of the two synthetic forcing modes	59
4.12	Block diagram of interactions among all scales	61
4.13	Comparison of resolvent and experimental response modes for sum wavenumber interaction of the two forcing modes	65
4.14	Comparison of resolvent and experimental response modes for difference wavenumber interaction of the two forcing modes	66
A.1	Envelope comparison	77
A.2	Filter cut-off robustness test	77

List of Tables

2.1	Mean parameters at the three measurement stations for the canonical flow	19
3.1	Streamwise wavelength and decay rate estimates for the synthetic mode	27
4.1	Streamwise wavelength and decay rate estimates for the two synthetic forcing and triadic response modes	51
4.2	Wavespeed estimates for the two synthetic forcing and triadic response modes	52
4.3	Critical layer estimates for the two synthetic forcing and triadic response modes . . .	53

Chapter 1

Background and Motivation

Turbulent fluid flow has been a subject of intense research for well over a hundred years, and is regarded by many as the *last unsolved problem* of classical physics. The large range of spatio-temporal scales (seen in most practical flow settings) and their non-linear coupling make the problem extremely challenging. In addition to its scientific appeal, understanding and predicting the effects of flow turbulence is of great importance to engineering design and other applications. The present thesis investigates the nature of non-linear scale interactions in turbulent boundary layers, a ubiquitous class of wall-bounded turbulent flows. Following a brief historical sketch of the turbulence problem, this chapter provides the relevant background and recent developments in wall turbulence, which naturally follow as motivation for the present work. An outline of the experimental approach is provided in the final section (1.5) of this chapter.

1.1 A Brief Historical Sketch of Turbulence

The seemingly disorderly and complex motion of flowing wind and water has captivated many poetic and artistic figures for centuries. da Vinci's sketches of a water fall (*c.* 1508), Hokusai's *The Great Wave Off Kanagawa* (1832), and van Gogh's *The Starry Night* (1889) are some of the more commonly encountered examples of historical works inspired by visual appeal of flow turbulence.

Such inspirations were not restricted to art alone! Efforts to understand turbulent flows from a scientific perspective can be traced back to the mid-nineteenth century. Hagen (1839) was probably the first to formally recognize two separate states of fluid motion as laminar and turbulent; the former characterized by orderly motion of various layers of the fluid with no lateral mixing, and the latter state characterized by chaotic eddying motions with rapid mixing between fluid layers. Boussinesq's eddy viscosity formulation (1877) attributed the enhanced momentum transport in

turbulent flows to the higher strain rates, clearly recognizing it as a property of fluids in a turbulent state. The seminal experiments by Reynolds (1883) of pipe flows showed the competing roles of inertial and viscous forces in promoting instability in fluid motion, which eventually drives the flow from a laminar to a turbulent state. The ratio of those two quantities, named in his honor as the Reynolds number, provides a dimensionless parametric criterion to help predict the nature (laminar vs. turbulent) of a given flow. The idea of dynamic similitude advanced by Reynolds, along with his later work on the time-averaged form of the governing Navier-Stokes equations, continue to have a profound influence on the scientific study of turbulence and its engineering applications to date.

While progress was made in the nineteenth century on the hydrodynamic theory of fluid flow, it was discredited by the hydraulic engineers of that time as it failed to explain the practically observed drag on solid bodies immersed in a flow at high Reynolds numbers. Various attempts to incorporate the effects of fluid viscosity to explain the seemingly paradoxical observations were to no avail. The crucial breakthrough came at the beginning of the twentieth century with Prandtl's revolutionary idea of the boundary layer (1904). He hypothesized that even at the asymptotic high-Reynolds number limit, the effects of viscosity remained important in a thin region next to the body's surface, called the boundary layer. In this region the relative fluid velocity goes from zero at the surface, a boundary condition resulting from the fluid viscosity, to the free-stream value at the layer edge. The flow outside this region has no mean shear stress and is treated as inviscid. Experimental confirmation of the boundary layer theory resolved the earlier paradoxes nagging hydrodynamic theory, and laid the basic framework for further study of wall-bounded flows, and turbulence in general.

Following these early advances, the problem of turbulence has attracted the attention (and devotion!) of many famous engineers, physicists, and mathematicians through the course of the last hundred years or so. This was partly a result of the great span of applications that require a good understanding of turbulent flow behavior – aerodynamics, geophysical studies, weather prediction, and astrophysics are some examples. In addition, the extremely challenging nature of the fundamental problem is in itself a big draw for many curious minds. The complexity in turbulence arises from its strongly non-linear and irreversible nature resulting in a multi-scale behavior in space and time, which visually manifests as irregular and chaotic motion of the fluid. The problem has seen concerted efforts from the scientific community through a combination of mathematical theory, insightful physical arguments, and experimental and computational tools. Though these efforts have yielded

some success (the degree of which might be subjective), many open questions still remain.¹ Thus turbulence continues to be a highly active and relevant area of research with many opportunities for new learning and application.

1.2 The Turbulent Boundary Layer

Turbulent boundary layer flows are routinely encountered in a wide range of technological applications, and hence are of inherent interest for study. Together with pipe and channel flows (internal geometries), they constitute a set of canonical wall-bounded flows with many common structural and statistical features. Note that the canonical conditions represent the simplest flow scenario where the fluid is incompressible, single-phase, neutrally-buoyant and non-reacting, the wall surface is smooth (and flat for a boundary layer), and there are no external perturbations. The no-slip condition at the wall establishes a mean shear-stress gradient and results in non-homogeneity in the perpendicular direction (referred to as the wall-normal direction), and sets these flows apart from other classes of turbulent flows like free-shear flows, homogeneous flows, *etc.* Vast amounts of literature are available on wall-bounded turbulence in the form of classical texts and monographs (*e.g.* [Schlichting, 1968](#); [Tennekes & Lumley, 1972](#); [Townsend, 1976](#)), and research articles (see [Marusic *et al.*, 2010b](#) and [Smits *et al.*, 2011](#) for recent reviews). Only a broad outline of the underlying concepts and recent advances that are directly relevant are presented here to put the current work in perspective.

1.2.1 Mean Flow Description

Two sets of dynamically relevant length and time scales are of importance in wall turbulence. The effects of viscosity are found to be dominant close to the wall, and the turbulence characteristics in this region can be well described by a set of length (δ_ν) and time (t_ν) scales known as the viscous or inner scales. They are given by $\delta_\nu = \nu/u_\tau$ and $t_\nu = \nu/u_\tau^2$ respectively, where ν is the kinematic viscosity of the fluid and u_τ is the velocity scale (called the friction velocity) defined as $u_\tau \equiv \sqrt{\bar{\tau}_w/\rho}$ ($\bar{\tau}_w$ is the mean wall-shear-stress and ρ is the fluid density). The influence of viscosity diminishes far from the wall and the length scale of importance in this outer region is the boundary layer thickness (δ) itself. Note that the velocity scale u_τ is generally employed in the outer region too; the inner boundary condition for the outer flow is thought to be set by u_τ , and hence it is considered to be

¹A collection of review articles edited by [Davidson, Kaneda & Sreenivasan \(2012\)](#) pertaining to various topics in turbulence provides a fairly up-to-date account of the state-of-the-art in fundamental research.

a global scale that is relevant in both regions. The inner part of the boundary layer is further subdivided into two regions based on the local turbulence characteristics. The region between the wall and $\approx 5 \delta_\nu$, called the viscous sublayer, has very low levels of turbulent velocity fluctuations due to the strong action of viscosity. The region above the sublayer extending to $\approx 100 \delta_\nu$, called the buffer layer, is characterized by intense fluctuations resulting in high levels of turbulence production and dissipation. The separation between the inner and outer regions increases with Reynolds number, which can also be defined as the ratio of the outer and inner length scales δ/δ_ν . With sufficient scale separation, it is reasonable to assume that there is an intermediate overlap region where both inner and outer scalings hold simultaneously. This line of argument leads to the famous ‘log law’ which describes mean velocity profile as having a logarithmic variation with wall-normal distance (Millikan, 1938). Experimental data from wall turbulence at high Reynolds numbers strongly supports the existence of an overlap logarithmic region (Marusic *et al.*, 2013).

1.2.2 Coherent Flow Structures

The above characterization of the boundary layer, which primarily stems from its statistical behavior, forms only a part of the complete description. A long-standing challenge has been the connection between the observed statistical and spectral behavior of the flow field, and the physical dynamical processes that generate the turbulent fluctuations that sustain the observed statistics. Observation and description of flow structures with coherence in space and time, known simply as *coherent structures*, have formed the basis of studies that attempt to provide a framework for making such connections. We recollect here a pertinent remark by Roshko (1976) four decades ago – “there is little doubt that coherent structures play a central role in the development of the several turbulent shear flows”. While a formal definition of a coherent structure is hard to make, the working definitions provided by Berkooz *et al.* (1993) as “organized spatial features that repeatedly appear and undergo a characteristic temporal life cycle”, and by Marusic *et al.* (2010b) as “organized motions that are persistent in time and space and contribute significantly to the transport of heat, mass, and momentum” among others are noted to be useful. Coherent structures hold the tantalizing possibility of providing a simplified low-order description of a complicated high-dimensional non-linear system, although there are no *a priori* guarantees that such a description would be possible at all. Cantwell (1981) and Robinson (1991) provide a review of the several important studies that have advanced our understanding of the importance and behavior of coherent structures; a more recent introduction to the topic can also be found in Sharma & McKeon (2013). It is noted here that the *attached eddy*

model (Townsend, 1976; Perry & Chong, 1982) is probably the most famous example of an attempt to bridge the gap between the statistical and structural views of wall turbulence.

Coherent structures in wall turbulence can be broadly divided into two classes based on the nature of their scaling. Streamwise velocity streaks and quasi-streamwise vortices, which constitute the key structural elements of the near-wall region, are found to scale in inner units. They are centered at a distance of $\approx 15 \delta_\nu$ from the wall, with streamwise and spanwise direction length scales (wavelength) of $\approx 1000 \delta_\nu$ and $\approx 100 \delta_\nu$ respectively. The other class consists of motions with streamwise lengths greater than the boundary layer thickness δ (or pipe radii, channel half-width), broadly referred to as the large scales, and are found to scale in outer units. These organized outer motions are further divided into two sub-classes. The first sub-class consists of motions, known simply as large-scale motions (LSMs), with streamwise and spanwise length scales of $2-3 \delta$ and $1-1.5 \delta$ respectively and are associated with packets of hairpin vortices (Adrian, 2007). The constituent hairpin vortices are not localized and are found to exist over a range of wall-normal locations spanning the buffer and log regions. The second sub-class of motions, known as very large-scale motions (VLSMs²), are further elongated in the streamwise direction with a length scale on the order of 10δ , and consist of spanwise alternating coherent regions of low and high momentum with a length scale of about 1δ (Hutchins *et al.*, 2011). VLSMs are found to be centered in the logarithmic region (Mathis *et al.*, 2009a) with a wall-normal signature that extends down to the wall. The behavior and influence of VLSMs has been an area of active research in recent years in the wall turbulence community. The following section elaborates on the topic, which then leads to the motivation for the current work.

1.3 Large-Scale Influences and Scale Interactions

Though the presence of organized motions at large scales in the overlap and outer regions of a turbulent boundary layer was recognized by early studies (Favre *et al.*, 1967; Kovasznay *et al.*, 1970), their dynamical significance in the flow has gained wide attention only in recent times. The advances in this area were aided by the development of high-Reynolds number experimental facilities and newer flow diagnostics (Smits & Marusic, 2013). The flow Reynolds number is an important factor in understanding large-scale influences on the flow given that the VLSMs, which are shown to account for a considerable fraction of the turbulent energy and Reynolds stress (Guala *et al.*, 2006),

²In literature, the term ‘superstructure’ has been used to describe VLSM-class motions in a boundary layer, while the term VLSM is reserved for use in internal geometries (pipes, channels). Though differences exist between the two (Monty *et al.*, 2009), they share many common features in the context of the present work. Therefore a distinction is not made and usage of the term VLSM is generalized here.

intensify in strength with increasing Reynolds number (Hutchins & Marusic, 2007b); their influence on the flow clearly manifests at high Reynolds numbers which were previously unavailable. With newer facilities, several recent studies have confirmed the existence, and characterized the behavior, of VLSMs in external (boundary layers) and internal (pipes, channels) wall-bounded turbulent flows (e.g. Kim & Adrian, 1999; Guala *et al.*, 2006; Hutchins & Marusic, 2007b; Monty *et al.*, 2007; Hutchins *et al.*, 2011).

1.3.1 Evidence of Large-Scale Influences

Of particular interest to us is the influence of large-scale outer region motions on the dynamics of small-scale turbulent fluctuations, especially in the near-wall region. The failure of classical scaling based on inner (or viscous) units of the near-wall turbulence intensity peak, among other observations, has engendered the idea that the outer region plays a more active role than merely driving the inner flow. The insightful study of turbulent ‘bursts’ (periods of intense small-scale turbulent activity) in a boundary layer by Rao, Narasimha & Narayanan (1971) provided the first clear evidence of coupling between the inner and outer regions. The ‘bursting’ frequency in the inner region was found to scale with outer units as opposed to inner units over a range of Reynolds numbers. A connection between the outer large-scale structure and its effects on the near-wall small-scale activity was made by Brown & Thomas (1977) through correlations between large- and small-scale streamwise velocity and wall-shear-stress fluctuations in a turbulent boundary layer. The study by Chen & Blackwelder (1978) of large-scale structure in a turbulent boundary layer using temperature as a passive contaminant also suggests a dynamical relationship between the outer and inner regions. Following the scale-decomposition technique of Brown & Thomas (1977), the phase relationships between large- and small-scales in a variety of turbulent shear flows were inferred by Bandyopadhyay & Hussain (1984) through correlation measurements of streamwise fluctuating velocity.

1.3.2 Recent Developments

In light of the recent experimental developments mentioned above, the question of scale interactions has evoked a renewed interest. Hutchins & Marusic (2007a) proposed an amplitude modulation mechanism to explain the large- and small-scale relationships; the amplitude of small scales (high temporal frequencies) is understood as being modulated by the large scales (low temporal frequencies), akin to amplitude modulation of a high-frequency carrier by a low-frequency signal in

radio-wave communication (see [Marusic *et al.*, 2010a](#)). This idea was extended and quantified by [Mathis *et al.* \(2009a\)](#) through an elegant demodulation scheme. The streamwise turbulent velocity signal u was first decomposed into large-scale (u_L) and small-scale (u_S) components using a suitable filter with a fixed cut-off such that $u = u_L + u_S$. Then, a correlation coefficient, termed amplitude modulation coefficient (R), between the large-scale velocity signal and an envelope of the small-scale velocity signal (extracted through a Hilbert transform procedure) was taken to be a measure of amplitude modulation in a turbulent boundary layer. The amplitude modulation coefficient was seen to have a very similar behavior with wall-normal distance across turbulent boundary layers, pipes, and channels ([Mathis *et al.*, 2009b](#)). Also, an interesting similarity in the behavior of the amplitude modulation coefficient with the skewness statistic of the streamwise velocity fluctuations was noted by [Mathis *et al.* \(2009a\)](#) without further investigation.

The interpretation of the large- and small-scale correlation as amplitude modulation was met with caution by [Schlatter & Örlu \(2010\)](#). They considered synthetic *turbulent* signals, synthesized by matching the probability density functions (PDF) of random signals to actual turbulent signals, at different heights inside a turbulent boundary layer. Amplitude modulation coefficient calculations, as outlined by [Mathis *et al.* \(2009a\)](#), for the synthetic signals showed a remarkable similarity to results obtained from actual turbulent signals in a boundary layer. From that, [Schlatter & Örlu \(2010\)](#) note that the interpretation of the coefficient R is not straightforward, and suggest that it is to a large extent another representation of the cross terms of the scale-decomposed skewness statistic. [Mathis *et al.* \(2011\)](#) confirm the similarity between the two statistics by showing that the cross term $3u_L u_S^2$, obtained from the expression of skewness for a scale-decomposed signal, mimics the behavior of the amplitude modulation coefficient across a range of Reynolds numbers in turbulent boundary layers. However, [Mathis *et al.* \(2011\)](#) note that the synthetic signals considered by [Schlatter & Örlu \(2010\)](#) are devoid of any scale information, *i.e.* the power spectrum is flat and does not contain amplitude information at any scale, therefore a scale decomposition to segregate large- and small-scales is not necessarily applicable. In a separate study, [Bernardini & Pirozzoli \(2011\)](#) consider two-point velocity correlations obtained from DNS data of a compressible turbulent boundary layer to show clear evidence of non-linear interaction between scales, and the same is interpreted as an amplitude modulation effect.

The large- and small-scale relationship was also investigated with newly available data from large-eddy simulations ([Chung & McKeon, 2010](#)) and atmospheric boundary layers ([Guala *et al.*, 2011](#)). As noted by [Chung & McKeon \(2010\)](#), the amplitude modulation coefficient is fundamentally

a correlation coefficient between the large and small scales, and therefore can be interpreted as a phase relationship between the two quantities, similar to the earlier studies of [Bandyopadhyay & Hussain \(1984\)](#). All the above discussed studies consistently show the correlation between the large scales and an envelope of the small-scale fluctuations to be positive near the wall and negative in the outer region, thereby implying that the two correlated quantities are close to being in phase and out of phase in those respective regions. Among the large scales, the dominating influence on the observed large- and small-scale relationship was shown to be originating at the VLSM scale by [Jacobi & McKeon \(2013\)](#) using a co-spectral technique.

It is now increasingly clear that the large- and small-scale interactions are an important aspect of wall turbulence. A better dynamical understanding of the non-linear scale coupling driving such interactions presents a potential opportunity at unraveling the workings of the wall turbulence system, and narrowing the gap between the statistical and structural pictures of the flow. The VLSMs play an overarching role in this context, particularly at high Reynolds numbers, and thereby present the motivation for further study.

1.4 Forcing-Response Analysis

The present work aims to probe the nature of non-linear scale interactions in a turbulent boundary layer through a study of the flow response to deterministic external large-scale forcing. This approach parallels the ‘black box’ perspective of turbulence suggested by [Clauser \(1956\)](#), where the complex non-linear system at hand is treated as an unknown entity (black box), and is probed by introducing external perturbations and observing its response. The motivation for targeted forcing at the large scales is twofold. Firstly, given the dynamical significance of the large scales (particularly the VLSMs), they are a natural starting point for any attempts at understanding the complicated network of coupled spatio-temporal scales. In addition, the large scales present a practical avenue to experimentally effect external perturbations (or forcing) on the flow, particularly at high-Reynolds numbers. To highlight this consideration we cite here briefly a design example discussed by [Gad-el Hak \(2000\)](#) for an aircraft application. [Gad-el Hak \(2000\)](#) estimates that directly targeting the small-scale near-wall cycle for any flow manipulation or control objective on a typical commercial aircraft in cruise condition requires sensors and actuators on the surface with a density of over a 1 million per square meter, and with the ability to respond at the order of tens of kiloHertz. Whereas we note that a strategy that exploits the inherent scale coupling to target the small-scales indirectly through large-scale forcing presents a much more feasible case for practice. The design of such strategies

requires a clear fundamental understanding of the nature of scale interactions and energy pathways in wall turbulence. The work presented here is a step towards that direction.

1.4.1 Targeted Forcing of Wall Turbulence

The use of external perturbations to elicit flow dynamics is a commonly used technique that can be traced back to the early transition studies by [Schubauer & Skramstad \(1947\)](#) of exponential growth in laminar boundary layer instabilities, where a thin vibrating ribbon along the spanwise direction was placed very near the wall to introduce controlled oscillations in the flow. A similar technique was later used by [Hussain & Reynolds \(1970, 1972\)](#) to introduce dynamic perturbations at set sinusoidal frequencies in a turbulent channel flow and study their downstream evolution. [Reynolds & Hussain \(1972\)](#) also attempted to model the experimental observations of the traveling-wave disturbances by extending the laminar Orr-Sommerfeld equations to a turbulent flow. An eigenvalue problem was formulated for velocity perturbations over a turbulent mean profile with various closure schemes to model the turbulent Reynolds stress. However, such quasi-laminar approaches were not successful in predicting the experimentally observed wavespeeds (eigenvalues) or mode shapes (eigenfunctions), and the main conclusion of [Reynolds & Hussain \(1972\)](#) was to recognize the essential role of the Reynolds stress terms in the flow dynamics.

More recently, [Jacobi & McKeon \(2011a,b\)](#) used a novel experimental technique to study the effects of static and dynamic wall-roughness perturbations in a turbulent boundary layer. The non-equilibrium effects resulting from a k -type spatially-impulsive roughness patch, which consisted of four parallel ribs aligned along the spanwise direction, were extensively characterized. A persistent ‘stress bore’ and spectral redistribution of small-scale energy in the downstream region were identified as key elements associated with the static roughness perturbation ([Jacobi & McKeon, 2011a](#)). In a later study, the same patch of k -type roughness was dynamically actuated in the wall-normal direction at a set sinusoidal frequency. In addition to the previously characterized static roughness effects, the dynamic forcing was shown to introduce a coherent and energetic large-scale spanwise-constant spatio-temporal mode in the flow, with well defined streamwise and temporal length scales ([Jacobi & McKeon, 2011b](#)). The results of [Jacobi & McKeon \(2011b\)](#) clearly demonstrate the effectiveness of the wall perturbation in exciting a synthetic large-scale in the flow. The same technique of wall perturbation is used here in a modified form to effect large-scale forcing of a turbulent boundary layer.

1.4.2 Resolvent Operator Framework

The forcing-and-response approach used here can be viewed in the context of the resolvent operator formulation by [McKeon & Sharma \(2010\)](#). In this approach, the dynamics of the governing Navier-Stokes equations is separated into linear and non-linear parts. The non-linear (convective acceleration) term, which introduces coupling between scales, is then treated as a source of *endogenous* forcing that drives the linear dynamics of the system. The ‘closure problem’ of turbulence is circumvented in this approach, and requires only the mean velocity profile (obtained either by experimental, computational or empirical data) as input for analysis. The resolvent operator of the Navier-Stokes equations, which constitutes the linear dynamics, is found to be low-rank for a wide range of spatial and temporal scales seen in wall turbulence. Thereby [McKeon *et al.* \(2013\)](#) note that the linear dynamics of the system is highly selective and acts as directional amplifier. This allows for a low-rank modeling of the system, and a rank-1 model is shown to capture to a good degree the statistical ([Moarref *et al.*, 2013](#)) and structural ([Sharma & McKeon, 2013](#); [Luhar *et al.*, 2014](#)) features of wall turbulence. The resolvent model is well suited to handle any external forcing imposed on the system, like in the case of the present experiments. The forcing is coherent and deterministic, and this allows for a careful study of the system response using the resolvent model to track the forcing effects, and possibly tailor the forcing to obtain any desired system response.

1.5 Approach

External forcing at the large scale is implemented in a turbulent boundary layer in two separate sets of experiments. These studies focus on the nature of triadic scale interactions resulting from the large-scale forcing. Triadic scale coupling, which refers to the coupling between three wavenumbers where the sum/difference of any two wavenumbers equals the third, is of primary interest given the quadratic non-linearity of the governing Navier-Stokes equations. In wavenumber space, the quadratic non-linearity dictates the direct coupling between scales to be among triadically consistent wavenumbers, *i.e.* any wavenumber k_l is directly coupled to all pairs of wavenumbers k_n, k_m that satisfy the condition $k_l = k_n \pm k_m$.

Chapter 2 provides details of the experimental setups. In the first set of experiments, a single large-scale mode with well defined spatial and temporal wavenumber was excited in the flow using the technique of [Jacobi & McKeon \(2011b\)](#) in a modified form. Results and analysis from this set of experiments are presented in chapter 3. The synthetic scale is seen to modify the naturally existing

triadic phase relationships between scales in a deterministic manner. In particular, a strong phase locking or organization effect is seen among all the triadically consist small scales that are directly coupled to the synthetic scale. Significant portions of this chapter have been previously published as [Duvvuri & McKeon \(2014, 2015a,b\)](#).

Following the single-scale experiments, the experimental setup was modified to enable simultaneous forcing of two distinct spatio-temporal modes in the flow. Results and analysis from this set of experiments are presented in chapter 4. Having characterized the effects of a single synthetic scale in the previous experiment, the emphasis here is on understanding the nature of the two triadic response modes excited by the forcing modes. Specific phase relationships associated with the interactions of the synthetic modes are investigated, and the resolvent model is used to capture the low-rank aspects of the forcing-response dynamics.

The thesis closes with a brief summary and discussion in chapter 5.

Chapter 2

Experimental Setup

Two separate sets of boundary layer experiments on a flat plate were performed with a spatially-impulsive dynamic wall-perturbation to study the influence of large-scale forcing on the flow. The perturbation was set to a single sinusoidal frequency in the first set, and a combination of two sinusoidal frequencies were used in the second set. Canonical flow measurements (with no perturbation) were also made in both cases to serve as reference for later analysis. Experimental details and canonical flow characteristics are presented in this chapter.

2.1 Flat-Plate Boundary Layer Facility

The flat-plate boundary layer experiments were performed in the Merrill wind tunnel at GALCIT. The facility is well characterized and has been described in detail previously by [Jacobi \(2012\)](#). The Merrill wind tunnel has a closed-loop (recirculating) design and is driven by a ducted fan and 50 HP AC induction motor assembly. Air temperature in the tunnel is controlled by an active in-loop cold-water heat exchanger positioned upstream of the test section. The temperature was held constant at approximately 22°C with a maximum deviation of $\pm 0.2^\circ\text{C}$ during the course of all experiments. The test section is made of acrylic glass (PMMA) with dimensions $2' \times 2'$ in the transverse plane and 8' in length, and has a deformable ceiling that allows for adjustments to the mean pressure gradient along the streamwise direction (x). An annotated photograph of the test section is shown in figure [2.1](#).

The test article consists of a smooth acrylic flat-plate at mid-height spanning the entire width and almost the full streamwise extent. The plate has an elliptic leading edge, and a trailing-edge flap that was set to maintain the leading-edge stagnation point on the measurement side (top). All experiments were performed with a nominally constant free-stream velocity \bar{U}_∞ of 22.1 m/s;

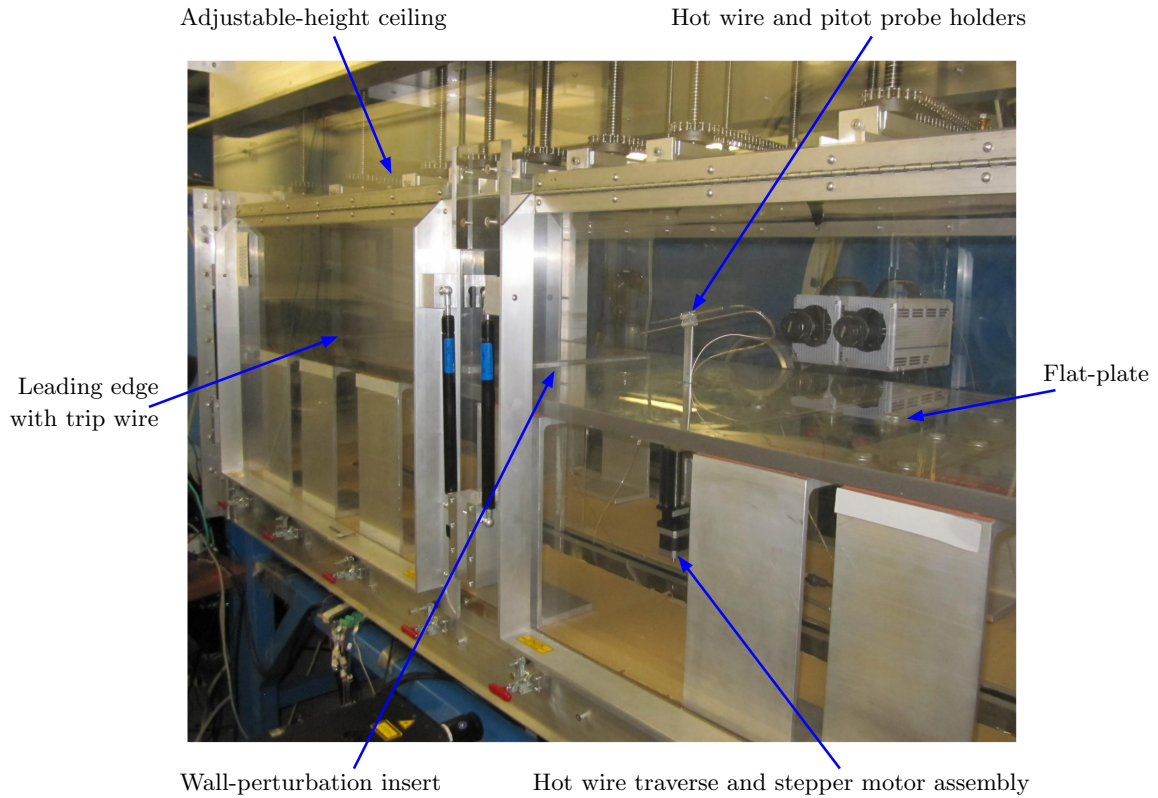


FIGURE 2.1: A photograph of the Merrill wind tunnel test section. Air flow inside the section is from left (upstream) to right (downstream). Some of the experimental components described in the text are identified here.

streamwise turbulence intensity (RMS) is under 0.2% of \bar{U}_∞ in the free-stream at this mean velocity. The incoming flow was tripped near the leading edge (19 mm downstream of the tip) by a 0.76 mm diameter piano wire glued to the plate surface resulting in a quick transition of the boundary layer to a turbulent state. The test section height profile was preset to obtain an approximately zero-mean-pressure-gradient flow over the entire length for the given flow condition. The stagnation point location and zero-mean-pressure-gradient condition were confirmed by measurements of pressure from taps positioned along the length of the plate using a Scanivalve pressure scanner (model DSA3217); the variation in the pressure coefficient (ΔC_p) was found to be under 1% of the mean over the range of measurement locations.

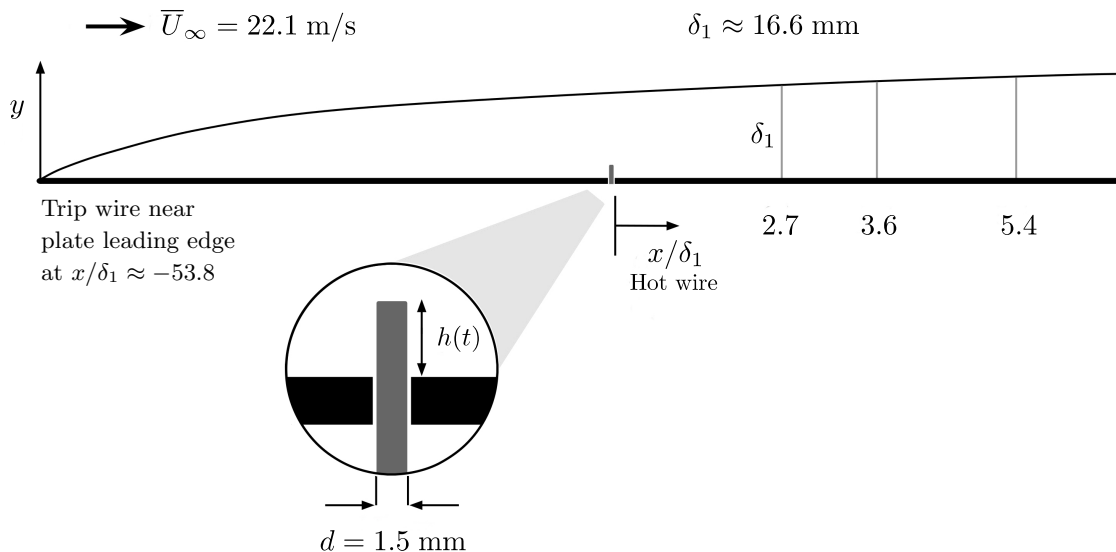


FIGURE 2.2: A schematic of the flat-plate setup (not to scale). The inset shows the spanwise-constant wall perturbation rib positioned 890 mm downstream of the plate’s leading edge trip wire, this location corresponds to $x = 0$. The hotwire measurement stations downstream of the perturbation ($x > 0$) are marked. The free-stream mean velocity \bar{U}_∞ is 22.1 m/s and the local boundary layer thickness δ at measurement station-1 is $\delta_1 \approx 16.6 \text{ mm}$. Note that the marked distances of the measurement stations from the wall perturbation location are normalized by δ_1 .

2.2 Dynamic Wall Perturbation

A spatially-impulsive spanwise-constant dynamic wall perturbation was introduced at a downstream location of 890 mm from the trip wire (see figure 2.2 for a schematic). Note that the flow is fully turbulent at this location with an estimated momentum-thickness-based Reynolds number $Re_\theta \approx 2750$. The perturbation consists of a thin straight aluminum rib of thickness $d = 1.5 \text{ mm}$ aligned along the spanwise direction about the plate centerline with an extent of 230 mm ($\approx 13.9 \delta_1$). A slotted insert fitted into the plate allows for the rib to protrude into the boundary layer through the plate from underneath (see figure 2.3 for a drawing of the insert and the rib). The insert slot is machined with sufficient tolerance to allow rib reciprocation with minimal friction but prevent air bleed between plate surfaces. The rib is connected to an actuation mechanism placed underneath the test section and set to oscillatory motion in the wall-normal direction. Different actuation mechanisms were used in the first and second sets of experiments, and are described below in detail.

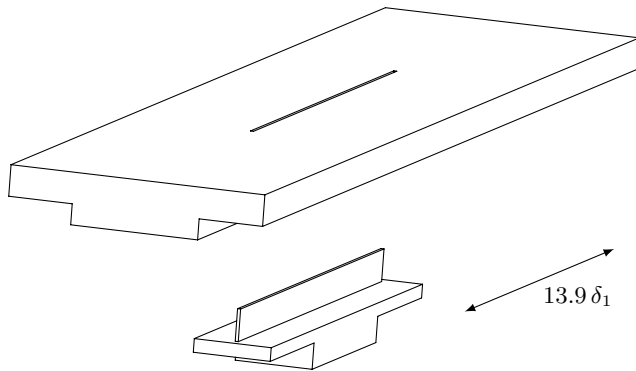


FIGURE 2.3: Line drawings of the plate insert and the rib. The insert slot allows for rib reciprocation, and can be seen in figure 2.1. The armature supporting the rib and its base is connected to a driving mechanism positioned underneath the test section (described in sections 2.2.1 and 2.2.2).

2.2.1 Single-Frequency Oscillations

In the first set of experiments the rib was driven by a crankshaft and DC motor mechanism (Dayton 4z142, see figure 2.4a) such that the motor shaft rotations translate to linear oscillations of the rib in the vertical direction (and sinusoidal in time). The frequency of oscillations was controlled by the motor rotation rate, and the amplitude was fixed by an offset between the connecting rod and the shaft center. Note that at the trough of each oscillation cycle, the rib sits flush with the plate surface. The operational frequency f_p was set to a constant of 50 Hz for all experiments in this set, and the crank shaft offset was machined to 0.3 mm. At low oscillation frequencies the offset resulted in rib oscillations with a root-mean-square amplitude (peak-to-peak) h_{rms} of $2 \times 0.3/\sqrt{2} = 0.42$ mm. However, at the operational frequency $f_p = 50$ Hz used here, slippage due to wear and heating resulted in a slightly higher peak-to-peak amplitude of $h_{\text{rms}} = 0.54 \pm 0.02$ mm. A magnetic linear encoder (Renishaw LM10) with a resolution of $1 \mu\text{m}$ was attached to the actuation mechanism to obtain the time-resolved perturbation input signal to the flow, *i.e.* height $h(t)$. A 200 ms sample of $h(t)$ is shown in the top panel of figure 2.5; the waveform can be written as (in mm)

$$h(t) = 0.4 + 0.4 \cos(2\pi \cdot 50 \cdot t). \quad (2.1)$$

The encoder signal was recorded along with the hotwire data during the course of experiments (see section 2.3.1). The encoder signal enables phase-locking and phase-averaging of the hotwire data during the post-processing stage, and is described in detail in chapter 3.

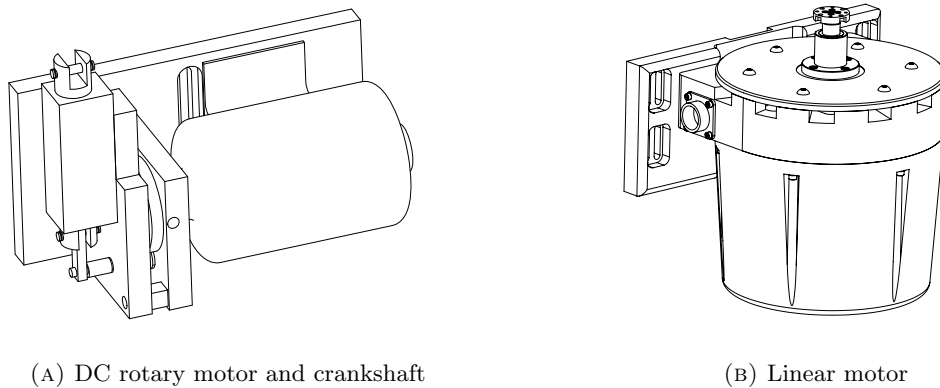


FIGURE 2.4: Line drawings of the two motors used in the experiments (not to scale). In both cases, the armature supporting the rib (seen in figure 2.3) is connected to the motor shafts seen in this figure; the corresponding rib oscillation waveforms are shown in figure 2.5. It is to be noted that motors are positioned below the test section, and are not visible in figure 2.1.

The wall perturbation design and the actuation mechanism are similar to the earlier experiments of [Jacobi & McKeon \(2011a,b\)](#) performed in the same facility. A k -type wall-roughness consisting of four parallel ribs, of thickness 1.57 mm each, aligned along the spanwise direction with an inter-rib distance of 6.35 mm and $h_{\text{rms}} = 1.16$ mm was used in their study with a $f_p = 30$ Hz. In comparison, the perturbation here is truly spatially-impulsive in nature with a significantly reduced streamwise extent and a smaller amplitude. This minimizes the static roughness effects observed in the previous work. To get a sufficiently strong dynamic forcing effect on the flow from a relatively smaller perturbation, the forcing frequency f_p had to be set at a higher value; this was chosen to be 50 Hz. The chosen value of f_p also targets the large-scale region of the turbulence spectrum as desired.

2.2.2 Double-Frequency Oscillations

The actuation mechanism used in the first set of experiments was restricted to only a single operational frequency and a preset amplitude determined by the crankshaft offset. For the second set of experiments, the DC motor mechanism was replaced with a linear motor based design that allows for actuation of the rib with complex waveforms; the perturbation rib was connected directly to the shaft of a Bose LM1 linear motor (see figure 2.4b) placed underneath the test section. The linear motor consists of an electromagnet in a flexure suspension driven by a fixed secondary electromagnet in proximity. This assembly is housed in a cylindrical casing and has an appearance similar to that of a conventional rotary motor. The control signal is applied to a signal conditioner unit which in

turn is connected to an amplifier that powers the motor. A computer software supplied with the motor allows for user-defined waveforms to be input to the signal conditioner. The non-linear nature of the flexure suspension results in a non-flat motor transfer function (both in amplitude and phase), and has to be accounted for in the design of inputs waveforms. An in-built optical encoder provides a time-resolved signal of the motor shaft displacement with a resolution of $10\ \mu\text{m}$; the encoder signal is recorded similar to the first set of experiments.

A waveform consisting of two sinusoidal frequency components was chosen for the study of forced triadic interactions in the second set of experiments. A 35 Hz component was added to the 50 Hz frequency component used in the first set of experiments. Along with the 50 Hz component, the 35 Hz component targets the large-scale region of the spectrum as desired. In addition, the combination of 35 Hz and 50 Hz isolates the triadic responses (15 Hz and 85 Hz) from the fundamental harmonics (70 Hz and 100 Hz); this aspect is elaborated in chapter 4. The motor input signal was adjusted to get an equal amplitude response of 0.4 mm from the motor for each of the two components. The final waveform is given by (in mm)

$$h(t) = 0.8 + 0.4 \cos(2\pi \cdot 35 \cdot t) + 0.4 \cos(2\pi \cdot 50 \cdot t); \quad (2.2)$$

a 200 ms sample of $h(t)$ obtained from the encoder signal is shown in the bottom panel of figure 2.5. The same waveform was used for all experiments in this set.

2.3 Velocity Measurements

Hotwire measurements of the streamwise velocity component were made at three measurement stations downstream of the perturbation along the plate centerline (see figure 2.2) and various wall-normal locations (y) at each of the stations. The hotwire probe holder was fixed to a precision 1D traverse system mounted to the plate via a circular airtight port (see figure 2.6). The streamwise position of the wire was manually set by adjusting the probe holder extension as needed for each experiment. The traverse leadscrew was driven by a computer-controlled stepper motor (Velmex BiSlide) with a resolution of $2.5\ \mu\text{m}$ per turn in the wall-normal direction. An external magnetic linear absolute encoder (Renishaw LMA10) was attached to the traverse system to provide a redundancy check on the probe location (distance from the wall). The closest measurement point to the wall is at a distance of approximately $150\ \mu\text{m}$; this location is set manually, aided by calibrated camera (Nikon D300s with a 170 mm Tamron SP-AF-180 F3.5 macro 1:1 lens and a Tamron AF

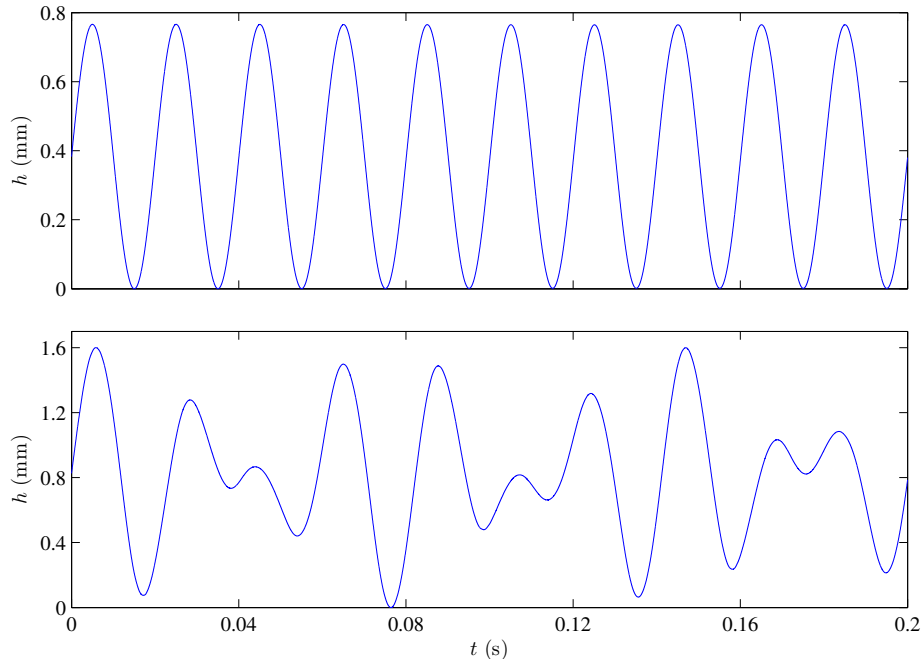


FIGURE 2.5: Wall perturbation amplitude $h(t)$ samples obtained from encoder data in the first (top panel) and second (bottom panel) set of experiments are shown over a period of 200 ms. The corresponding waveforms are in equations 2.1 and 2.2. Note that $h = 0$ corresponds to the wall ($y = 0$).

2X teleconverter) images of the probe. Starting at this point, the probe was moved automatically to subsequent preset wall-normal measurement locations. At each station time-resolved streamwise velocity measurements were made at 43 and 50 logarithmically spaced wall-normal locations in the first and second set of experiments respectively.

2.3.1 Hotwire Anemometry and Data Sampling Parameters

A 5 μm diameter gold-plated tungsten boundary-layer type probe (Dantec 55P05) with an active-length $l = 1.25$ mm was used with a Dantec StreamLine Pro anemometer. The wire was operated at a fixed over-heat ratio of 1.8 and calibrated *in situ* against Pitot tube measurements made using a Baratron MKS 220DD pressure transducer (0-20 Torr range). Calibration runs were made across a range of free-stream velocities immediately prior to, and after every experiment to ensure steadiness of calibration. A fifth-order polynomial fit was used as a transfer function to obtain velocity from anemometer voltage information. The frequency response of the system was estimated using the standard pulse-response test and found to be between ≈ 25 kHz and ≈ 55 kHz for mean velocities ranging from 0 m/s to 22.1 m/s, well above the spectral region of interest for these experiments. For

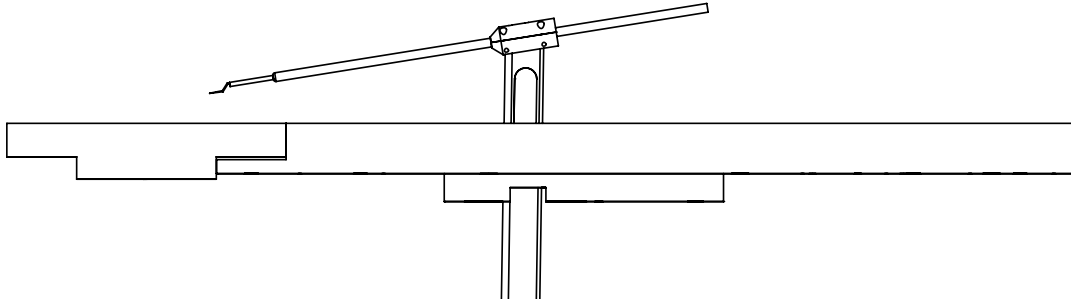


FIGURE 2.6: 2D line drawing of the hotwire traverse setup. The hotwire and probe holder are fixed to a plate-mounted sting as shown. The sting is traversed by a stepper motor arrangement (not seen here, but visible in figure 2.1). The insert shown in figure 2.3 can be seen here as part of the plate.

the given setup and operating conditions, the uncertainty in velocity measurements is estimated to be under 1% following the instrument manual provided by Dantec.

Voltage signals from the anemometer were low-pass filtered at 30 kHz using the anemometer’s built-in third-order Butterworth filter prior to acquisition. A National Instruments A/D card (NI-6154) was used to record digital data at a sampling frequency $f_s = 60$ kHz satisfying the Nyquist requirement. The motor encoder signals (sections 2.2.1 and 2.2.2) were simultaneously digitized and recorded using a second channel on the same card. Sample record lengths were set to $T = 60$ s and $T = 80$ s in the first set and second set of experiments respectively at all wall-normal measurement locations and stations, corresponding to $\approx 80,000$ and $\approx 107,000$ outer eddy turnover periods.

2.4 Canonical Flow Statistics and Power Spectrum

Station	x/δ_1	δ (mm)	Re_θ	Re_τ
1	2.7	16.55	2780	940
2	3.6	16.64	2804	942
3	5.4	16.75	2892	955

TABLE 2.1: Canonical (smooth wall) boundary layer mean parameters at the three measurement stations downstream of perturbation. δ_1 is the layer thickness δ at station-1. Karman number (Re_τ) is estimated is using the Coles-Fernholz relation (see text).

Mean flow parameters for the canonical zero-pressure-gradient turbulent boundary layer at the three measurement stations are summarized in table 2.1. The boundary layer thickness δ is estimated from the mean velocity profile using the 99% criteria; a local spline curve fit is used at the boundary

layer edge to determine δ such that $\bar{U}(\delta) = 0.99\bar{U}_\infty$. The momentum thickness θ of the boundary layer is also estimated directly from the mean velocity profile to obtain the momentum-thickness-based Reynolds number $Re_\theta (\equiv \bar{U}_\infty\theta/\nu)$. Karman number (Re_τ) estimates shown in the table 2.1 are then obtained from the local values of Re_θ by using the Coles-Fernholz empirical relation

$$C_f \equiv 2 \left[\frac{u_\tau}{\bar{U}_\infty} \right]^2 = 2 \left[\frac{1}{\kappa} \log(Re_\theta) + C \right]^{-2}, \quad (2.3)$$

where C_f is the skin-friction coefficient and u_τ is defined as the friction velocity ($u_\tau \equiv \sqrt{\bar{\tau}_w/\rho}$ with $\bar{\tau}_w$ and ρ denoting the mean wall-shear-stress and fluid density respectively). The Karman constant κ and C in the above relation are taken to be $\kappa = 0.384$, $C = 4.127$ following Nagib *et al.* (2007). Equation 2.3 provides estimates of u_τ for given values of Re_θ . From thus obtained u_τ , the Karman number is written as

$$Re_\tau = \frac{u_\tau\delta}{\nu} = \delta^+, \quad (2.4)$$

where ν is the kinematic viscosity of air. Based on these estimates, the inner length scale ν/u_τ is used along with the outer scale δ for scaling appropriate quantities to serve as a reference, and the scaled quantities are denoted using the conventional ‘+’ superscript notation. However, all velocity and spectral power information is scaled only in outer units given the uncertainty in estimates of friction velocity.

2.4.1 Mean Velocity and Turbulence Intensity

Time-resolved velocity signals $U(y, t)$ from the hotwire are decomposed into mean and fluctuating components (Reynolds decomposition):

$$U(y, t) = \bar{U}(y) + u(y, t). \quad (2.5)$$

Figure 2.7 shows the mean velocity \bar{U} and turbulence intensity $\sqrt{u^2}$ profiles at station-1. The near-wall peak in intensity commonly seen at $y^+ \approx 15$ (*e.g.* Smits *et al.*, 2011) occurs here at $y^+ \approx 21$. From this, the combined uncertainty in y from near-wall probe positioning and the friction velocity estimate (from equation 2.3) is inferred to be $6\nu/u_\tau \approx 100 \mu\text{m}$. Figure 2.7 also shows Laser Doppler Velocimetry (LDV) measurements of DeGraaff & Eaton (2000) from a boundary layer flow at comparable Reynolds number of $Re_\theta = 2900$. Note that a uniform offset of $\Delta y^+ = 6$ was applied to the data of DeGraaff & Eaton (2000) in figure 2.7 to account for the uncertainty in y discussed

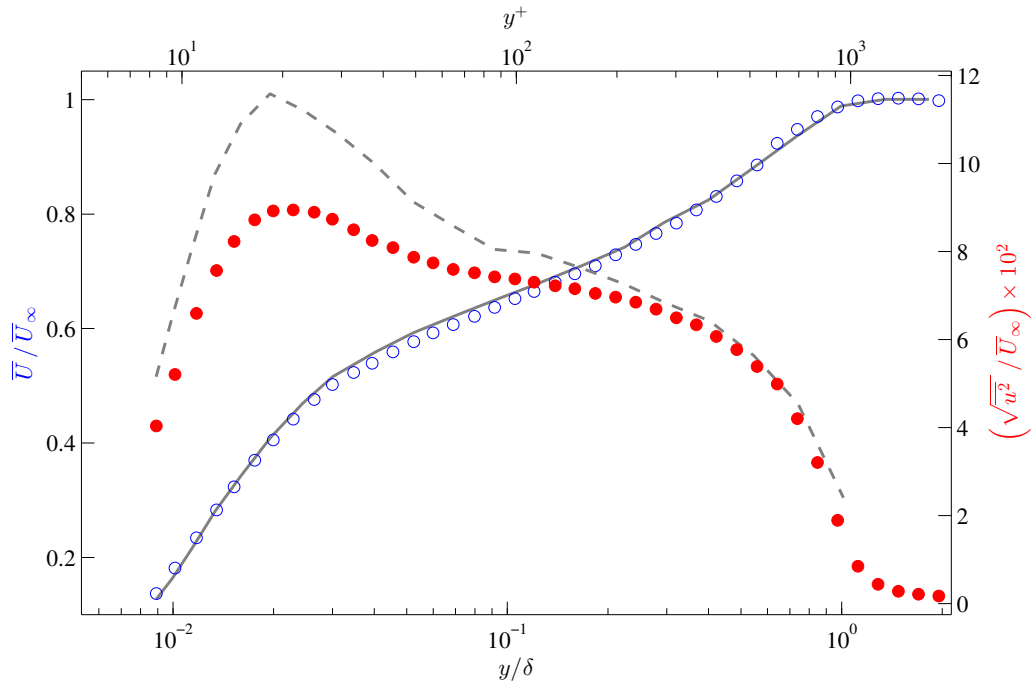


FIGURE 2.7: Mean velocity (open markers) and turbulence intensity (filled markers) profiles at station-1 for the canonical zero-pressure-gradient turbulent boundary layer. Mean velocity (solid line) and intensity (dashed line) data from DeGraaff & Eaton (2000) are shown for comparison.

above and enable a direct comparison between the two data sets.

At the given Reynolds number the viscous-scaled wire length is $l^+ = 71$; significant attenuation of the near-wall peak intensity is to be expected for $l^+ > 20$ (Hutchins *et al.*, 2009) due to spatial resolution limits of the wire, and the same can be seen in figure 2.7. However, with a peak $\overline{u^2}^+ = 4.38$, the level of attenuation is lower than the predicted value of $\overline{u^2}^+ \approx 3.8$ from the data fit of Hutchins *et al.* (2009). Overall, the comparisons to DeGraaff & Eaton (2000) are satisfactory and confirm the canonical nature of the flow in the present setup. No corrections were applied to the wall-normal locations of data or turbulence intensity as they have no direct bearing on the analysis or conclusions presented here.

2.4.2 Velocity Power Spectrum

The power spectral density (PSD) Φ_u of u provides a scale-wise distribution of the power (variance). In the frequency domain f , we have

$$\int_{f \rightarrow 0}^{\infty} \Phi_u(y, f) df = \overline{u^2}(y). \quad (2.6)$$

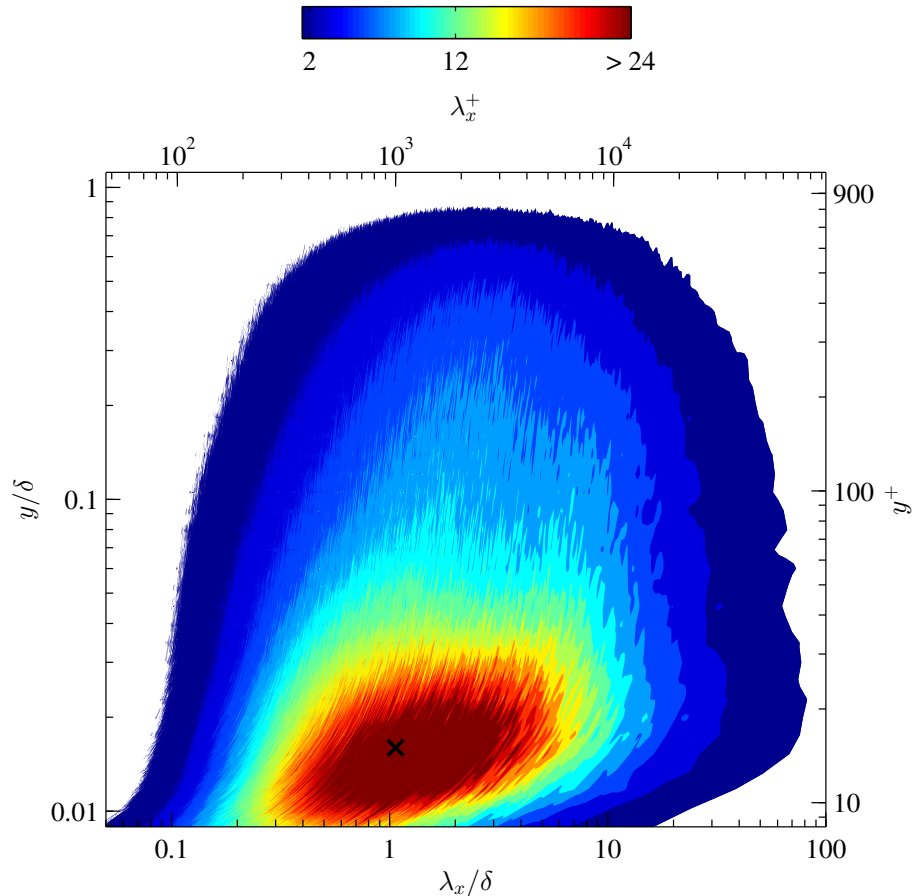


FIGURE 2.8: Pre-multiplied and scaled power spectral density $(k_x \delta / \bar{U}_\infty^2) \Phi_u^c \times 10^6$ at station-1. ‘x’ denotes the vicinity of the expected near-wall cycle (inner) peak at $y^+ = 15$, $\lambda_x^+ = 1000$.

Figure 2.8 shows $\Phi_u^c(y, f)$ at station-1 calculated from $u(y, t)$ using the standard Welch’s method, with superscript c denoting canonical flow. Taylor’s hypothesis of ‘frozen turbulence’ (Taylor, 1938) is applied to project temporal fluctuations onto the streamwise direction (frequency f to wavenumber k_x) using the local mean velocity, and the power levels are shown in a pre-multiplied form, both following conventions in recent experimental wall turbulence literature.

Statistical and spectral results for the canonical flow at stations-2 and -3 are similar to station-1 and are not shown here. This is expected given only the slight increase in Reynolds number (table 2.1) from station-1 to -3.

Chapter 3

Single-Mode Forcing of the Turbulent Boundary Layer

The single-frequency wall perturbation described in chapter 2.2.1 excites a coherent spanwise-constant velocity fluctuation in the downstream region with well defined spatial (streamwise direction) and temporal scales. In this chapter the spatio-temporal mode, or traveling wave, is characterized using hotwire velocity data and its influence on the flow is studied. The streamwise length and time scales of the synthetic mode roughly correspond to the VLSM scales active in canonical flows at higher Reynolds numbers. The study focuses on the nature of phase relationships between the large- and small-scales of turbulence in the presence of the synthetic large-scale mode. An interesting small-scale phase-locking or organization is revealed through the analysis in section 3.4 at the end of this chapter.

3.1 Flow Statistics and Power Spectrum

The mean velocity and turbulence intensity profiles for flow with single-mode forcing at station-1 ($x = 2.7 \delta_1$) are compared with corresponding canonical flow data in figure 3.1. Station-1 is sufficiently far downstream of the perturbation for the flow to recover from the severe static roughness effects, described in detail previously by Jacobi & McKeon (2011a,b). A slight deficit in the mean momentum relative to the canonical flow is still noticeable at this streamwise location, and is attributed to the rib blockage and the resulting ‘stress bore’ (Jacobi & McKeon, 2011a). However, the static roughness effects are expected to be minimal in comparison with the dynamic forcing, and the present study will focus on the latter. The boundary layer thickness is found to remain the same, and hence there is no significant change in Re_θ (and Re_τ) between the two flows given

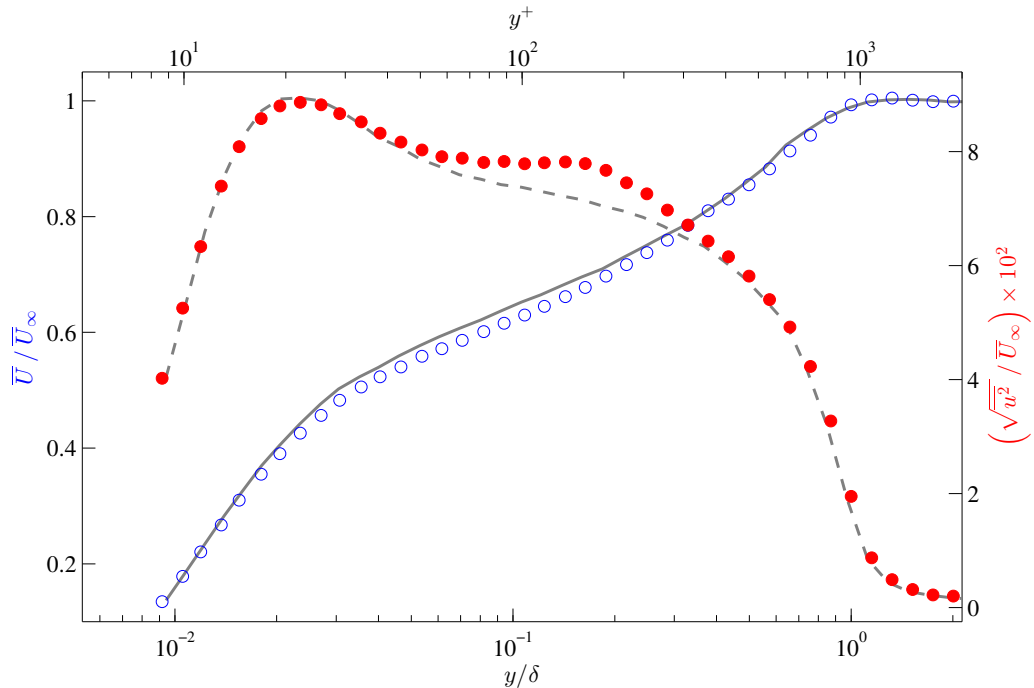


FIGURE 3.1: Mean velocity (open markers) and turbulence intensity (filled markers) profiles for flow with single mode forcing at station-1. Canonical flow mean velocity (solid line) and intensity (dashed line) data from figure 2.7 are also shown for comparison.

the nearly overlapping mean velocity profiles. It should be noted that the Coles-Fernholz estimate (equation 2.3) is strictly applicable only to the canonical flow. However, viscous scaling provides a useful reference and is shown in figures throughout along with outer scaling.

The energetic hump in the turbulence intensity seen between $y \approx 0.05 \delta$ and $y \approx 0.4 \delta$ is mostly a result of the dynamic forcing, and can be better understood from the power spectral density Φ_u^{f1} (superscript $f1$ denotes single-mode forcing) shown in figure 3.2. The presence of a synthetic scale is clearly seen in the form of an energetic narrow-band streak in the large-scale region of the spectrum. It is to be noted that this band corresponds to the temporal forcing frequency of 50 Hz projected onto the streamwise direction x using the local mean velocity \bar{U}_∞ . The difference spectra in the figure reveals that the dominant change (in comparison with the canonical flow) brought about by the forcing is the excitation of the synthetic scale. The temporal wavenumber of the synthetic scale (denoted by $\tilde{\omega}$) is $\tilde{\omega} = 0.24 \bar{U}_\infty \delta^{-1}$. A clear separation in scales exists between the synthetic scale and the natural energetic small scales in the flow. This allows for a scale decomposition to study large- and small-scale interactions in the presence of the synthetic mode, as elaborated on in section 3.3.

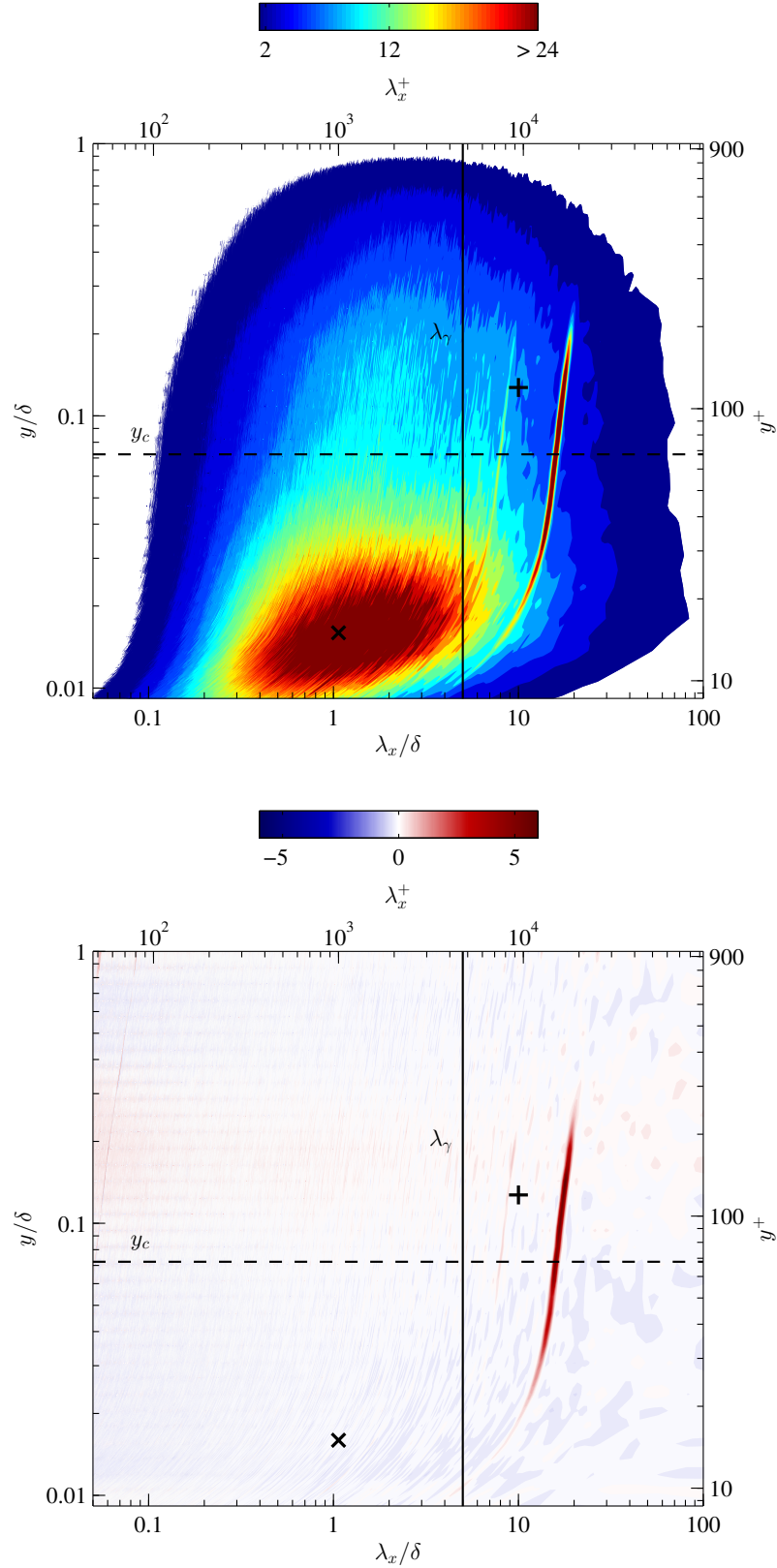


FIGURE 3.2: Top panel shows pre-multiplied power spectral density $(k_x \delta / \bar{U}_\infty^2) \Phi_u^{f1} \times 10^6$, and the bottom panel shows the normalized difference in power levels $(\Phi_u^{f1} - \Phi_u^c) / \Phi_u^c$ between the forced and canonical (figure 2.8) flows at station-1. In both panels, ‘x’ and ‘+’ denote the vicinity of the expected near-wall cycle and VLSM (see section 3.2.3) peaks respectively. The critical layer location $y_c = 0.072\delta$ (section 3.2.2) and the filter cut-off $\lambda_\gamma = 5\delta$ (section 3.3.4) are also marked.

The effects of the spatially-impulsive forcing decay with downstream distance, and the flow statistics and spectrum eventually collapse onto to the canonical case. The streamwise spatial wavelength and the decay rate for the synthetic scale are estimated in the following section using phase-locked velocity data from stations -1 to -3.

3.2 Synthetic Mode Characterization

The time-resolved velocity fluctuations $u(y, t)$ can be decomposed into an organized wave component \tilde{u} corresponding to the synthetic mode, and a reminder term u' that comprises of the *turbulent* fluctuations. Following [Hussain & Reynolds \(1970\)](#) and [Jacobi & McKeon \(2011b\)](#), equation 2.5 for the streamwise velocity at each station (fixed x and z) can be re-written as

$$U(y, t) = \bar{U}(y) + \tilde{u}(y, t) + u'(y, t). \quad (3.1)$$

The wave component \tilde{u} represents fluctuations at a specific spatio-temporal scale; with the streamwise, spanwise, and temporal wavenumbers denoted by real quantities \tilde{k}_x , \tilde{k}_z , and $\tilde{\omega}$ respectively, \tilde{u} can be written in a general form as

$$\tilde{u}(x, y, z, t) = \frac{1}{2} \hat{u}(y) e^{i([\tilde{k}_x + i\beta]x + \tilde{k}_z z - \tilde{\omega}t)} + \text{c.c.}, \quad (3.2)$$

where exponent β is the decay rate of the synthetic mode. The complex amplitude $\hat{u}(y)$ contains both magnitude and phase information of the synthetic mode with wall-normal distance.

The wave component \tilde{u} at all measurement locations is obtained from experimental data by the following procedure. The temporal velocity signal $u(t)$ is first filtered through a narrow bandpass Fourier filter (10 Hz bandwidth) centered around the forcing frequency (50 Hz), and then phase-averaged over 2700 cycles with reference to the input forcing signal $h(t)$. The filtering process mitigates de-correlating effects caused by frequency content naturally present in the flow, but is not a necessary step prior to averaging of phase. Note that $\langle \tilde{u} \rangle$, where $\langle \cdot \rangle$ represents the mean operator, is zero by definition. Using the signal $h(t)$ as a phase reference, the synthetic mode oscillation cycle with wall-normal distance can be constructed in a coherent manner. Phasemaps in [figure 3.3](#) generated following the above procedure show the variation in amplitude and phase of \tilde{u} with wall-normal and streamwise distances.

Stations (Δx)	$\tilde{\lambda}_x/\delta_1$	$\beta \delta_1$
1-2 ($0.9\delta_1$)	15.4	0.28
2-3 ($1.8\delta_1$)	16.1	0.21

TABLE 3.1: Streamwise wavelength $\tilde{\lambda}_x$ and decay rate β for the synthetic mode estimated using data between stations -1 and -2 (top row), and stations -2 and -3 (bottom row).

3.2.1 Normal Mode Wavenumbers

The streamwise wavelength $\tilde{\lambda}_x (= 2\pi/\tilde{k}_x)$ of the synthetic scale is estimated by tracking the change in phase ϕ of \tilde{u} with streamwise distance between stations -1 and -3. At each of the three measurements stations, the value of phase the local phase $\phi(y)$ is taken at the wall-normal location where the mode amplitude (RMS of \tilde{u}) is highest to minimize any de-correlation errors in phase arising from the phase-averaging procedure. A visual inspection of the phasemaps in figure 3.3 reveals a fairly good degree of phase coherence with wall-normal distance of the synthetic mode between stations -1 and -3, thereby justifying the above method. With that, we write $\tilde{\lambda}_x = 2\pi(\Delta x/\Delta\phi)$; estimates of $\tilde{\lambda}_x$ are shown in table 3.1. The exponential decay rate β is also estimated in a similar manner by choosing the peak amplitude of \tilde{u} at each station and tracking its change with streamwise distance; values for β are shown in the same table.

With the above information, the synthetic scale is now considered as a normal spatio-temporal mode of wavenumber $\tilde{\mathbf{k}} = (0.41\delta^{-1}, 0, 0.24\bar{U}_\infty\delta^{-1})$, where $\tilde{\mathbf{k}}$ is the wavenumber triplet $(\tilde{k}_x, \tilde{k}_z, \tilde{\omega})$. Here \tilde{k}_x is calculated using the value of $\tilde{\lambda}_x = 15.4\delta_1$ between stations -1 and -2 as it is prone to a lesser estimation error in comparison to the value of $\tilde{\lambda}_x = 16.1\delta_1$ obtained between stations -2 and -3, where the synthetic mode undergoes further decay. The spanwise-constant perturbation excites a mode with \tilde{k}_z nominally being zero. However, the finite spanwise extent of the perturbation rib and the end effects caused by lateral walls of the wind tunnel test section probably induce a weak 3D nature to the synthetic scale in practice. Bearing this in mind, \tilde{k}_z is identically set to zero. It is to be noted that the ‘locally parallel’ approximation for the boundary layer is implicitly invoked here by modeling the streamwise spatial fluctuations as a Fourier mode. Given the only minor variation in δ and Re_τ over the streamwise range of measurements, it is justified to be a reasonable approximation.

The amplitude and phase behavior of the synthetic mode are broadly similar to the earlier work of Jacobi & McKeon (2011b), where $\tilde{\lambda}_x$ was reported to be 18.7δ . It is interesting to note that a substantial reduction in the streamwise extent and amplitude of the wall perturbation in comparison

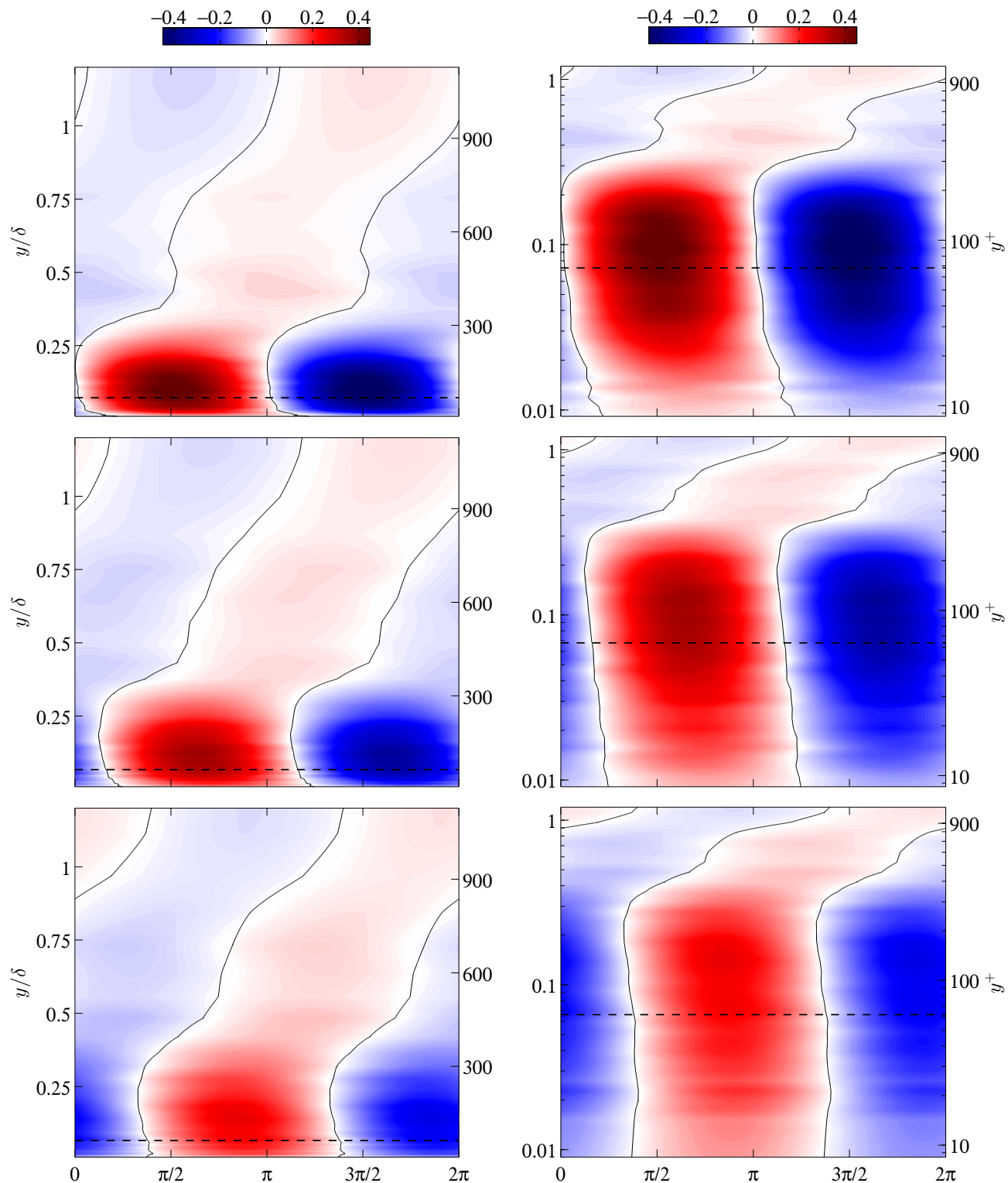


FIGURE 3.3: Phasemaps of $\tilde{u}(y, t)$ over one temporal period of oscillation. Top, center, and bottom panels show data from stations -1, -2, and -3 respectively in raw velocity units (m/s). Wall-normal distance is shown on a linear scale in the left panels, and on a logarithmic scale to highlight the near-wall region in the right panels. Solid curves are contour levels at $\tilde{u} = 0$, and dashed horizontal lines indicate the local critical layer location y_c on all panels.

to [Jacobi & McKeon \(2011b\)](#) resulted in only a marginal decrease in $\tilde{\lambda}_x$. This suggests that the dynamics of the periodic separation and reattachment bubble around the perturbation rib, which sets the streamwise length scale, is most receptive to $\tilde{\lambda}_x$ on the scale of $\mathcal{O}(10\delta - 20\delta)$. Conversely, the flow response can also be understood in terms of the wavespeed ($\tilde{c} = \tilde{\omega}/\tilde{k}_x$) of the synthetic mode. The wavespeed $\tilde{c} = 0.59\bar{U}_\infty$ found in the present experiment is close to $\tilde{c} = 0.47\bar{U}_\infty$ reported by [Jacobi & McKeon \(2011b\)](#), both are around $\tilde{c} \sim 0.5\bar{U}_\infty$; the flow response seems to be selective to a wavespeed in that range. Data from the second set of experiments presented in the following chapter also supports this hypothesis (see section 4.2.2). A more detailed study covering the rib amplitude, frequency, and flow Reynolds number parameter space is required to gain a better understanding of the spatial length scale or wavespeed set by the dynamic wall perturbation. Such a study is beyond the scope of this work; instead the focus here is on exploiting the large-scale forcing effects of the wall perturbation to investigate the nature of non-linear scale coupling in the flow.

3.2.2 Critical Layer

For a traveling wave in a shear flow, the critical layer is defined as the location where the wavespeed matches the local mean velocity. In the high-Reynolds number inviscid limit, the governing Navier-Stokes equations pose a singular point at the critical layer. For a wall-bounded flow, viscosity must be considered in the region around the critical layer, along with the near-wall region, to regularize the solution. The traveling wave mechanics are strongly influenced by the critical layer (*e.g.* see [Maslowe, 1986](#); [Schmid & Henningson, 2001](#)), and critical layer effects are relevant in the present study. For the synthetic mode, using the wavespeed $\tilde{c} = 0.59\bar{U}_\infty$ calculated above, the critical layer y_c is estimated from the mean velocity profile, such that $\bar{U}(y_c) = \tilde{c}$, to be 0.072δ ($y_c^+ \approx 68$) at station-1. The critical layer location is indicated throughout in all relevant figures by a dashed line.

The peak amplitude of the synthetic mode is expected to occur in the vicinity of its critical layer ([McKeon & Sharma, 2010](#)). Judging by the proximity of y_c to the wall-normal peak in \tilde{u} (see figures 3.3 and 3.8), the estimate of $y_c = 0.072\delta$ can be considered as fairly good. However, it is important to note its sensitivity to \tilde{k}_x due to the sharp mean velocity gradient in the region of interest. A slight uncertainty in the estimation of \tilde{k}_x (and hence \tilde{c}), possibly due to the finite number of phase-averaging cycles, can result in a significant change to y_c . The variation in $\tilde{\lambda}_x$ of $0.7\delta_1$ seen in table 3.1 is used to arrive at an estimate on the uncertainty in y_c . By taking $\pm 0.7\delta_1$ to be the error in the estimate of $\tilde{\lambda}_x$ in section 3.2.1, the *true* critical layer is worked out to lie somewhere in the region $0.056\delta < y < 0.093\delta$, with a corresponding wavespeed range of $0.56\bar{U}_\infty < \tilde{c} < 0.61\bar{U}_\infty$.

3.2.3 Synthetic Mode as a VLSM Proxy

Very-large-scale motions show a distinct peak in the velocity power spectrum at higher Reynolds numbers ($Re_\tau \gtrsim 4000$), and have been previously observed to have streamwise lengths of 15δ to 20δ (Hutchins & Marusic, 2007b). Single-point measurements underestimate the streamwise length scale of these motions due to their meandering nature; the VLSM spectral signature from single-point measurements scales is found to scale in outer units as $\lambda_x \approx 6\delta$ (Hutchins & Marusic, 2007a). Mathis *et al.* (2009a) observed the wall-normal spectral peak of the VLSM motions at $y^+ \approx 3.9 Re_\tau^{1/2}$, and associated it with the center of the log-region. The exact location, strength, and wavelength of the VLSM-class motions at very high Reynolds numbers is still an open issue (Vallikivi *et al.*, 2015), but for the purposes of the present discussion we take the streamwise wavelength of the VLSM peak to be of $\mathcal{O}(10\delta)$ and centered at $y^+ \approx 3.9 Re_\tau^{1/2}$ following Mathis *et al.* (2009a); this location is indicated in figure 3.2 for reference. It is to be noted that a distinct VLSM spectral signature, or a peak, cannot be seen in the present data as the Reynolds number is not sufficiently high. Following Hutchins *et al.* (2011) the convection velocity (or wavespeed) of these motions is taken as the local mean velocity at the indicated wall-normal location, and is found to be $0.65 \bar{U}_\infty$ for the present flow. The streamwise length scale and wavespeed of the synthetic mode from sections 3.2.1 and 3.2.1 are seen to have a close correspondence to the above estimates of the natural VLSM. Therefore, the synthetic mode can be viewed as a *deterministic* spanwise-constant VLSM in the flow. The analysis presented in the rest of this chapter attempts to generalize large-scale influences on small-scale turbulence utilizing the synthetic VLSM, referred to as the synthetic large scale.

Before proceeding to the next section, the following remark is important. Along with the large-scale mode, multiple spatial and temporal small scales are excited by the static roughness effect of the wall perturbation in the immediate downstream region. The artifacts of this effect can be seen in the data of Jacobi & McKeon (2011b) where non-linear growth in the phase of the synthetic mode was observed in the region $x < 1\delta$ downstream of the perturbation. For $x > 1\delta$, the synthetic scale showed a normal mode behavior with a linear change in phase with streamwise distance. Given the relatively weaker roughness strength of the perturbation in the present experiment, any small-scale activity directly excited by the rib is expected to decay rapidly; evidence for the same can be seen in the difference spectra of figure 3.2. Thus, the flow is thought to be dominated by the synthetic large scale in the region of measurements ($x \geq 2.7\delta$); any remnants of the direct influence from the wall perturbation on the small scales are considered insignificant. Note that this justified assumption is implicit in the phase-averaging scheme (section 3.2.1) that gives \tilde{k}_x for the synthetic scale.

3.3 Modified Large- and Small-Scale Phase Relations

We now examine the nature of large- and small-scale phase relations in the flow through the skewness and amplitude modulation co-efficient (Mathis *et al.*, 2009a) statistics of the turbulent velocity fluctuations. Firstly, by considering a general statistical signal, both quantities are shown to be measures of phase in triadic wavenumber interactions. The experimental results are then interpreted accordingly to understand the synthetic large-scale influence on the phase relations in the forced turbulent boundary layer.

3.3.1 Skewness

We begin our analysis by considering a general statistically homogeneous (or statistically stationary when considered in temporal domain) real velocity signal $u(x)$ in the streamwise direction x (note that the notation u used earlier in the context of experimental data is retained here in a more general setting). As this analysis is later applied to data from single-point measurements, u is taken as a single-variable function (x in this case) for simplicity. Performing a multi-scale decomposition on the signal using a Fourier basis, with wavenumbers k_i and corresponding amplitudes and phases α_i and ϕ_i respectively, we write

$$u(x) = \alpha_1 \cos(k_1 x + \phi_1) + \alpha_2 \cos(k_2 x + \phi_2) \dots + \alpha_i \cos(k_i x + \phi_i) + \dots \quad (3.3)$$

with $0 < k_1 < k_2 < \dots < k_i < \dots < k_\infty$,

where k_1 and k_∞ denote the largest and smallest length scales in u respectively (figure 3.4). With σ denoting the standard deviation of u , skewness S of the signal forms the following triple sum

$$\begin{aligned} \sigma^3 S = \langle u^3 \rangle &= \left\langle \sum_{l=1}^{\infty} \sum_{m=1}^{\infty} \sum_{n=1}^{\infty} \alpha_l \alpha_m \alpha_n \cos(k_l x + \phi_l) \cos(k_m x + \phi_m) \cos(k_n x + \phi_n) \right\rangle \\ &= \sum_{l=1}^{\infty} \sum_{m=1}^{\infty} \sum_{n=1}^{\infty} \alpha_l \alpha_m \alpha_n \langle \cos(k_l x + \phi_l) \cos(k_m x + \phi_m) \cos(k_n x + \phi_n) \rangle. \end{aligned} \quad (3.4)$$

Using the orthogonal property of the Fourier basis, it is straightforward to show that only triadic combinations of wavenumbers k_l, k_m, k_n with $k_l = k_n - k_m$ and wavenumber pairs k_l, k_n with $k_n = 2k_l$ make a non-zero contribution to S (see appendix A.1). Note that here we assume $k_l < k_m < k_n$

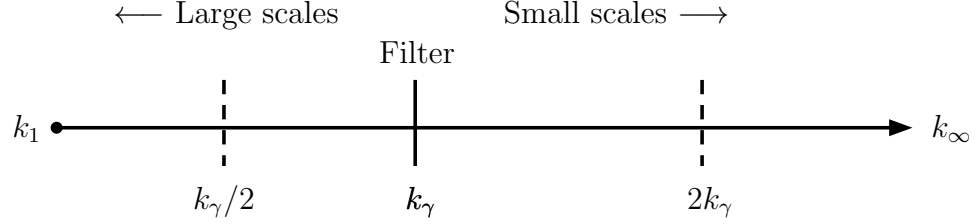


FIGURE 3.4: A schematic of the wavenumber line showing the large- and small-scale regions. k_γ indicates the filter cut-off location.

without a loss of generality. S can then be reduced to the following form:

$$S = \frac{6}{4\sigma^3} \sum_{\substack{\forall l,m,n \\ k_l < k_m < k_n \\ k_l + k_m = k_n}} \alpha_l \alpha_m \alpha_n \cos(\phi_l + \phi_m - \phi_n) + \frac{3}{4\sigma^3} \sum_{\substack{l=1 \\ k_n = 2k_l}}^{\infty} \alpha_l^2 \alpha_n \cos(2\phi_l - \phi_n). \quad (3.5)$$

From the above equation it is seen that skewness is nothing but a weighted (by mode amplitudes) and normalized (by σ^3) sum of the quantity $\cos(\phi_l + \phi_m - \phi_n)$ over all sets of triads and wavenumber pairs. By considering amplitude modulation coefficient next, it will be readily seen that the quantity $\cos(\phi_l + \phi_m - \phi_n)$ is a measure of the phase difference between the large-scale (lower wavenumber) mode $\cos(k_l x + \phi_l)$ and the envelope of the small-scale (higher wavenumbers) modes $\cos(k_m x + \phi_m)$ and $\cos(k_n x + \phi_n)$.

3.3.2 Amplitude Modulation Coefficient

The procedure to calculate R as outlined by [Mathis *et al.* \(2009a\)](#) is followed here, but with a slight departure in the enveloping technique which is explained below. Firstly, the velocity signal u is split into large- and small-scale components using a spatial Fourier filter at a set wavenumber, arbitrarily chosen as k_γ (see figure 3.4). We then have the large- and small-scale velocity signals u_L and u_S as

$$\begin{aligned} u_L &= \alpha_1 \cos(k_1 x + \phi_1) \dots + \alpha_l \cos(k_l x + \phi_l) \dots + \alpha_{\gamma-1} \cos(k_{\gamma-1} x + \phi_{\gamma-1}), \\ u_S &= \alpha_\gamma \cos(k_\gamma x + \phi_\gamma) \dots + \alpha_m \cos(k_m x + \phi_m) \dots + \alpha_n \cos(k_n x + \phi_n) + \dots \end{aligned} \quad (3.6)$$

Here again we assume without a loss of generality that $k_l < k_\gamma < k_m < k_n$. Next, an envelope function $\mathcal{E}(x)$ for the small-scale velocity signal is obtained using the Hilbert transform. [Mathis](#)

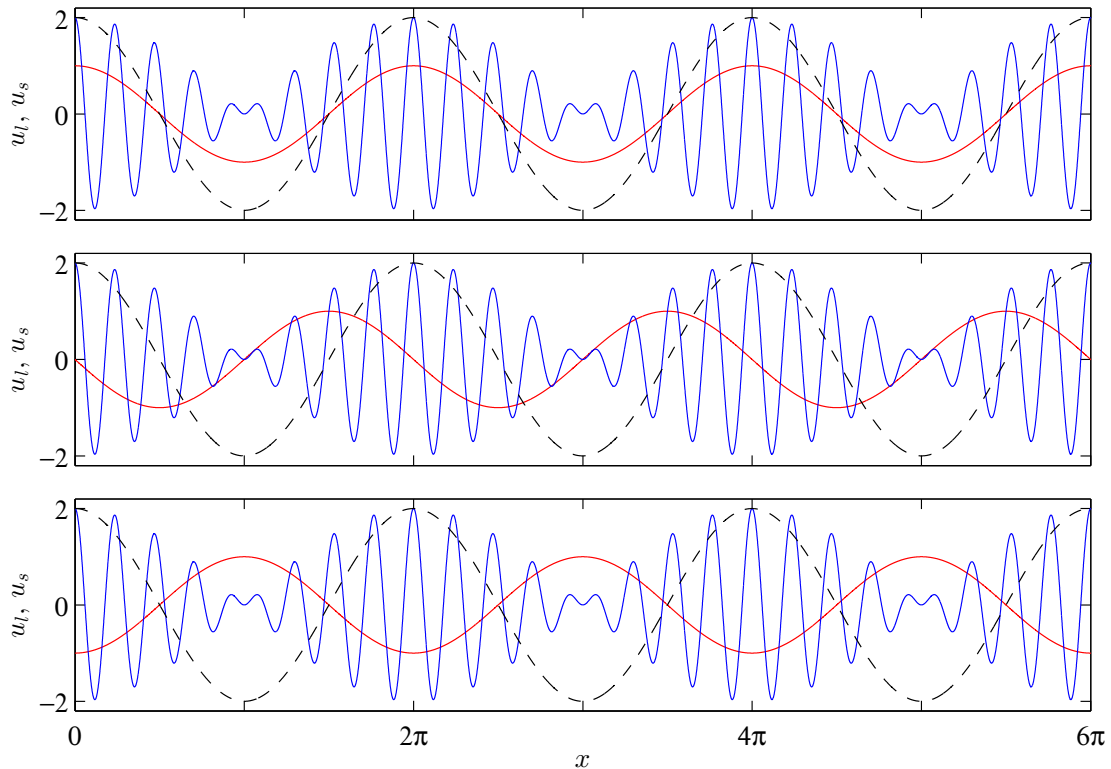


FIGURE 3.5: Example shows phase relations between large- and small-scale velocity components for a signal containing a set of three triadically consistent wavenumbers, taken to be $k_1 = 1$, $k_2 = 8$, $k_3 = 9$ for illustration. Wavenumber k_1 constitutes the large-scale component (red curve) written as $u_l = \cos(k_1 x + \phi_1)$, and wavenumbers k_2, k_3 constitute the small-scale component (blue curve) written as $u_s = \cos(k_2 x + \phi_2) + \cos(k_3 x + \phi_3)$; dashed curve denotes the envelope of the small-scale signal \mathcal{E} (see section 3.3.2). Three different values of $0, \pi/2$, and π are chosen for $\Delta\phi = \phi_1 + \phi_2 - \phi_3$ in the top, center, and bottom panel examples respectively. The corresponding values of the amplitude modulation coefficient $R = \cos(\phi_l + \phi_m - \phi_n)$ are 1, 0, and -1 for the three cases.

et al. (2009a) use the analytic signal modulus A , given by $A(x) = \sqrt{u_S^2(x) + \mathcal{H}^2(x)}$ where $\mathcal{H}(x)$ is the Hilbert transform of $u_S(x)$, as an envelope of the small-scale activity. Here we take A^2 to be our envelope function, *i.e.* $\mathcal{E}(x) = A^2(x)$. This allows for a more direct interpretation of the final result in terms of phase in triadic interactions. For the purposes of forming a correlation coefficient, as done in the calculation of R , $A^2(x)$ is a valid proxy for $A(x)$. As R is a normalized measure, no significant differences are expected in its value between the cases of $A(x)$ and $A^2(x)$ being used as the envelope function, and this was easily verified with experimental data (see figure A.1 in appendix). The envelope \mathcal{E} is subject to a large-scale-pass filter with the same cut-off wavenumber k_γ used in equation 3.6, and the filtered envelope function is denoted by \mathcal{E}_L . Finally, a correlation coefficient is formed between the large-scale velocity signal (u_L) and the large-scale component of the small-scale envelope (\mathcal{E}_L), written as

$$R = \frac{\langle u_L \mathcal{E}_L(u_S) \rangle}{\sqrt{\langle u_L^2 \rangle} \sqrt{\langle \mathcal{E}_L(u_S)^2 \rangle}}. \quad (3.7)$$

Starting with equation 3.6, the above described procedure is followed with further simplifications (see appendix A.1) to reduce the expression for the amplitude modulation coefficient to the following form

$$R = \frac{1}{\Omega} \sum_{\substack{\forall l, m, n \\ k_n - k_m = k_l \\ 0 < k_l < k_\gamma \\ k_m, k_n > k_\gamma}} \alpha_l \alpha_m \alpha_n \cos(\phi_l + \phi_m - \phi_n), \quad (3.8)$$

where $\Omega = \sqrt{\langle u_L^2 \rangle \langle \mathcal{E}_L^2 \rangle}$ is the normalization factor for the covariance $\langle u_L \mathcal{E}_L \rangle$. As in the case of S (equation 3.5), only triadic interactions between wavenumbers make a non-zero contribution to R .

As noted by Chung & McKeon (2010), the amplitude modulation coefficient, which is essentially a normalized dot product between two quantities, can be interpreted as a measure of the phase difference between them. That is, if \vec{a} and \vec{b} are two vectors in general with an included angle φ , then $\vec{a} \cdot \vec{b} = |\vec{a}| |\vec{b}| \cos(\varphi)$. The sense of the phase relationship (the sign of φ) is lacking here due to the symmetry of the cosine function. As the value of R varies from 1 to -1, it implies the relative phase between large- and small-scale signals varies from 0 to π respectively, with the value of $R = 0$ corresponding to a phase difference of $\pi/2$. Following this, it is easily seen from equation 3.8 that the quantity $\phi_l + \phi_m - \phi_n = \Delta\phi$ is the phase difference between the large-scale k_l and the envelope of the triadic small-scales k_m, k_n . Thus R can be interpreted as an amplitude-weighted (and normalized) phase measure $\cos(\Delta\phi)$ of all triadic interactions where the large-scale and the two triadic small-scales fall on either side of the filter cut-off. Figure 3.5 illustrates this by considering an example of a signal consisting of three triadically consistent wavenumbers components.

Notice that skewness (equation 3.5) is also a measure of the same phase quantity, but over all triadic interactions without any filter restrictions. The similarity between S and R was first pointed out by Sharma & McKeon (2013) for a single triad, *i.e.* a single set of three triadically consistent wavenumbers. Although S and R exhibit similar trends with wall-normal height in a turbulent boundary layer (Mathis *et al.*, 2009a; Schlatter & Örlü, 2010), it is easy to see from equations 3.5 and 3.8 that differences exist between the two. This is discussed in the following subsection, and an exact relationship is established between the two phase measures.

3.3.3 Connection between Skewness and Amplitude Modulation Coefficient Statistics

There are significant differences between measured values of S and R in the near-wall and the outer wake regions of a turbulent boundary layer (see for instance [Mathis *et al.*, 2011](#), figure 1). These differences can be understood by a direct comparison of equations 3.5 and 3.8; S accounts for triadic and wavenumber pairs interactions over the entire wavenumber range, whereas R accounts for only those triadic interactions that occur across the filter cut-off location k_γ . Also, the weights and normalization factors for triadic interactions in S and R are different. The triadic and wavenumber pair interactions captured by S but not by R can be accounted for by considering the three quantities $\langle u_S^3 \rangle$, $\langle u_L^3 \rangle$, $\langle u_L^2 u_S \rangle$, as explained below with reference to the schematic shown in figure 3.4.

- $\langle \mathbf{u}_S^3 \rangle$: u_S only contains velocity scales with wavenumbers greater than k_γ , hence $\langle u_S^3 \rangle$ captures all triadic and wavenumber pair interactions to the right of the filter. This is similar to $\langle u^3 \rangle$, but $\langle u^3 \rangle$ captures those interactions across the entire wavenumber line whereas $\langle u_S^3 \rangle$ is band-limited, and likely to be most active close to the wall.
- $\langle \mathbf{u}_L^3 \rangle$: u_L only contains velocity scales with wavenumbers smaller than k_γ , hence $\langle u_L^3 \rangle$ captures triadic interactions to the left of the filter where the two smaller wavenumbers are less than $k_\gamma/2$, and wavenumber pair interactions for all wavenumbers k_l, k_n such that $k_n = 2k_l$ and $k_l < k_l < k_\gamma/2$. Larger scale activity is most prevalent in the wake region.
- $\langle \mathbf{u}_L^2 \mathbf{u}_S \rangle$: with workings similar to S and R in equations 3.5 and 3.8 respectively, it can be shown that $\langle u_L^2 u_S \rangle$ reduces to the following form

$$\langle u_L^2 u_S \rangle = \frac{1}{2} \sum_{\substack{\forall l, m, n \\ k_l < k_m < k_\gamma < k_n \\ k_\gamma/2 < k_m \\ k_l + k_m = k_n}} \alpha_l \alpha_m \alpha_n \cos(\phi_l + \phi_m - \phi_n) + \frac{1}{4} \sum_{\substack{l=\gamma/2 \\ k_n=2k_l}}^{\gamma} \alpha_l^2 \alpha_n \cos(2\phi_l - \phi_n). \quad (3.9)$$

The first term on the RHS captures triadic interactions where the intermediate wavenumber necessarily lies in between $k_\gamma/2$ and k_γ , and the second term captures wavenumber pair interactions for all wavenumbers k_l, k_n such that $k_n = 2k_l$ and $k_\gamma/2 < k_l < k_\gamma$.

From the above descriptions of $\langle u_S^3 \rangle$, $\langle u_L^3 \rangle$, $\langle u_L^2 u_S \rangle$, it is seen that the three quantities exactly capture the triadic and wavenumber interactions accounted for by S and missed by R . An analytical relationship can now be established between S and R ; balancing the weights between S , R , $\langle u_S^3 \rangle$, $\langle u_L^3 \rangle$, $\langle u_L^2 u_S \rangle$ gives

$$\sigma^3 S = 1.5 \Omega R + \langle u_S^3 \rangle + \langle u_L^3 \rangle + 3 \langle u_L^2 u_S \rangle. \quad (3.10)$$

The RHS terms have a clear resemblance to scale-decomposed skewness factor, but with a scaled version of R replacing the term $3 \langle u_L u_S^2 \rangle$. This confirms the suggestion of Mathis *et al.* (2011) that the cross-term $3 \langle u_L u_S^2 \rangle$ can be used as an alternative or complementary diagnostic tool to R .

It is worth noting that the analysis presented thus far makes no assumptions regarding the underlying dynamics of the system that generates the signal u . Hence equation 3.10 is applicable to any statistically homogeneous (or stationary) signal in general. This helps in understanding the results of the amplitude modulation coefficient presented by Mathis *et al.* (2009a) and Schlatter & Örlu (2010) for synthetic *turbulence* signals. Mathis *et al.* (2009a) show that $R(y)$ is nearly zero when phase information is randomly scrambled in velocity signals obtained from a turbulent boundary layer. By assigning random phases to different scales, we expect on average the number of large scales with the corresponding envelopes of two triadically interacting small-scales in phase ($\Delta\phi = 0$) and out of phase ($\Delta\phi = \pi$) to be equal, and hence $R(y) \approx 0$. Schlatter & Örlu (2010) consider synthetic signals with matched PDFs to real turbulent signals but with no scale (amplitude) information contained in them. However, by matching the PDF (and hence skewness), they retain the phase information contained in the real signal. Although all amplitude information is removed from the signal, as R is a normalized measure, it is not surprising to see that there is a good match between $R(y)$ calculated from their real and synthetic signals.

From the above analysis it is seen that the amplitude modulation effect in wall turbulence can be naturally interpreted in terms of phase relations between tradically consistent scales. This interpretation also extends to the observations of small-scale frequency modulation in the near-wall region of a turbulent boundary layer (Ganapathisubramani *et al.*, 2012). For flows in a statistically stationary state, the amplitude associated with each scale is invariant in space and time (equation 3.3). In essence, the so called amplitude and frequency modulation effects are simply measures of the relative placement (or arrangement) of various scales in the flow. Modulation in a strict sense implies a dynamical connection between scales, and requires a more advanced framework (based on the governing equations) for a full description.

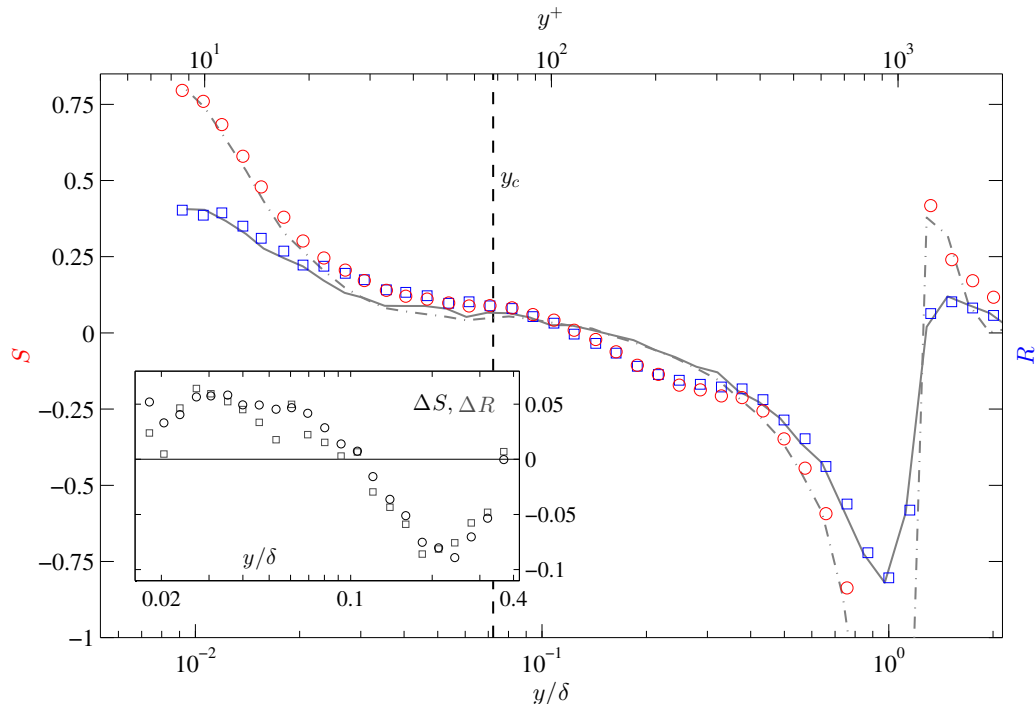


FIGURE 3.6: Skewness S (round markers) and amplitude modulation coefficient R (square markers) profiles for flow with single mode forcing at station-1. Canonical flow skewness (dash-dot line) and amplitude modulation coefficient (solid line) data are also shown for comparison. Inset plot shows the difference between the forced and canonical flows for both the statistics (ΔS , ΔR) in the region $0.02 < y/\delta < 0.4$.

3.3.4 Synthetic Large-Scale Effects on Small Scales

The skewness and amplitude modulation coefficient statistics are now used to infer the effects of the synthetic large scale (characterized earlier in section 3.2) on the natural phase relations in the flow. For the purposes of calculating R , a Fourier filter with cut-off at $\lambda_\gamma = 5\delta$ was chosen to separate the large- and small-scale components. A clear separation between the energetic small scales and the synthetic large scale is seen at all y for this choice of the filter cut-off (figure 3.2). While the choice of $\lambda_\gamma = 5\delta$ is somewhat subjective, it is easily demonstrated from experimental data that the correlation coefficient R is insensitive to the exact value of the filter cut-off (see figure A.2 in appendix).

Skewness and amplitude modulation coefficient profiles are shown in figure 3.6 for canonical and forced flows at station-1. For the canonical flow, the behavior of S and R with wall-normal distance y implies that large- and small-scales are close to being in phase ($S, R > 0$) near the wall, and gradually move towards being out of phase ($S, R < 0$) approaching the boundary layer edge; this trend is consistent with observations in previous literature.

The forced flow contains the synthetic large scale at wavenumber \tilde{k} ($= \tilde{\omega}/\tilde{c}$) in addition to the other turbulence scales. That is, $\tilde{u} = \tilde{\alpha} \cos(\tilde{k}x + \tilde{\phi})$ is added to $u(x)$ in equation 3.3. In the presence of the synthetic scale, the values of S and R are altered significantly, particular in the wall-normal region where the synthetic scale is active. There is a marked increase in the values of S and R in the region $0.02\delta < y < 0.1\delta$ and decrease in the region $0.1\delta < y < 0.4\delta$ in presence of the synthetic large-scale. The cross-over location $y/\delta \approx 0.1$ corresponds well to the synthetic mode peak location (see figure 3.8), and is close to the estimated critical layer location y_c . The results in figure 3.6 suggest that the synthetic large-scale drives the envelope of all small-scales towards being in and out of phase with it below and above its critical layer location respectively, thereby altering the natural large- and small-scale phase relationships in the flow. This can interpreted in the context of strengthening of the natural VLSMs, and its small-scale modulation effect, with increasing Reynolds number (Mathis *et al.*, 2009a); the synthetic large scale generalizes this effect in the present scenario.

It is to be noted that quantities S and R reveal the action of the synthetic scale, in conjunction with the large-scale activity naturally present in the flow, on the small scales *i.e.* the large-scale signal u_L includes the synthetic scale \tilde{u} and other natural large scales present in the flow. While a noticeable effect of the synthetic scale is seen on the envelope of all small scales (as quantified by S and R), a stronger influence is expected on the small scales that directly couple to the synthetic scale through non-linear triadic interactions. This is examined in the following section by suitably defining a small-scale envelope and studying a modified correlation coefficient similar to R .

3.4 Organization of Directly-Coupled Small Scales

Any two small-scale wavenumbers $k_n, k_m (> k_\gamma)$ that are triadically consistent with \tilde{k} ($= \tilde{\omega}/\tilde{c}$) have a direct dynamical coupling with the synthetic scale. Thus the influence of external forcing at wavenumber \tilde{k} can be expected to have a prominent manifestation among wavenumber pairs k_n, k_m that satisfy the triadic condition $k_n - k_m = \tilde{k}$. Consider a velocity signal written as $u_{mn}(x) = \alpha_m \cos(k_mx + \phi_m) + \alpha_n \cos(k_nx + \phi_n)$ for a specific set of specific small-scale triadic wavenumbers k_m, k_n . Following section 3.3.2, an envelope function $A_{mn}(x)$ for u_{mn} can be formulated as the square of the analytic function modulus, *i.e.* $A_{mn}(x) = u_{mn}^2(x) + \mathcal{H}_{mn}^2(x)$, where \mathcal{H}_{mn} is the

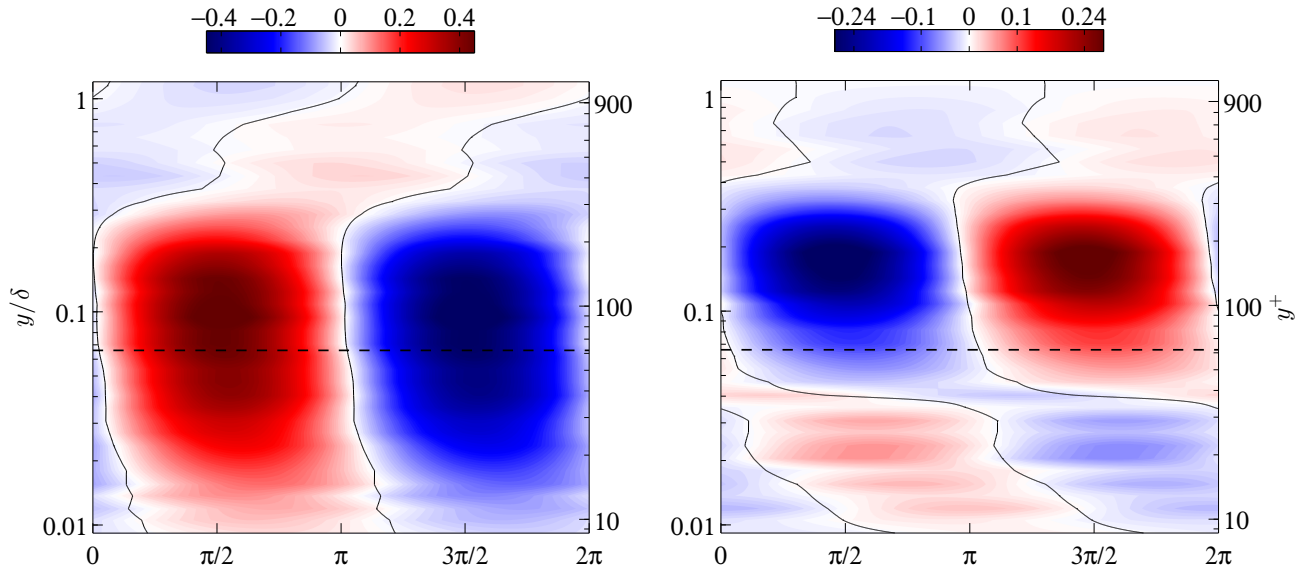


FIGURE 3.7: A comparison of the synthetic mode shape $\tilde{u}(y, t)$ (left panel, reproduced here from figure 3.3) with the average triadic envelope $\tilde{\mathcal{E}}(y, t)$ (right panel) at station-1. Solid lines are zero-level contours, and the dashed lines indicate the critical layer y_c .

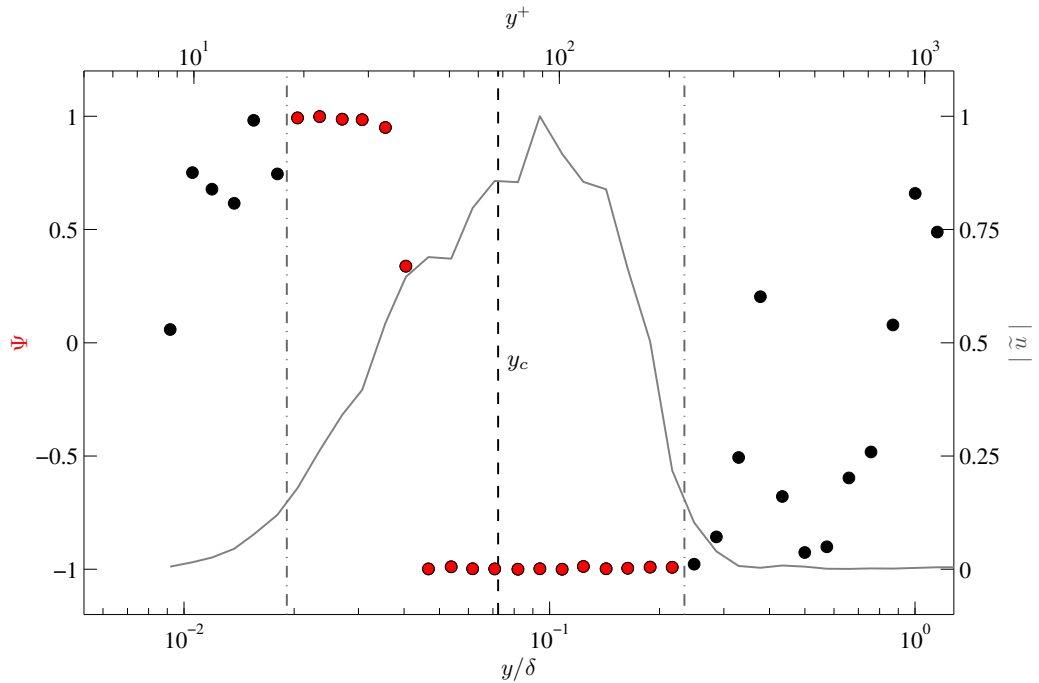


FIGURE 3.8: Correlation coefficient $\Psi(y)$ (round markers) and normalized synthetic mode energy $\langle (\tilde{u})^2 \rangle(y) / \langle (\tilde{u})^2 \rangle_{\max}$, denoted by $|\tilde{u}|$ (solid line), at station-1. The dash-dot lines indicate the wall-normal locations where the synthetic mode energy drops to 15% of its maximum value; the markers for Ψ are highlighted in red in the region between the 15%-energy reference lines.

Hilbert transform of u_{mn} . After removing the mean term, A_{mn} reduces to the following form (see appendix A.2):

$$\begin{aligned} A_{mn}(x) &= 2\alpha_m\alpha_n \cos[(k_n - k_m)x + \phi_n - \phi_m] \\ &= 2\alpha_m\alpha_n \cos[\tilde{k}x + \phi_n - \phi_m]. \end{aligned} \quad (3.11)$$

We now consider the entire small-scale velocity signal u_S , consisting of scales from wavenumbers k_γ to k_∞ , and perform the following procedure to extract an average envelope function over all k_n, k_m components in u_S that satisfy the triadic condition with the synthetic scale \tilde{k} . u_S is squared and phase-averaged with respect to the forcing signal (following the phase-averaging procedure described in section 3.2) to obtain the function (see appendix A.2), denoted by $\tilde{u}_S^2(x) = \tilde{\mathcal{E}}(x)$,

$$\tilde{\mathcal{E}} = \sum_{\substack{\forall m,n \\ k_n - k_m = \tilde{k} \\ k_m, k_n > k_\gamma}} \alpha_m\alpha_n \cos(\tilde{k}x + \phi_n - \phi_m). \quad (3.12)$$

The phase averaging procedure picks out the \tilde{k} component from u_S^2 . A straightforward comparison between equations 3.11 and 3.12 reveals that, in essence, $\tilde{\mathcal{E}}$ captures the amplitude-weighted average phase of the triadic envelope across all sets of small-scale wavenumbers that couple directly with the synthetic scale.

The triadic envelope $\tilde{\mathcal{E}}$ calculated using experimental data, with the same filter as earlier with cut-off at $\lambda_\gamma = 5\delta$, is shown along with the synthetic large scale \tilde{u} in figure 3.7. A certain correlation between \tilde{u} and $\tilde{\mathcal{E}}$ can be seen by just a visual comparison. The two quantities are in phase close to the wall, and out of phase away from it following an abrupt jump of π radians in the phase of $\tilde{\mathcal{E}}$ close to the critical layer location. The phase relationship can be analyzed in a quantitative manner by defining a correlation coefficient Ψ between \tilde{u} and $\tilde{\mathcal{E}}$, akin to the amplitude modulation coefficient,

$$\Psi = \frac{\langle \tilde{u} \tilde{\mathcal{E}} \rangle}{\langle \tilde{u}^2 \rangle^{1/2} \langle \tilde{\mathcal{E}}^2 \rangle^{1/2}}. \quad (3.13)$$

It is to be noted that R gives the average phase difference between all large- and small-scales in the flow (including the synthetic scale when present), whereas Ψ is a measure of the phase between the synthetic scale and the average triadic envelope of small-scales that are in direct coupling. Thus Ψ represents the coupling due to one wavenumber within the broader u_L . $\Psi(y)$ at station-1 is shown in figure 3.8 along with the normalized energy of the synthetic large-scale. The wall-normal locations where the synthetic large-scale energy drops to 15% of its peak value are shown by dash-dot lines

for reference; the region between these lines is where effects of the synthetic large-scale are expected to dominate. As the energy in the synthetic mode drops close to zero, the correlation coefficient Ψ becomes noisy (outside the 15%-energy reference lines). A clear phase-locking, or organization effect in phase of directly coupled small-scales by the synthetic large-scale is seen in the region where the synthetic scale is active. The triadic small-scales are exactly in phase with the synthetic large-scale ($\Psi = 1$) near the wall and exactly out of phase ($\Psi = -1$) away from the wall; a sharp phase jump of π radians occurs at $y = 0.04\delta$, close to the estimated critical layer location. The phase behavior of the directly coupled small-scales is consistent with the altered large and small-scale phase relationship suggested by skewness and amplitude modulation coefficient.

It is interesting to note that the results presented here are connected in a broad manner to earlier work in the area of Homogeneous Isotropic Turbulence (HIT). [Brasseur & Wei \(1994\)](#) categorize triadic scale interactions in a HIT setting into two classes: (1) *local-to-non-local* interactions with a separation between scales of a decade or less; (2) *distant* interactions between disparate scales with a separation larger than a decade at the least. The *distant* class of scale interactions are found to have negligible transfer of energy directly from large- to small-scales, but have a significant influence on the small-scale structure. *Distant*, or long-range, scale interactions were studied by [Yeung & Brasseur \(1991\)](#) and [Yeung et al. \(1995\)](#) through numerical experiments where coherent narrow-band anisotropic forcing was imposed at the large scales. The triadic small scales were found to have a direct response in terms of anisotropic energy redistribution, and phase correlations with the large-scale forcing. Although the non-homogeneous nature of the flow in the present case introduces additional dynamics into play and requires further considerations, it is not entirely surprising to see broadly similar interactions between large- and small-scales as the key non-linear element governing scale coupling in both flow scenarios comes from the same governing equation.

Chapter 4

Double-Mode Forcing of the Turbulent Boundary Layer

The nature of bulk interactions between large- and small-scales was investigated in the previous chapter using data from the first set of experiments, where a single large-scale mode was artificially excited in the flow. The focus in the present chapter shifts towards exploring the direct triadic wavenumber responses resulting from the interaction of two synthetic modes. The double-frequency wall perturbation used in the second set of experiments (described in section 2.2.2) excites two coherent large-scale spanwise-constant velocity fluctuations in the downstream region with well defined spatial and temporal scales. The two spatio-temporal modes and their corresponding triadic response modes are characterized here. Triadic consistency between modes is experimentally demonstrated in both streamwise and temporal wavenumbers. The ideas related to phase relations developed previously in sections 3.3 and 3.4 are used here to understand the phase coupling between specific triads. A connection to the resolvent operator framework is made towards the end in section 4.4.

4.1 Flow Statistics and Power Spectrum

The mean velocity and turbulence intensity profiles for flow with double-mode forcing at station-1 ($x = 2.7\delta_1$) are compared with corresponding canonical and single-mode forcing flow data in figure 4.1. As expected, the relative increase in wall-normal amplitude of the perturbation from the previous experiment (see figure 2.5 for a comparison) produces a slightly higher mean momentum deficit, visible around $y = 0.1\delta$. However, the relatively stronger perturbation does not affect the boundary layer thickness and no significant change in Re_θ (and Re_τ) was noticed. As noted previously, the estimate of Re_τ is strictly applicable only to a canonical flow; the use of viscous scaling in y is continued in figures of this chapter as it provides a useful reference.

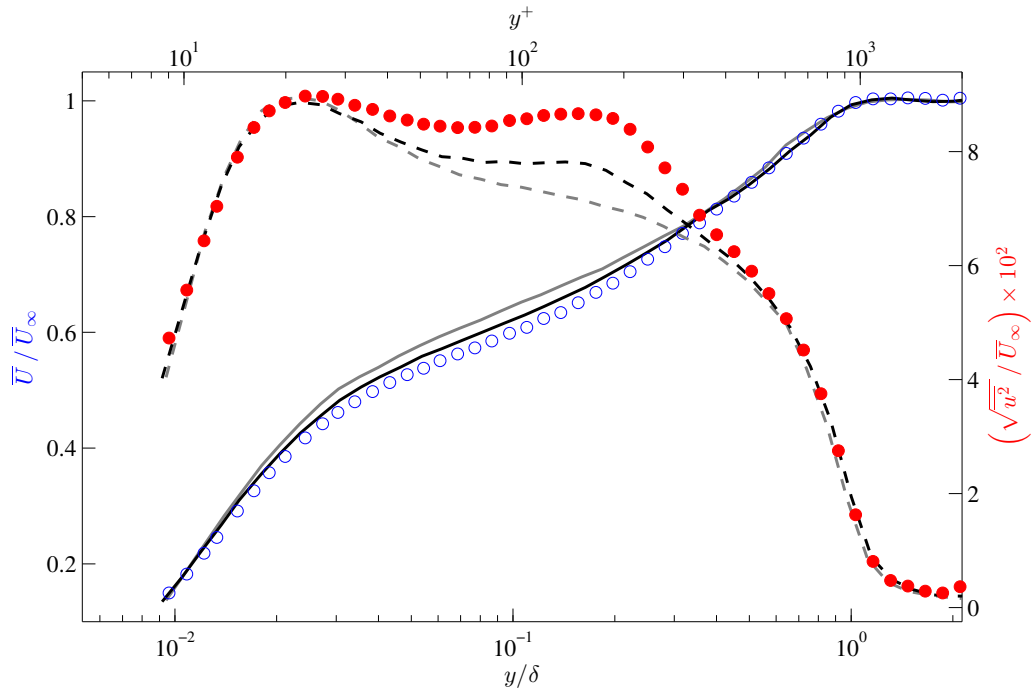


FIGURE 4.1: Mean velocity (open markers) and turbulence intensity (filled markers) profiles for flow with double-mode forcing at station-1. Canonical flow mean velocity (solid grey curve) and intensity (dashed grey curve) data from figure 2.7, and single-mode forced flow mean velocity (solid black curve) and intensity (dashed black curve) data from figure 3.1 are also shown for comparison.

The energetic hump in the turbulence intensity seen between $y \approx 0.03\delta$ and $y \approx 0.4\delta$ can be understood from the power spectral density Φ_u^{f2} (superscript $f2$ denotes double-mode forcing) shown in figure 4.2. The presence of two energetic synthetic scales can be clearly seen in the form of narrow-band streaks in the large-scale region of the spectrum. The two bands correspond to the forcing frequencies of 50 Hz and 35 Hz projected onto the streamwise direction x using the local mean velocity \bar{U}_∞ . The corresponding temporal wavenumbers of the two scales are given by $\tilde{\omega}_1 = 0.24\bar{U}_\infty\delta^{-1}$ and $\tilde{\omega}_2 = 0.17\bar{U}_\infty\delta^{-1}$ respectively. The difference spectra in the figure reveal that the dominant change brought in the flow by the forcing is the excitation of the synthetic scales.

From results presented in the previous chapter, the energetic large-scale activity excited by the perturbation is expected to have a strong influence on the small-scale turbulence. In addition to those effects, it is important to note that the increased wall perturbation strength also plays a role in the present case. The ‘stress bore’ generated by the static roughness effects can have a direct influence on the small scales as demonstrated by [Jacobi & McKeon \(2011a\)](#). These effects are not treated explicitly as the focus here is on understanding the dynamic forcing effects, in particular the direct triadic responses ensuing from the non-linear interaction of the two synthetic scales.

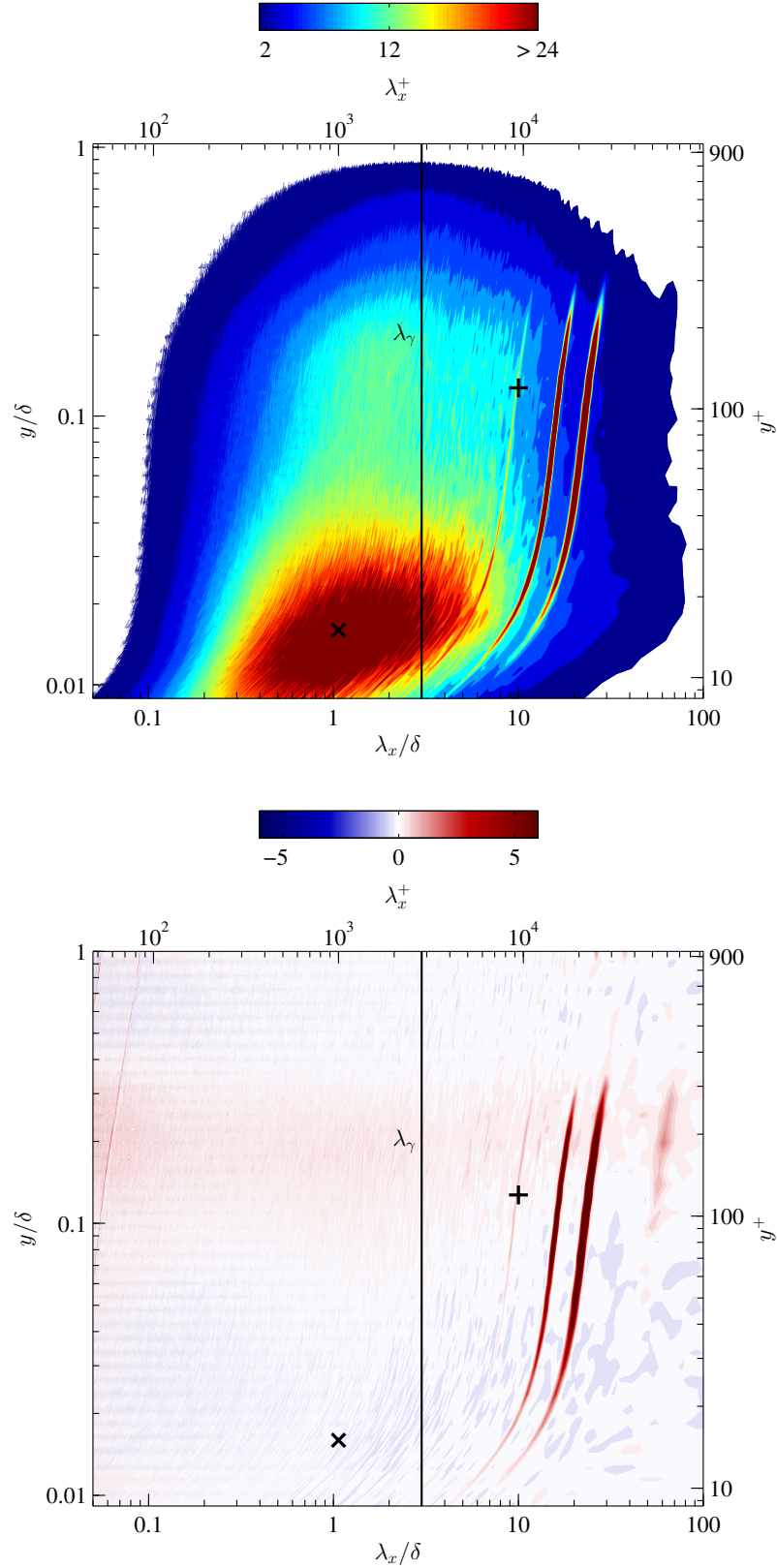


FIGURE 4.2: Top panel shows pre-multiplied power spectral density $(k_x \delta / \bar{U}_\infty^2) \Phi_u^{f2} \times 10^6$, and the bottom panel shows the normalized difference in power levels $(\Phi_u^{f2} - \Phi_u^c) / \Phi_u^c$ between the forced and canonical (figure 2.8) flows at station-1. In both panels, ‘x’ and ‘+’ denote the vicinity of the expected near-wall cycle and VLSM (see section 3.2.3) peaks respectively. The new filter cut-off (see section 4.3) at $\lambda_\gamma = 3\delta$ is marked by the solid vertical line.

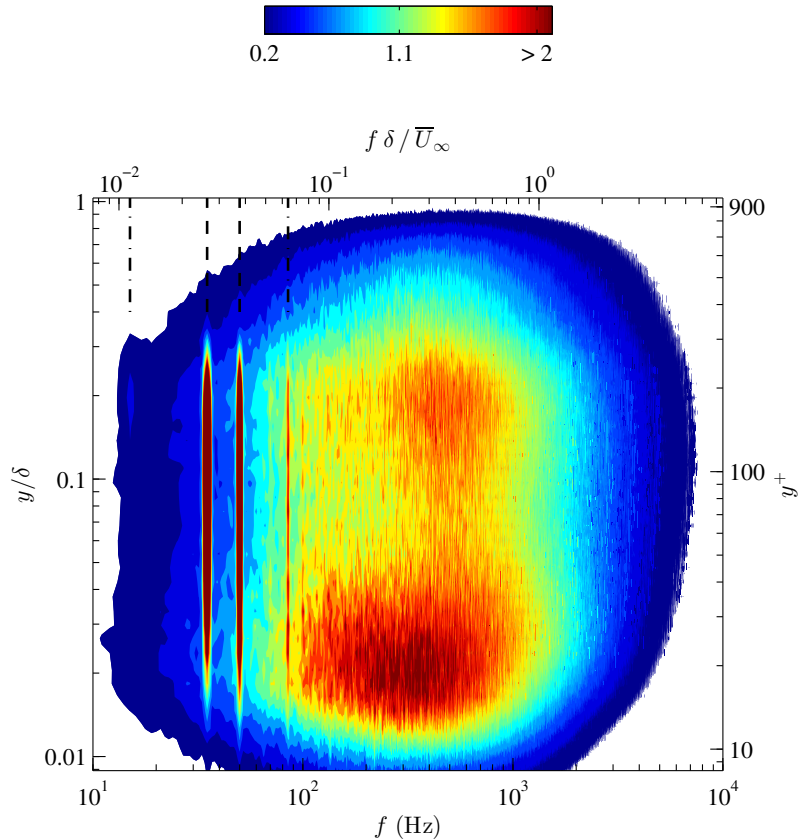


FIGURE 4.3: Pre-multiplied power spectral density $\left(f/\overline{U}_\infty^2\right) \Phi_u^{f^2} \times 10^3$. The vertical dashed lines indicate forcing frequencies of 35 Hz and 50 Hz, and the dash-dot lines indicate triadic response frequencies of 15 Hz and 85 Hz for reference.

4.1.1 Triadic Responses in Frequency Space

A close inspection of figure 4.2 reveals narrow-band activity in regions to the left and right of the two forcing frequencies at 50 Hz and 35 Hz. These bands are triadic responses corresponding to the sum and difference wavenumbers of the two forcing frequencies, and can be better understood by considering the power spectral density directly in frequency space, shown in figure 4.3. Firstly, as expected, the two forcing frequencies can be clearly seen as energetic vertical bands. In addition, clear narrow-band activity can be seen at 85 Hz, corresponding to the sum of the forcing frequencies with a temporal wavenumber of $\tilde{\omega}_3 = \tilde{\omega}_1 + \tilde{\omega}_2 = 0.41 \overline{U}_\infty \delta^{-1}$. This suggests that the direct non-linear coupling between the forcing modes is effective in transfer of energy to the response mode at 85 Hz. This is consistent with the observations of Yeung & Brasseur (1991) and Brasseur & Wei (1994) in HIT where *local* wavenumbers interactions were found to be mostly responsible for inter-scale energy transfer. Note that the frequencies under consideration here are of the same order,

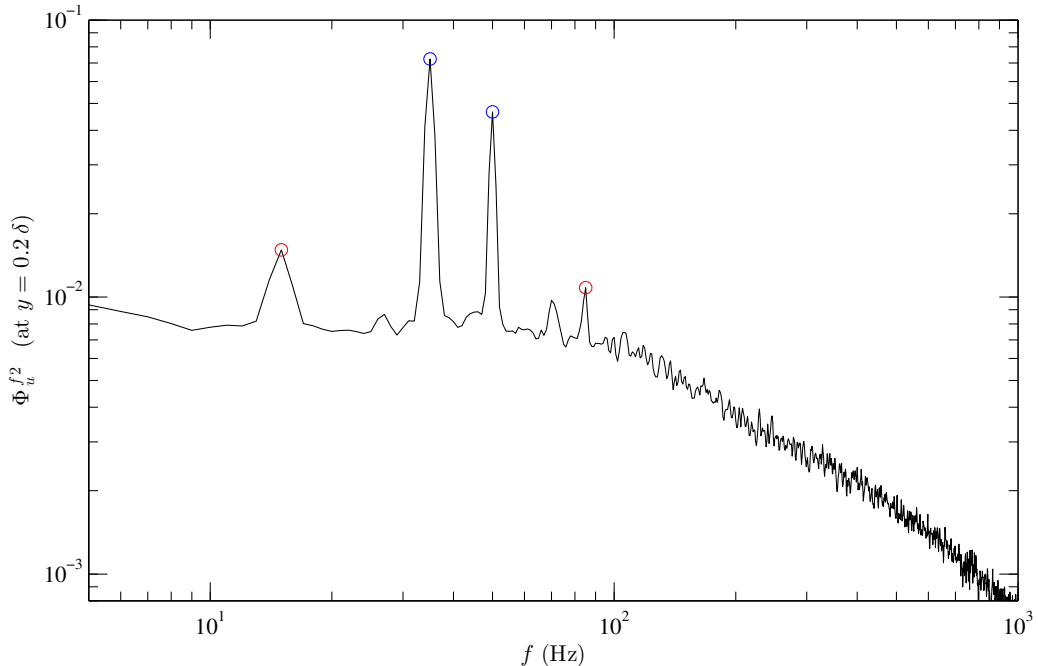


FIGURE 4.4: Raw line spectrum of $\Phi_u^{f^2}$ at $y = 0.2\delta$. The blue circles highlight forcing frequency peaks at 35 Hz and 50 Hz, and the red circles highlight triadic response frequency peaks at 15 Hz and 85 Hz.

and can thereby be classified as *local* following Brasseur & Wei (1994).

A faint energy signature centered around $y \approx 0.2\delta$ can also be seen at 15 Hz, the temporal wavenumber of $\tilde{\omega}_4 = \tilde{\omega}_1 - \tilde{\omega}_2 = 0.07\bar{U}_\infty\delta^{-1}$ corresponding to the difference frequency of the forcing modes. The relative amplitude of this lower frequency band is masked due to the pre-multiplied power level contours in figure 4.3. The raw line spectrum at this height is shown in figure 4.4 to highlight a peak in the power level at the difference frequency.

It is interesting to note that harmonics at 100 Hz and 70 Hz corresponding to the two forcing frequencies can also be identified in the above discussed spectral figures. The harmonic response represents a special case where a mode is coupled to its harmonic wavenumber through self triadic interactions. Signatures of the harmonic response can also be seen in the single-mode experiments discussed previously (see figure 3.2), and in the experimental data of Jacobi & McKeon (2011b). The harmonic modes are not subject to explicit treatment here; the focus instead will be on isolating and characterizing the triadic responses to interactions between the two distinct forcing modes. The forcing and response mode shapes are isolated from the phase-locked hotwire data in the following section, and the spatial wavelengths thus obtained show similar triadic consistency in streamwise wavenumber (k_x) space along with frequency (f) space.

4.2 Synthetic Modes Characterization

The three-component decomposition of equation 3.1 is extended in the present case to isolate the two forcing and the two triadic response modes. The total time resolved velocity U is written as

$$\begin{aligned} U(y, t) &= \bar{U}(y) + u(y, t) \\ &= \bar{U}(y) + \tilde{u}_1(y, t) + \tilde{u}_2(y, t) + \tilde{u}_3(y, t) + \tilde{u}_4(y, t) + u'(y, t). \end{aligned} \quad (4.1)$$

Here \tilde{u}_1 and \tilde{u}_2 are organized wave components corresponding to forcing mode wavenumbers $\tilde{\omega}_1$ and $\tilde{\omega}_2$, and \tilde{u}_3 and \tilde{u}_4 are organized wave components corresponding to triadic response mode wavenumbers $\tilde{\omega}_3$ and $\tilde{\omega}_4$. The *turbulent* fluctuations over the mean and four wave components are denoted by u' . Similar to equation 3.2, the wave components are written in the following general form:

$$\begin{aligned} \tilde{u}_1(x, y, z, t) &= \frac{1}{2} \hat{u}_1(y) e^{i([\tilde{k}_{x1} + i\beta_1]x + \tilde{k}_{z1}z - \tilde{\omega}_1 t)} + \text{c.c.} \\ \tilde{u}_2(x, y, z, t) &= \frac{1}{2} \hat{u}_2(y) e^{i([\tilde{k}_{x2} + i\beta_2]x + \tilde{k}_{z2}z - \tilde{\omega}_2 t)} + \text{c.c.} \\ \tilde{u}_3(x, y, z, t) &= \frac{1}{2} \hat{u}_3(y) e^{i([\tilde{k}_{x3} + i\beta_3]x + \tilde{k}_{z3}z - \tilde{\omega}_3 t)} + \text{c.c.} \\ \tilde{u}_4(x, y, z, t) &= \frac{1}{2} \hat{u}_4(y) e^{i([\tilde{k}_{x4} + i\beta_4]x + \tilde{k}_{z4}z - \tilde{\omega}_4 t)} + \text{c.c.} \end{aligned} \quad (4.2)$$

The spatial wavenumbers \tilde{k}_x , \tilde{k}_z , temporal wavenumbers $\tilde{\omega}$, and decay rates β in the above equations are all real quantities. Complex amplitudes $\hat{u}(y)$ contain magnitude and phase information of the synthetic modes with wall-normal distance.

The phase-averaging procedure outlined in section 3.2 was followed here to individually extract the above four wave components from the velocity signal $u(y, t)$. At each measurement location, the time-resolved signal $u(t)$ is first filtered through a narrow band-pass Fourier filter (10 Hz bandwidth) centered around the frequency of interest, and then phase-averaged over multiple multiple cycles; cycle counts of 1100, 2700, 3900, and 6700 were used for frequency components of 15 Hz, 35 Hz, 50 Hz, and 85 Hz respectively. It is to be noted that higher frequencies afford a greater number of oscillation cycles for a data record with fixed number of samples. The two frequency components of the encoder signal $h(t)$ (section 2.2.2) provide reference phases to coherently construct the mode shapes $\tilde{u}_1(y, t)$, $\tilde{u}_2(y, t)$ corresponding to the two forcing frequencies, and the square of the encoder signal $h^2(t)$ is used to obtain reference phases to coherently construct the mode shapes $\tilde{u}_3(y, t)$, $\tilde{u}_4(y, t)$

corresponding to the two response frequencies. Following the discussion in section 3.2.1, the two forcing modes (and the resulting response modes) excited by the spanwise-constant perturbation can be nominally treated as two dimensional. This allows us to estimate the wall-normal velocity component \tilde{v} for the modes using experimentally measured \tilde{u} and the continuity equation, written for each of the modes as

$$\begin{aligned} \frac{\partial \tilde{u}}{\partial x} + \frac{\partial \tilde{v}}{\partial y} &= 0, \\ \implies \tilde{v} &= \int_0^y \left(-\frac{\partial \tilde{u}}{\partial x} \right) dy. \end{aligned} \tag{4.3}$$

Estimates of \tilde{v} allows for the complete calculation of the non-linear forcing exerted by the two forcing modes, this aspect will be dealt with in detail later in section 4.4.

Phasemaps of \tilde{u} and \tilde{v} constructed using the above described procedures at station-1 ($x = 2.7 \delta_1$) are shown in figure 4.5 for the two forcing modes, and in figure 4.6 for the two response modes. The two forcing modes in figure 4.5 are found to be very similar in their amplitude and phase behavior. This is not entirely surprising given that the two modes were forced with equal amplitude perturbations and their frequencies are close, hence the flow response to the wall perturbation can be expected to be similar for both components. The two triadic response modes in figure 4.6 however show significantly different behavior in streamwise velocity mode shapes \tilde{u} . Starting at the wall, \tilde{u}_3 has a backward tilt in time t (forward in streamwise direction x) followed by an abrupt phase jump of π radians at $y \approx 0.4 \delta$. The direction of tilt is then found to be reversed above the phase jump location. In contrast, \tilde{u}_4 is vertically aligned for the entire height and exhibits a π radians phase jump at the edge of the boundary layer.

The contrasting behavior between the two triadic response modes can be attributed to a combination of two factors. Firstly, as will be seen in the following section, the two modes have disparate streamwise length scales. The difference response mode \tilde{u}_4 is found to be extremely long with a streamwise wavelength of $\approx 50 \delta$; confinement effects of the wind tunnel test section become significant at these length scales in determining the mode behavior. In addition to this experimental limitation, it is important to note that the non-linear forcing from the two forcing modes which drives the sum and difference wavenumber response modes is different (see section 4.4), and hence differences in the response behaviors are also to be expected.

The spatial wavelengths and wavespeeds are estimated in the following section to complete the characterization of the synthetic scales and model them as normal spatio-temporal modes.

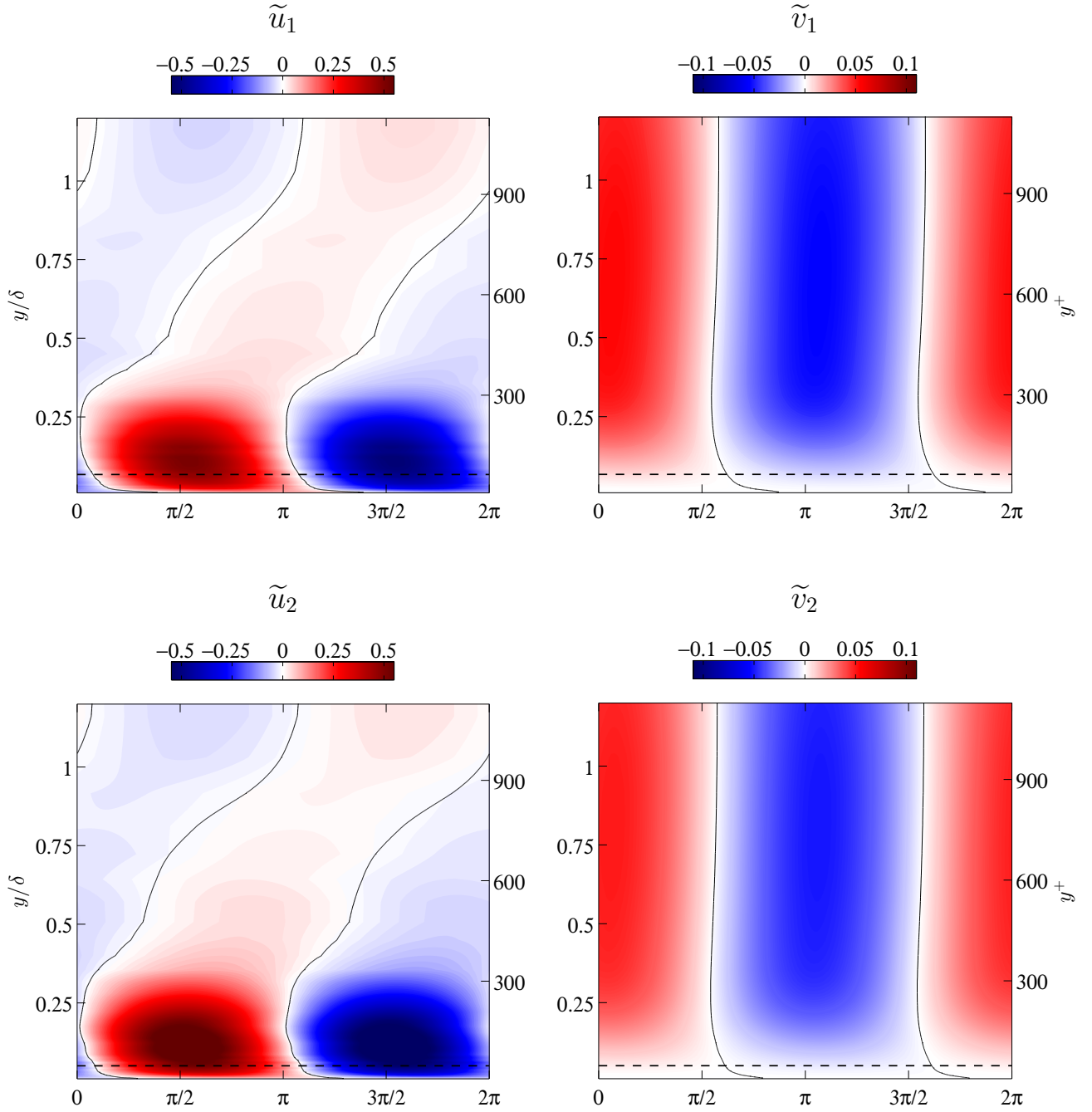


FIGURE 4.5: Phasemaps of $\tilde{u}(y, t)$ (left panel) and $\tilde{v}(y, t)$ (right panel) over one temporal period of oscillation for the two forcing modes at station-1. Top and bottom panels show data for forcing modes 1 and 2 respectively, in raw velocity units (m/s). Solid curves are contour levels at $\tilde{u}, \tilde{v} = 0$, and dashed horizontal lines indicate the critical layer locations y_c for the respective modes on all panels. It is to be noted that constant phase shifts were applied at wall-normal locations to \tilde{u}_1 and \tilde{u}_2 for better visual presentation such that the mode variation in y appears continuous. Corresponding phase shifts were also applied to \tilde{v}_1 and \tilde{v}_2 to preserve the phase relationship between \tilde{u} and \tilde{v} dictated by the continuity equation.

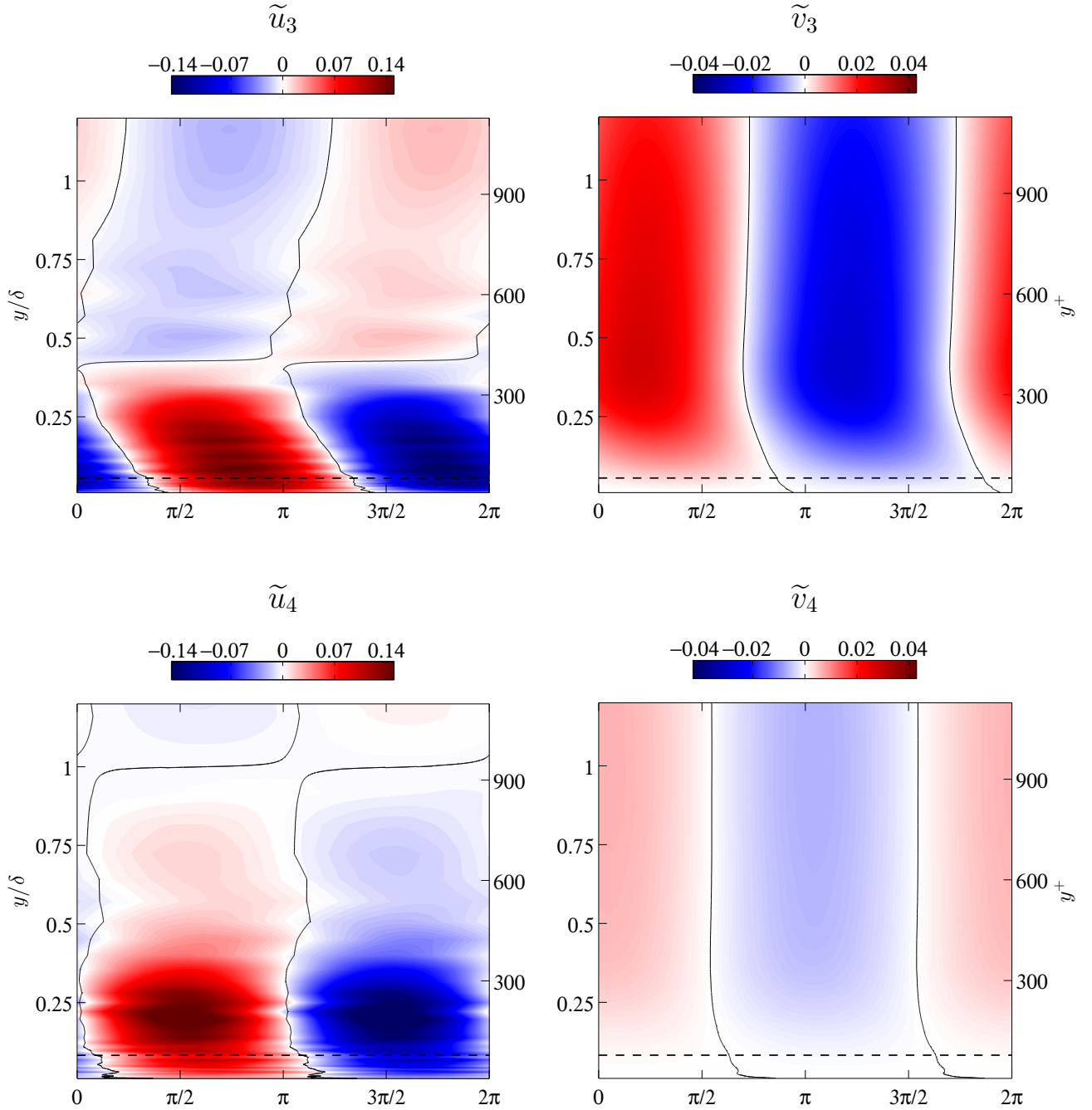


FIGURE 4.6: Phasemaps of $\tilde{u}(y, t)$ (left panel) and $\tilde{v}(y, t)$ (right panel) over one temporal period of oscillation for the two triadic response modes at station-1. Top and bottom panels show data for response modes 3 and 4 respectively, in raw velocity units (m/s). Solid curves are contour levels at $\tilde{u}, \tilde{v} = 0$, and dashed horizontal lines indicate the critical layer locations y_c for the respective modes on all panels. It is to be noted that constant phase shifts were applied at wall-normal locations to \tilde{u}_3 and \tilde{u}_4 for better visual presentation such that the mode variation in y appears continuous. Corresponding phase shifts were also applied to \tilde{v}_3 and \tilde{v}_4 to preserve the phase relationship between \tilde{u} and \tilde{v} dictated by the continuity equation.

4.2.1 Normal Mode Wavenumbers and Triadic Responses in Wavenumber Space

Mode 1 (50 Hz forcing mode)

Stations	$\tilde{\lambda}_{x1}/\delta_1$	$\beta_1 \delta_1$
1-2	14.6	0.17
2-3	15.8	0.18

Mode 2 (35 Hz forcing mode)

Stations	$\tilde{\lambda}_{x2}/\delta_1$	$\beta_2 \delta_1$
1-2	19.8	0.19
2-3	19.5	0.17

Mode 3 (85 Hz response mode)

Stations	$\tilde{\lambda}_{x3}/\delta_1$	$\beta_3 \delta_1$
1-2	8.5	0.15
2-3	9.6	0.17

Mode 4 (15 Hz response mode)

Stations	$\tilde{\lambda}_{x4}/\delta_1$	$\beta_4 \delta_1$
1-2	54.2	0.18
2-3	59.2	0.19

TABLE 4.1: Streamwise wavelengths $\tilde{\lambda}_x$ and decay rates β for the synthetic forcing modes (1 and 2) and triadic response modes (3 and 4) estimated using data between stations-1 and -2 ($\Delta x = 0.9 \delta_1$), and stations-2 and -3 ($\Delta x = 1.8 \delta_1$).

The procedure followed in section 3.2.1 is repeated here separately for each of the two forcing and two response modes to estimate their streamwise wavelengths and decay rates, and the results are shown in table 4.1. With this information, the synthetic scales can now be modeled as spatio-temporal modes, with the wavenumber triplet $\tilde{\mathbf{k}} = (\tilde{k}_x, \tilde{k}_z, \tilde{\omega})$ for each mode written as:

- Forcing modes:

$$\tilde{\mathbf{k}}_1 = (0.43 \delta^{-1}, 0, 0.24 \bar{U}_\infty \delta^{-1}); \quad \tilde{\mathbf{k}}_2 = (0.32 \delta^{-1}, 0, 0.17 \bar{U}_\infty \delta^{-1}).$$

- Response modes:

$$\tilde{\mathbf{k}}_3 = (0.74 \delta^{-1}, 0, 0.41 \bar{U}_\infty \delta^{-1}); \quad \tilde{\mathbf{k}}_4 = (0.12 \delta^{-1}, 0, 0.07 \bar{U}_\infty \delta^{-1}).$$

It is worth noting again at this point that \tilde{k}_z is nominally set to zero for the above modes since the wall perturbation is constant along the spanwise direction. However, the finite spanwise extent of the perturbation rib and the end effects caused by lateral walls of the wind tunnel test section probably induce a weak 3D nature in practice. Also, the ‘locally parallel’ approximation for the boundary layer may not hold well for the difference response mode \tilde{u}_4 given its extremely long streamwise wavelength.

With the above experimental limitations notwithstanding, it is interesting to see that triadic consistency between the forcing and response modes also holds in streamwise wavenumbers along with temporal wavenumbers. That is, $\tilde{k}_{x3} = 0.74 \delta^{-1} \approx \tilde{k}_{x1} + \tilde{k}_{x2} (= 0.75 \delta^{-1})$ and $\tilde{k}_{x4} = 0.12 \delta^{-1} \approx \tilde{k}_{x1} - \tilde{k}_{x2} (= 0.11 \delta^{-1})$; the slight differences are within the experimental uncertainty involved in estimation of the spatial wavelengths (see table 4.1). Given the quadratic non-linearity in the governing Navier-Stokes equations, the non-linear wavenumber responses resulting from two interacting modes $\tilde{\mathbf{k}}_1, \tilde{\mathbf{k}}_2$ are expected to be of the form $\tilde{\mathbf{k}}_3 = \tilde{\mathbf{k}}_1 + \tilde{\mathbf{k}}_2$ and $\tilde{\mathbf{k}}_4 = \tilde{\mathbf{k}}_1 - \tilde{\mathbf{k}}_2$. The present experimental results serve as a unique demonstration of such interactions in a fully turbulent wall-bounded flow.

4.2.2 Wavespeeds and Critical Layers

\tilde{c}_1	\tilde{c}_2	\tilde{c}_3	\tilde{c}_4
$0.56 \bar{U}_\infty$	$0.53 \bar{U}_\infty$	$0.55 \bar{U}_\infty$	$0.58 \bar{U}_\infty$
$(+0.04 \bar{U}_\infty / -0.05 \bar{U}_\infty)$	$(+0.02 \bar{U}_\infty / -0.01 \bar{U}_\infty)$	$(+0.08 \bar{U}_\infty / -0.07 \bar{U}_\infty)$	$(+0.06 \bar{U}_\infty / -0.04 \bar{U}_\infty)$

TABLE 4.2: Wavespeed estimates (and uncertainty margins) for the synthetic modes.

Wavespeeds ($\tilde{c} = \tilde{\omega}/\tilde{k}_x$) of the synthetic modes calculated from the above spatio-temporal wavenumbers are shown in table 4.2. It is observed that the two forcing modes excited by the wall perturbation propagate downstream at nearly the same rate, *i.e.* $\tilde{c}_1 \approx \tilde{c}_2$. The two spatio-temporal modes can thereby be interpreted as being part of a single physical coherent structure generated by

the perturbation, and this structure propagates downstream at a wavespeed $\approx 0.55 \bar{U}_\infty$. The two triadic response modes, by implication, also propagate downstream at nearly the same wavespeeds; this is observed in table 4.2 where $\tilde{c}_3 \approx \tilde{c}_4$. The flow therefore consists of two dominant forcing modes and two resulting triadic response modes, and this four-mode structure possesses a good degree of coherence in space and time as it propagates downstream of the perturbation. It is to be noted that the wavespeed $\tilde{c} = 0.59 \bar{U}_\infty$ of the single-mode structure in the previous experiment (section 3.2.1) also matches the above observations within measurement uncertainties. Observations from these two experiments, and also the earlier work of Jacobi & McKeon (2011*b*), suggest that the boundary layer flow is receptive to a structure with $\tilde{c} \sim 0.5 \bar{U}_\infty$ when subject to dynamic forcing from the wall. As noted earlier, a more detailed study covering a wider parameter space in terms of rib amplitude, frequency, and flow Reynolds number is required to understand the complete dynamics of the flow response to wall perturbations and verify the above hypothesis.

y_{c1}	y_{c2}	y_{c3}	y_{c4}
0.067 δ	0.050 δ	0.055 δ	0.082 δ
(+0.034 δ / - 0.025 δ)	(+0.011 δ / - 0.004 δ)	(+0.077 δ / - 0.021 δ)	(+0.062 δ / - 0.027 δ)

TABLE 4.3: Critical layer estimates (and uncertainty margins) for the synthetic modes.

Using the above wavespeed information, the estimated critical layer locations for each of the four modes are shown in table 4.3. The variation in $\tilde{\lambda}_x$ between stations 1-2 and 2-3 seen from table 4.1 were used to arrive at the uncertainty margins in tables 4.2 and 4.3. As noted previously, slight uncertainty in the estimation of \tilde{c} result in a significant change to y_c . The above critical layer locations are indicated in all relevant plots by dashed lines throughout this chapter.

4.3 Phase Relations in Scale Interactions

Having completed the characterization of the synthetic modes, we now examine the phase relations between various scales in the flow. We begin by briefly considering the bulk large- and small-scale phase relationship using the statistical measures of skewness (S) and amplitude modulation coefficient (R), discussed in detail in the previous chapter (see section 3.3). This is followed by detailed considerations of specific phase relations in interactions of isolated scales of interest.

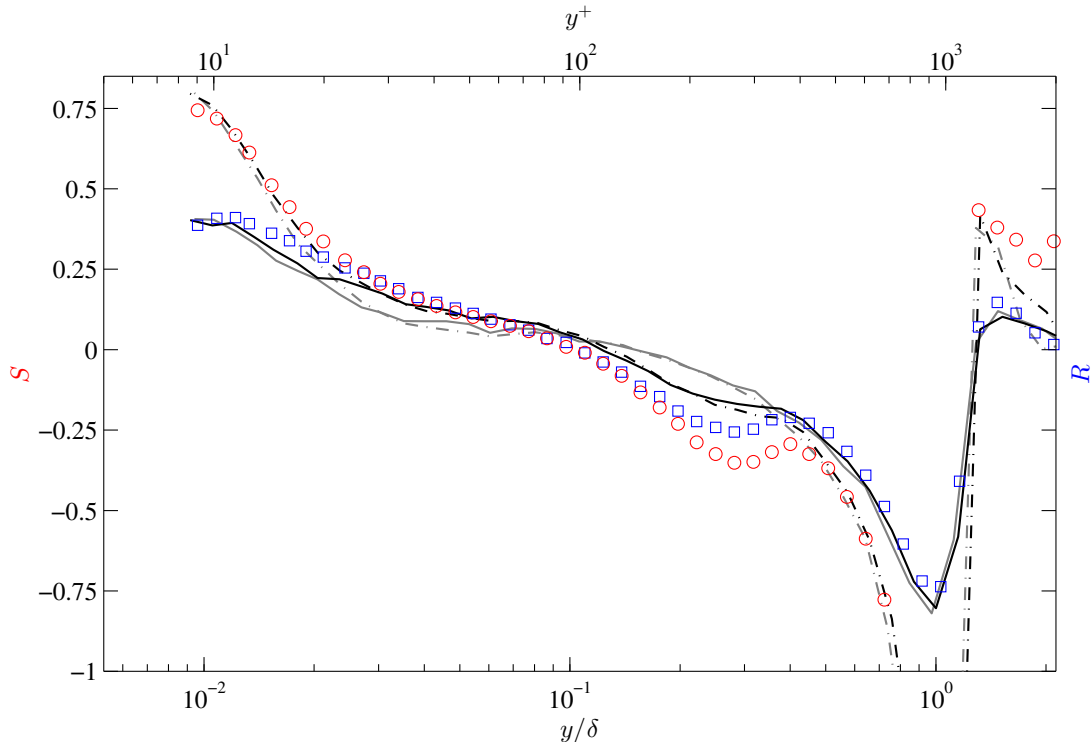


FIGURE 4.7: Skewness S (round markers) and amplitude modulation coefficient R (square markers) profiles for flow with double-mode forcing at station-1. Canonical flow skewness (dash-dot grey line) and amplitude modulation coefficient (solid grey line) data, and single-mode forced flow skewness (dash-dot black line) and amplitude modulation coefficient (solid black line) data from figure 3.6 are also shown for comparison.

4.3.1 Large- and Small-Scale Interactions

Calculation of R requires a filter cut-off selection to separate velocity fluctuations into large- and small-scales. From the power spectral data in figure 4.2, it can be seen that a clear separation between scales is harder to achieve in the present case in comparison with the previous single-mode experiment. The narrow-band corresponding to the synthetic response mode at $\tilde{\omega}_3 = 0.41 \bar{U}_\infty \delta^{-1}$ grazes the edge of the energetic small-scale near-wall region. To ensure classification of the synthetic modes as part of large-scale activity, the filter cut-off λ_γ in the present case was set at 3δ . Scale-mixing to some degree is unavoidable with the choice of $\lambda_\gamma = 3\delta$, but this has no significant bearing on the broad conclusions drawn from the following analysis. As previously demonstrated (section 3.3.4 and figure A.2), the correlation coefficient R is fairly insensitive to the choice of filter cut-off λ_γ ; more detailed investigations of the robustness of the correlation coefficient to the exact cut-off choice can be found in Mathis *et al.* (2009a), Chung & McKeon (2010), and Jacobi & McKeon (2013).

Figure 4.7 shows data for S and R from the present double-mode forcing experiment, along with previous data from canonical and single-mode forcing flows for comparison. With overall increase in the strength of synthetic large-scale activity in the present case relative to the single-mode forcing flow, a stronger ‘modulation’ effect is to be expected. This is seen in the form of relative increase in values of S , R near the wall, and relative decrease in values of S , R away from the wall in the wall-normal region where the synthetic modes are active.

4.3.2 Isolated-Scale Interactions

The following analysis is aimed at understanding interactions of a specific scale with all other scales of turbulence that are in direct triadic coupling. To begin with, we reconsider the analysis of section 3.4 where the nature of direct coupling between the single synthetic scale \tilde{u} , at wavenumber \tilde{k} , and all pairs of small-scale triadic wavenumbers k_m, k_n such that $k_n - k_m = \tilde{k}$ was investigated. The correlation coefficient Ψ between the single scale \tilde{u} and the function $\tilde{\mathcal{E}} = \tilde{u}_S^2$, which was shown to represent a physical envelope of all triadic small scales, was used to infer the phase relationship in the interaction between the two quantities. Note that the ability to isolate the organized wave component associated with the synthetic scale from the turbulent signal allows for the study of a specific set of interactions associated with that scale, *viz.* the coupling between \tilde{u} and $\tilde{\mathcal{E}}$ in that case.

A straightforward extension of this idea can be used to understand the phase relations between an isolated scale and all the associated triadic interactions at that scale. In the context of the single-mode forcing experiment, consider the function \tilde{u}^2 (denoted by $\tilde{\mathcal{R}}$), which represents the square of the velocity fluctuations u phase-averaged with respect to the input forcing signal. In comparison to $\tilde{\mathcal{E}}$, a broader class of triadic interactions over all wavenumbers k_m, k_n such that $k_n \pm k_m = \tilde{k}$ is captured by the quantity $\tilde{\mathcal{R}}$. Note that no scale restrictions are imposed on the choice of k_m, k_n in the calculation of $\tilde{\mathcal{R}}$, *i.e.* in comparison with $\tilde{\mathcal{E}}$ the small-scale filter on u is removed before the squaring and phase-averaging procedure. A correlation coefficient Φ , similar to Ψ (equation 3.13), can then be defined to quantify the phase relationship between \tilde{u} and $\tilde{\mathcal{R}}$; Φ is written as

$$\Phi = \frac{\langle \tilde{u} \tilde{\mathcal{R}} \rangle}{\langle \tilde{u}^2 \rangle^{1/2} \langle \tilde{\mathcal{R}}^2 \rangle^{1/2}} . \quad (4.4)$$

$\Phi(y)$ calculated for flow with single-mode forcing is shown in figure 4.8, along with $\Psi(y)$ (shown previously in figure 3.8) for comparison. It is seen that the profile of $\Phi(y)$ closely matches that of $\Psi(y)$ in the wall-normal region where the synthetic mode is energetically active. This suggests

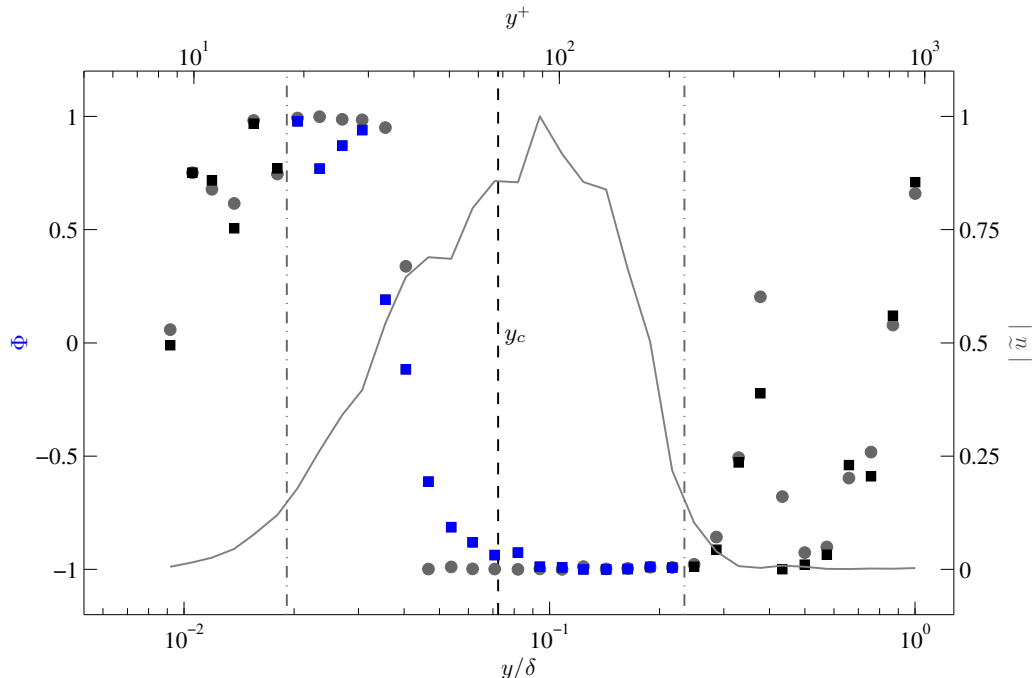


FIGURE 4.8: Correlation coefficient $\Phi(y)$ (square markers) and normalized synthetic mode energy $\langle (\tilde{u})^2 \rangle(y) / \langle (\tilde{u})^2 \rangle_{\max}$, denoted by $|\tilde{u}|$ (solid line), at station-1 for flow with single-mode forcing. The dash-dot lines indicate the wall-normal locations where the synthetic mode energy drops to 15% of its maximum value; the markers for Φ are highlighted in blue in the region between the 15%-energy reference lines. $\Psi(y)$ (round markers) from figure 3.8 are also shown in the background for comparison.

that the phase relationship between the isolated scale and the triadic wavenumber pairs is mostly dominated by interactions across the large- and small-scale filter. It is to be noted that $\tilde{\mathcal{R}}$ is related to a more traditionally studied quantity – the Reynolds stress; $\tilde{\mathcal{R}}$ represent the oscillatory normal streamwise component of the generalized fluctuating velocity stress tensor $T_{ij} = u_i u_j$. In comparison, $\tilde{\mathcal{E}}$ represents the oscillatory stress component arising from a scale-restricted velocity signal.

Correlation coefficients Ψ and Φ discussed above are presented in the following section for each of the two forcing modes and two response modes characterized earlier, along with additional phase measures specific to interactions between the synthetic modes.

4.3.3 Phase Relations at Various Levels in the Interaction Hierarchy

Data from the present double-mode forcing experiment allows us for a further extension of the above ideas to quantify specific phase relationships between the four synthetic modes. A block diagram shown in figure 4.9 summarizes the various interactions considered here and serves as a

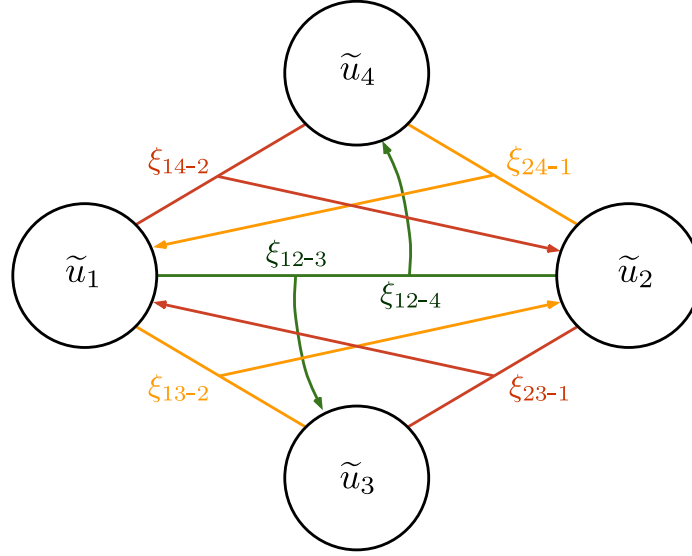


FIGURE 4.9: A block diagram summarizing the correlation coefficients formed between the four synthetic modes, each represented by a circle (or block). Arrows connecting the various blocks represent scale interactions, and they are labeled by the corresponding correlation coefficient used to quantify the interaction phase relations. All arrows are color-matched with markers in figures 4.10 and 4.11 that show the corresponding correlation coefficient data.

helpful reference. We first consider the two response modes \tilde{u}_3 and \tilde{u}_4 , which are primarily forced by the synthetic modes \tilde{u}_1 and \tilde{u}_2 . Akin to the function $\tilde{\mathcal{R}}$ defined above, we define the following two quantities: $\tilde{\mathcal{R}}_{12-3} = \widetilde{\tilde{u}_1 \tilde{u}_2}$, which represents the product of \tilde{u}_1, \tilde{u}_2 phase-averaged with respect to the reference signal for \tilde{u}_3 ; $\tilde{\mathcal{R}}_{12-4} = \widetilde{\tilde{u}_1 \tilde{u}_2}$, which represents the product of \tilde{u}_1, \tilde{u}_2 phase-averaged with respect to the reference signal for \tilde{u}_4 . It is to be noted that the product $\tilde{u}_1 \tilde{u}_2$ consists of two scales corresponding to the sum and difference wavenumbers ($\tilde{k}_3 = \tilde{k}_1 + \tilde{k}_2$) and ($\tilde{k}_4 = \tilde{k}_1 - \tilde{k}_2$) respectively; $\tilde{\mathcal{R}}_{12-3}$ picks out the scale at wavenumber \tilde{k}_3 and $\tilde{\mathcal{R}}_{12-4}$ picks out the scale at wavenumber \tilde{k}_4 .

The phase relationships between \tilde{u}_3 and $\tilde{\mathcal{R}}_{12-3}$, and \tilde{u}_4 and $\tilde{\mathcal{R}}_{12-4}$ can then be quantified by defining the following two correlation coefficients:

$$\begin{aligned} \xi_{12-3} &= \frac{\langle \tilde{u}_3 \tilde{\mathcal{R}}_{12-3} \rangle}{\langle \tilde{u}_3^2 \rangle^{1/2} \langle \tilde{\mathcal{R}}_{12-3}^2 \rangle^{1/2}} ; \\ \xi_{12-4} &= \frac{\langle \tilde{u}_4 \tilde{\mathcal{R}}_{12-4} \rangle}{\langle \tilde{u}_4^2 \rangle^{1/2} \langle \tilde{\mathcal{R}}_{12-4}^2 \rangle^{1/2}} . \end{aligned} \tag{4.5}$$

In comparison with Φ (equation 4.4), which is measure of the phase between a single scale and all the triadically consistent wavenumber pairs, ξ_{12-3} and ξ_{12-4} provide a measure of the phase between

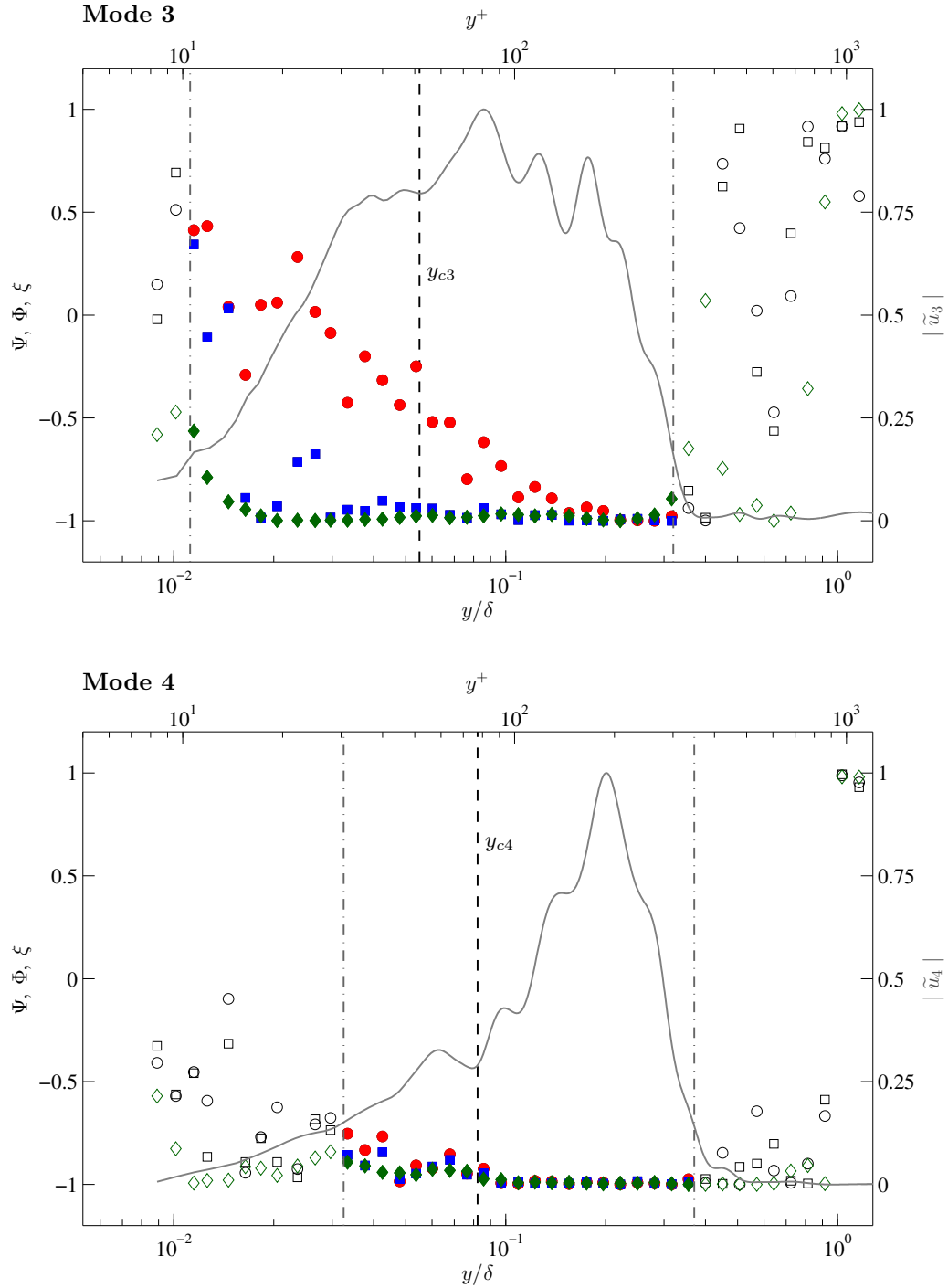


FIGURE 4.10: Correlation coefficients Φ_3 (square markers), Ψ_3 (round markers), and ξ_{12-3} (diamond markers) for mode \tilde{u}_3 in the top plot, and correlation coefficients Φ_4 (square markers), Ψ_4 (round markers), and ξ_{12-4} (diamond markers) for mode \tilde{u}_4 in the bottom plot are shown at station-1. The corresponding normalized mode energies are shown in the background (grey curves) in both plots, and the wall-normal locations where the mode energy drops to 15% of its maximum value are indicated by dash-dot lines for reference. Data markers in this region where the synthetic mode is energetically active are highlighted in color.

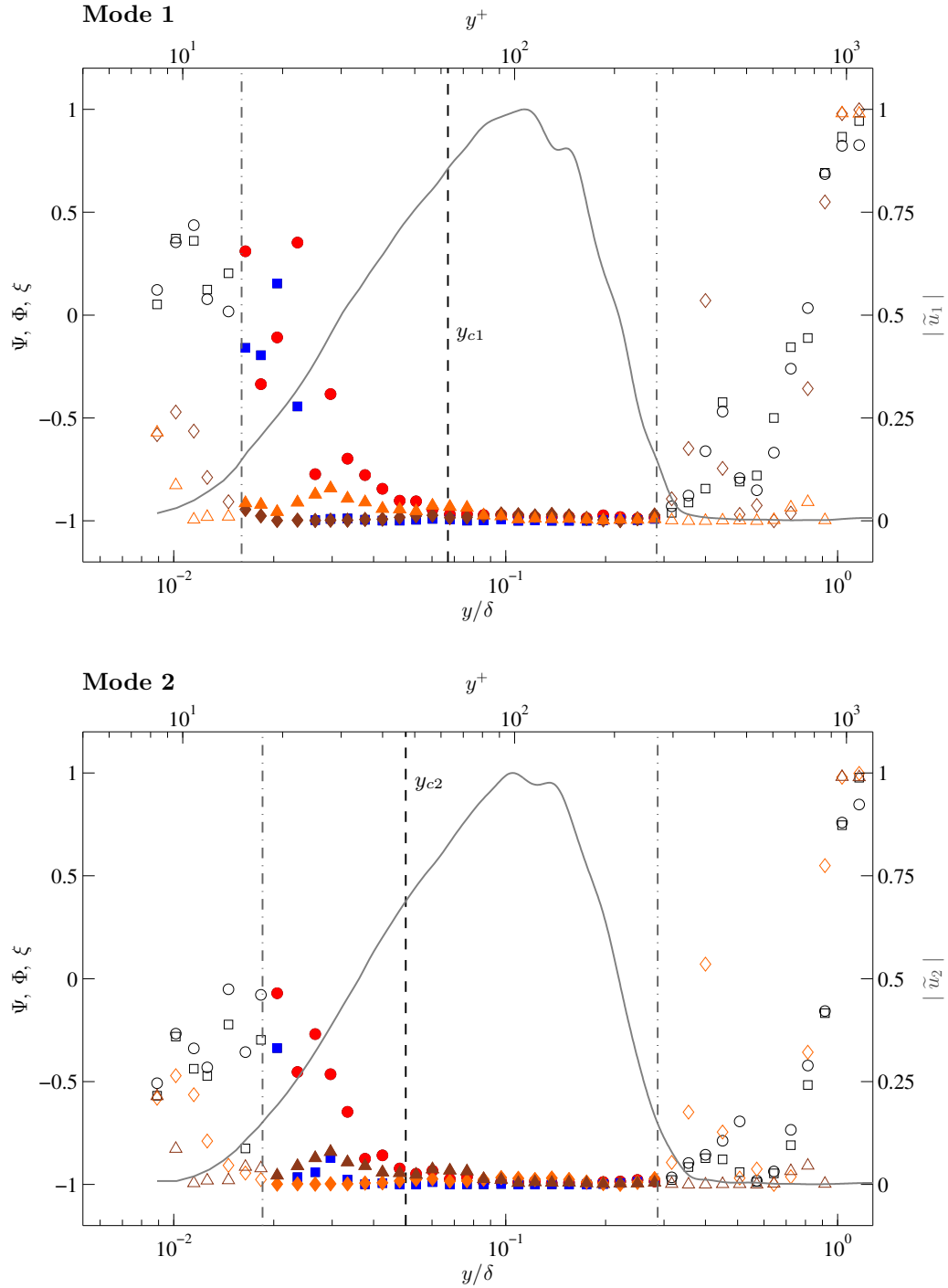


FIGURE 4.11: Correlation coefficients Φ_1 (square markers), Ψ_1 (round markers), ξ_{23-1} (diamond markers), and ξ_{24-1} (triangle markers) for mode \tilde{u}_1 in the top plot, and correlation coefficients Φ_2 (square markers), Ψ_2 (round markers), ξ_{13-2} (diamond markers), and ξ_{14-2} (triangle markers) for mode \tilde{u}_2 in the bottom plot are shown at station-1. The corresponding normalized mode energies are shown in the background (grey curves) in both plots, and the wall-normal locations where the mode energy drops to 15% of its maximum value are indicated by dash-dot lines for reference. Data markers in this region where the synthetic mode is energetically active are highlighted in color.

the response modes and just the two forcing modes. From the general form of the synthetic mode velocities in equation 4.2, the above correlation coefficients can easily be reduced to the form

$$\begin{aligned}\xi_{12-3} &= \cos(\angle\hat{u}_1 + \angle\hat{u}_2 - \angle\hat{u}_3), \\ \xi_{12-4} &= \cos(\angle\hat{u}_1 - \angle\hat{u}_2 - \angle\hat{u}_4),\end{aligned}\tag{4.6}$$

where $\angle\hat{u}$ denotes the phase of the complex mode amplitude \hat{u} . Figure 4.10 shows the correlation coefficients ξ_{12-3} , Ψ_3 , Φ_3 for mode 3, and ξ_{12-4} , Ψ_4 , Φ_4 for mode 4. It is to be noted the procedures described earlier to calculate Ψ , Φ for the single-mode forcing experiment is implemented here for modes 3 and 4 separately to obtain Ψ_3 , Φ_3 , and Ψ_4 , Φ_4 respectively.

Similar correlation coefficients are also written for each of the two forcing modes as

$$\xi_{23-1} = \frac{\langle \tilde{u}_1 \tilde{\mathcal{R}}_{23-1} \rangle}{\langle \tilde{u}_1^2 \rangle^{1/2} \langle \tilde{\mathcal{R}}_{23-1}^2 \rangle^{1/2}}, \quad \xi_{24-1} = \frac{\langle \tilde{u}_1 \tilde{\mathcal{R}}_{24-1} \rangle}{\langle \tilde{u}_1^2 \rangle^{1/2} \langle \tilde{\mathcal{R}}_{24-1}^2 \rangle^{1/2}}, \tag{4.7}$$

$$\xi_{13-2} = \frac{\langle \tilde{u}_2 \tilde{\mathcal{R}}_{13-2} \rangle}{\langle \tilde{u}_2^2 \rangle^{1/2} \langle \tilde{\mathcal{R}}_{13-2}^2 \rangle^{1/2}}, \quad \xi_{14-2} = \frac{\langle \tilde{u}_2 \tilde{\mathcal{R}}_{14-2} \rangle}{\langle \tilde{u}_2^2 \rangle^{1/2} \langle \tilde{\mathcal{R}}_{14-2}^2 \rangle^{1/2}}. \tag{4.8}$$

Here ξ_{23-1} and ξ_{24-1} quantify the phase interactions of scale \tilde{u}_1 with triadic combinations of $\tilde{u}_2\tilde{u}_3$ and $\tilde{u}_2\tilde{u}_4$ respectively. Similarly, ξ_{13-2} and ξ_{14-2} quantify the phase interactions of scale \tilde{u}_2 with triadic combinations of $\tilde{u}_1\tilde{u}_3$ and $\tilde{u}_1\tilde{u}_4$ respectively. In terms of the complex mode amplitude phase, the above coefficients can be reduced to the form

$$\begin{aligned}\xi_{23-1} &= \cos(\angle\hat{u}_3 - \angle\hat{u}_2 - \angle\hat{u}_1), & \xi_{24-1} &= \cos(\angle\hat{u}_2 + \angle\hat{u}_4 - \angle\hat{u}_1), \\ \xi_{13-2} &= \cos(\angle\hat{u}_3 - \angle\hat{u}_1 - \angle\hat{u}_2), & \xi_{14-2} &= \cos(\angle\hat{u}_1 - \angle\hat{u}_4 - \angle\hat{u}_2).\end{aligned}\tag{4.9}$$

Straightforward comparisons of equations 4.6 and 4.9 lead to the following simple relationships between the various phase measures

$$\begin{aligned}\xi_{12-3} &= \xi_{23-1} = \xi_{13-2}, \\ \xi_{12-4} &= \xi_{24-1} = \xi_{14-2}.\end{aligned}\tag{4.10}$$

For a given set of three triadically consistent modes, $\{\tilde{u}_1, \tilde{u}_2, \tilde{u}_3\}$ or $\{\tilde{u}_1, \tilde{u}_2, \tilde{u}_4\}$, the (unsigned) phase difference between the oscillatory Reynolds stress arising from any two of the three modes in

the triad and the velocity response (the third mode) is the same. Figure 4.11 shows the correlation coefficients Ψ_1, Φ_1 for mode 1, and Ψ_2, Φ_2 for mode 2. As noted above, the procedure to calculate Ψ, Φ is implemented for modes 1 and 2 separately to obtain Ψ_1, Φ_1 , and Ψ_2, Φ_2 respectively. Data for ξ_{12-3} and ξ_{12-4} (from figure 4.10) are shown again in both plots (labeled as ξ_{23-1}, ξ_{24-1} in the top plot, and ξ_{13-2}, ξ_{14-2} in the bottom plot) for completeness.

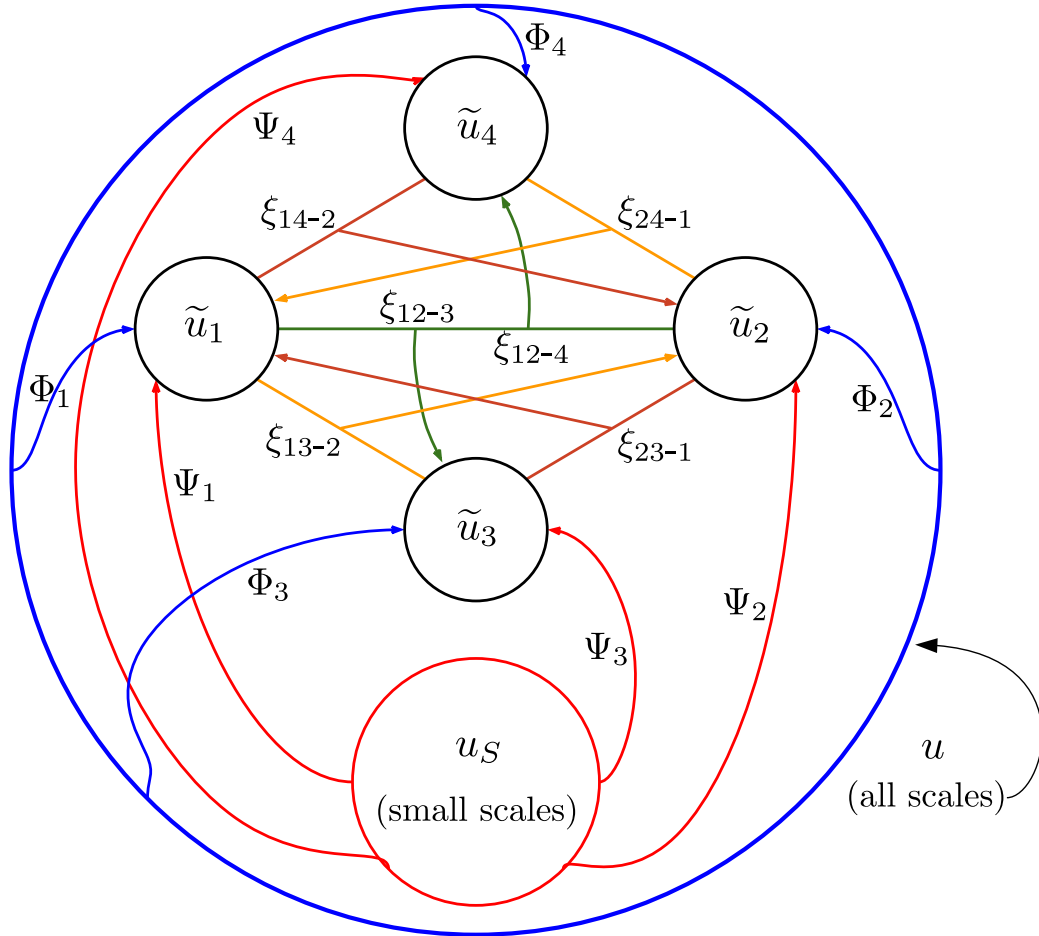


FIGURE 4.12: A block diagram summarizing the correlation coefficients formed at various levels in the scale interaction hierarchy. The outer blue circle, or block, represents the entire system containing all the scales of turbulent fluctuations, and the inner red block is a subset that represents the small scales. The four isolated scales (synthetic modes), shown earlier in figure 4.9, are also a subset of entire the system. Arrows connecting the various blocks represent scale interactions, and they are labeled by the corresponding correlation coefficient used to quantify the interaction phase relations. All arrows are color-matched with markers in figures 4.10 and 4.11 that show the corresponding correlation coefficient data.

The block diagram in figure 4.12 summarizes all the correlation coefficients used in this section to quantify the phase relations involved in the interactions of isolated scales. These interactions can be classified into a three-level nested hierarchy. At the outer level are the interactions of an isolated scale with all the other scales (Φ). At the intermediate level are the interactions with the small scales (Ψ). And finally, at the inner level are basic first-order interactions involving the isolated scale and two other triadically consistent scales (ξ).

It is observed from data in figure 4.10 that the overall phase in the interactions of the two response modes are dominated by the influence of the two forcing modes. An interesting contrast in the phase of small-scale interactions between modes 3 and 4 is also noted, and the same is broadly attributed to the differences in behavior of the two response modes discussed earlier. It is also interesting to note that all the correlation coefficients ξ_{12-3} , ξ_{12-4} shown in figure 4.10 (and figure 4.11) have a value of -1, or close to -1, in the wall-normal regions of interest. This implies that the ‘Reynolds stress’ from any two interacting scales on the third scale in a triad has a phase shift of π radians. While this is noted here at an observational level, further analysis is needed to understand the full significance of such consistent phase behavior between the four interacting scales.

4.4 Rank-1 Resolvent Operator Model

As a final exercise, we now examine the role of low-rank dynamics in the interactions of the four synthetic modes. The rank-1 resolvent operator model of McKeon & Sharma (2010), briefly introduced earlier in section 1.4.2, will be considered here for a forcing-response type analysis. In this model, the governing Navier-Stokes equations for a wall-bounded turbulent flow are Fourier transformed along the homogeneous directions of x, z, t with corresponding wavenumbers k_x, k_z, ω . This transformation reduces the governing equations for the three-dimensional velocity field $\mathbf{u}(x, y, z, t)$ to the following form at each scale $\mathbf{k} = (k_x, k_z, \omega)$:

$$\hat{\mathbf{u}}_{\mathbf{k}} = \mathcal{H}_{\mathbf{k}} \hat{\mathbf{f}}_{\mathbf{k}}. \quad (4.11)$$

Here $\hat{\mathbf{u}}$ is the velocity, \mathcal{H} is the linear Navier-Stokes resolvent operator, and $\hat{\mathbf{f}}$ is the net contribution at scale \mathbf{k} from the non-linear term $-(\mathbf{u} \cdot \nabla)\mathbf{u}$ in the original equations. For a given \mathbf{k} , the term $\hat{\mathbf{f}}_{\mathbf{k}}$ arises from non-linear interactions of all other pairs of triadically consistent scales $\mathbf{k}_a, \mathbf{k}_b$ such that $\mathbf{k}_a \pm \mathbf{k}_b = \mathbf{k}$. Thereby $\hat{\mathbf{f}}$ can be considered as a form of *endogenous* forcing that drives the dynamics associated with the linear operator \mathcal{H} (McKeon *et al.*, 2013). It is to be noted that the

terms $\widehat{\mathbf{u}}$, \mathcal{H} , $\widehat{\mathbf{f}}$ are functions of the non-homogeneous direction y . Detailed formulation of \mathcal{H} can be found in [McKeon & Sharma \(2010\)](#); [Luhar *et al.* \(2014\)](#) for a turbulent pipe, and in [Moarref *et al.* \(2013\)](#) for a turbulent channel.

Schmidt decomposition (or singular value decomposition) was used by [McKeon & Sharma \(2010\)](#) to seek a structure for the dominant forcing-response behavior dictated by the operator \mathcal{H} . The decomposition results in an orthogonal set of forcing and response functions (denoted by ϕ_j and ψ_j respectively), referred to as singular modes, and associated singular values (denoted by σ_j). The velocity response $\widehat{\mathbf{u}}$ is then represented using the first N singular modes as

$$\widehat{\mathbf{u}}_{\mathbf{k}} = \sum_{j=1}^N \chi_{\mathbf{k}j} \sigma_{\mathbf{k}j} \psi_{\mathbf{k}j}, \quad (4.12)$$

where $\psi_{\mathbf{k}j}$ and $\sigma_{\mathbf{k}j}$ are the singular response modes and singular values respectively of $\mathcal{H}_{\mathbf{k}}$, and the weights $\chi_{\mathbf{k}j}$ represent the projections of $\widehat{\mathbf{f}}_{\mathbf{k}}$ onto the singular forcing modes. $\widehat{\mathbf{f}}_{\mathbf{k}}$ is written as

$$\widehat{\mathbf{f}}_{\mathbf{k}} = \sum_{j=1}^N \chi_{\mathbf{k}j} \phi_{\mathbf{k}j}, \quad \text{where} \quad \chi_{\mathbf{k}j} = \int \phi_{\mathbf{k}j}^* \widehat{\mathbf{f}}_{\mathbf{k}} dy. \quad (4.13)$$

[McKeon & Sharma \(2010\)](#) demonstrated the operator \mathcal{H} is low-rank for a wide range of active spatio-temporal scales \mathbf{k} found in wall turbulence. The first singular value $\sigma_{\mathbf{k}1}$ was found to be significantly higher than the rest, that is $\sigma_{\mathbf{k}1} \gg \sigma_{\mathbf{k}j}$ for $j \geq 2$, for scales \mathbf{k} of interest. A rank-1 model, where the velocity response is approximated as $\widehat{\mathbf{u}}_{\mathbf{k}} \approx \sigma_{\mathbf{k}1} \psi_{\mathbf{k}1}$, was found to capture the key statistical ([Moarref *et al.*, 2013](#)) and structural ([Sharma & McKeon, 2013](#); [Luhar *et al.*, 2014](#)) features of wall turbulence.

The above resolvent model is used to understand the role of low-rank dynamics in the experimentally observed triadic responses that result from the interaction between the two forcing modes. Rank-1 forcing modes $\phi_1 = (\phi_x, \phi_y, \phi_z)$ and response modes $\psi_1 = (\psi_x, \psi_y, \psi_z)$ for the experimental wavenumbers $\widetilde{\mathbf{k}}_3$ and $\widetilde{\mathbf{k}}_4$, along with the corresponding singular values σ_1 , were obtained from the readily available turbulent channel resolvent computational code of [Moarref *et al.* \(2013\)](#), and are shown in figures 4.13 and 4.14. The experimentally obtained u and v velocity components for the two forcing modes (data shown in figure 4.5) are used to estimate the forcing $\widehat{\mathbf{f}}_{\mathbf{k}_3}$ and $\widehat{\mathbf{f}}_{\mathbf{k}_4}$ (at wavenumbers $\widetilde{\mathbf{k}}_3$ and $\widetilde{\mathbf{k}}_4$ respectively) that arises from the interaction of modes 1 and 2 (wavenumbers $\widetilde{\mathbf{k}}_1$ and $\widetilde{\mathbf{k}}_2$); details of this calculation are provided in appendix B.1. Amplitude and phase of the resulting estimates for $\widehat{\mathbf{f}}_{\mathbf{k}_3} = (f_x, f_y, 0)_{\mathbf{k}_3}$ and $\widehat{\mathbf{f}}_{\mathbf{k}_4} = (f_x, f_y, 0)_{\mathbf{k}_4}$, along with the experimental velocity responses $\widetilde{\mathbf{u}}_3 = (\widetilde{u}_3, \widetilde{v}_3, 0)$ and $\widetilde{\mathbf{u}}_4 = (\widetilde{u}_4, \widetilde{v}_4, 0)$ (from figure 4.6), are also shown in the

figures with the resolvent data. It is to be noted that the resolvent modes obtained from the operator \mathcal{H} are normalized to contain unit energy. Therefore the experimental and resolvent data magnitudes in figures are normalized by their respective maxima to enable a direct comparison of variation with wall-normal distance.

The experimental forcing estimates $\widehat{\mathbf{f}}_{\mathbf{k}_3}$ and $\widehat{\mathbf{f}}_{\mathbf{k}_4}$ are projected on to the respective resolvent forcing modes $\phi_{\mathbf{k}_3,1}$ and $\phi_{\mathbf{k}_4,1}$ to obtain the weights $\chi_{\mathbf{k}_3,1}$ and $\chi_{\mathbf{k}_4,1}$:

$$\chi_{\mathbf{k}_3,1} = \int_0^\delta \phi_{\mathbf{k}_3,1}^* \widehat{\mathbf{f}}_{\mathbf{k}_3} dy; \quad \chi_{\mathbf{k}_4,1} = \int_0^\delta \phi_{\mathbf{k}_4,1}^* \widehat{\mathbf{f}}_{\mathbf{k}_4} dy. \quad (4.14)$$

The experimental velocity response $\widetilde{\mathbf{u}}_3$ and $\widetilde{\mathbf{u}}_4$ are also projected on to the respective resolvent response modes $\psi_{\mathbf{k}_3,1}$ and $\psi_{\mathbf{k}_4,1}$ to obtain weights, denoted by $\alpha_{\mathbf{k}_3,1}$ and $\alpha_{\mathbf{k}_4,1}$, which serve as indicators for the strength of rank-1 behavior in the actual measured response. $\alpha_{\mathbf{k}_3,1}$ and $\alpha_{\mathbf{k}_4,1}$ are written as

$$\alpha_{\mathbf{k}_3,1} = \int_0^\delta \psi_{\mathbf{k}_3,1}^* \widehat{\mathbf{u}}_3 dy; \quad \alpha_{\mathbf{k}_4,1} = \int_0^\delta \psi_{\mathbf{k}_4,1}^* \widehat{\mathbf{u}}_4 dy. \quad (4.15)$$

From equations 4.12 and 4.13, we expect the above forcing and response weights to be related through their respective singular values

$$\alpha_{\mathbf{k}_3,1} = \sigma_{\mathbf{k}_3,1} \chi_{\mathbf{k}_3,1} \quad \text{and} \quad \alpha_{\mathbf{k}_4,1} = \sigma_{\mathbf{k}_4,1} \chi_{\mathbf{k}_4,1}. \quad (4.16)$$

Using the data presented in figures 4.13 and 4.14, the amplitude and phase values of the LHS and RHS terms in the above equations are found to be

- $|\alpha_{\mathbf{k}_3,1}| = 33.4$, $\angle\alpha_{\mathbf{k}_3,1} = 20.5^\circ$ and $|\sigma_{\mathbf{k}_3,1} \chi_{\mathbf{k}_3,1}| = 15.3$, $\angle(\sigma_{\mathbf{k}_3,1} \chi_{\mathbf{k}_3,1}) = 11.5^\circ$,
- $|\alpha_{\mathbf{k}_4,1}| = 27.4$, $\angle\alpha_{\mathbf{k}_4,1} = -131.3^\circ$ and $|\sigma_{\mathbf{k}_4,1} \chi_{\mathbf{k}_4,1}| = 43.5$, $\angle(\sigma_{\mathbf{k}_4,1} \chi_{\mathbf{k}_4,1}) = -128.2^\circ$.

While the amplitudes compare poorly, a reasonably good agreement is seen among phase values in the above results.

It is worth noting the limitations of this analysis at this point. Firstly, the use of channel resolvent modes for analysis of boundary layer data introduces inaccuracies, particularly in the outer region. In addition, the forcing estimates are prone to experimental noise, as evidenced by the spurious small-scale fluctuations in the amplitude and phase profiles of figures 4.13 and 4.14. This in turn introduces projection errors in equations 4.14 and 4.15 used to estimate weights. Apart from these practical limitations, it is also important to note that the forcing in the experiments is externally imposed, and changing the relative phase between the two forcing modes can alter the

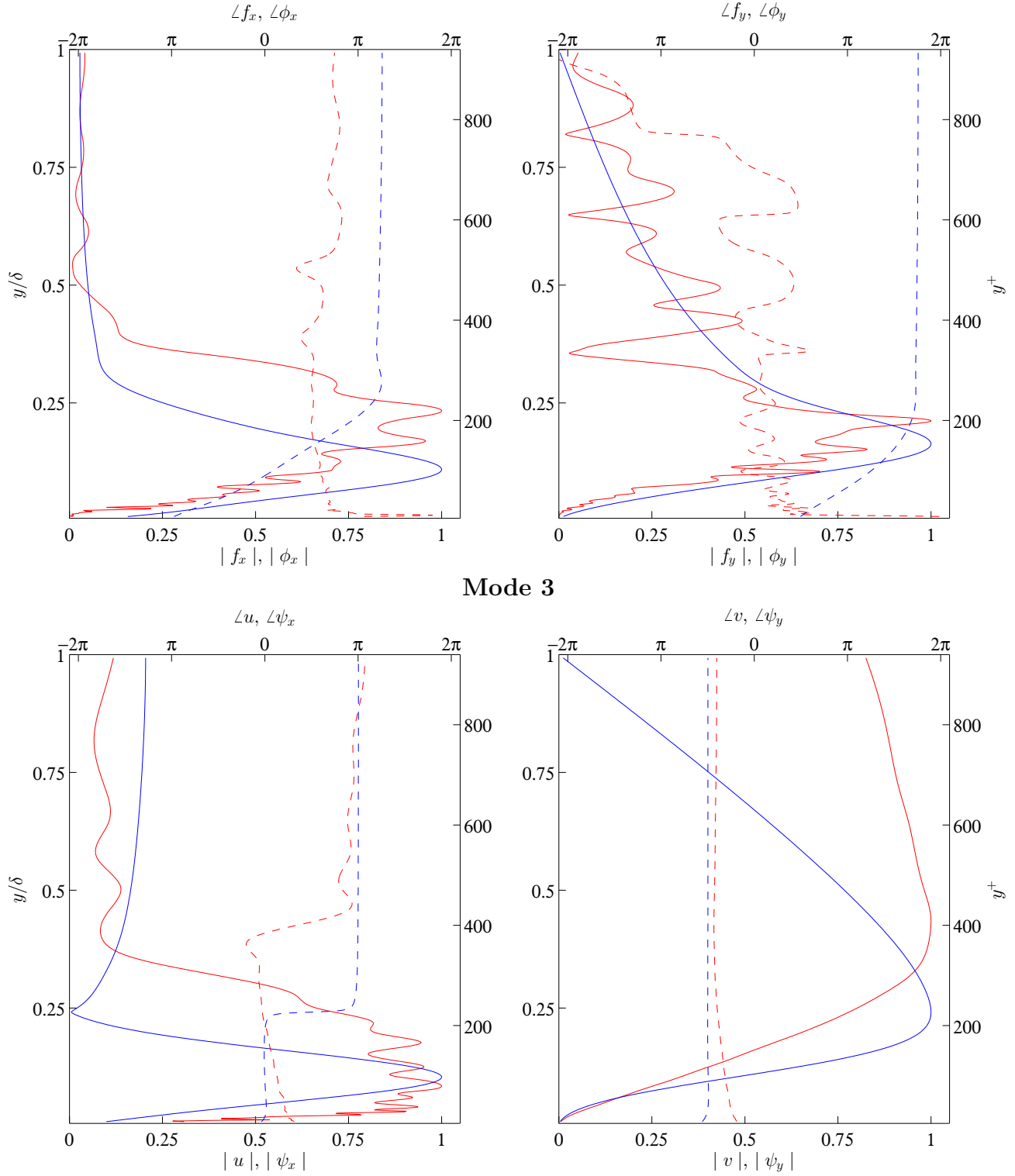


FIGURE 4.13: Comparison of the experimental forcing and response data (red) with rank-1 resolvent data (blue) for mode 3. Normalized magnitude (solid lines) and phase (dashed lines) variation with wall-normal distances is shown for x and y components of forcing (top panels) and velocity response (bottom panels). All the mode amplitudes shown here are in normalized forms.

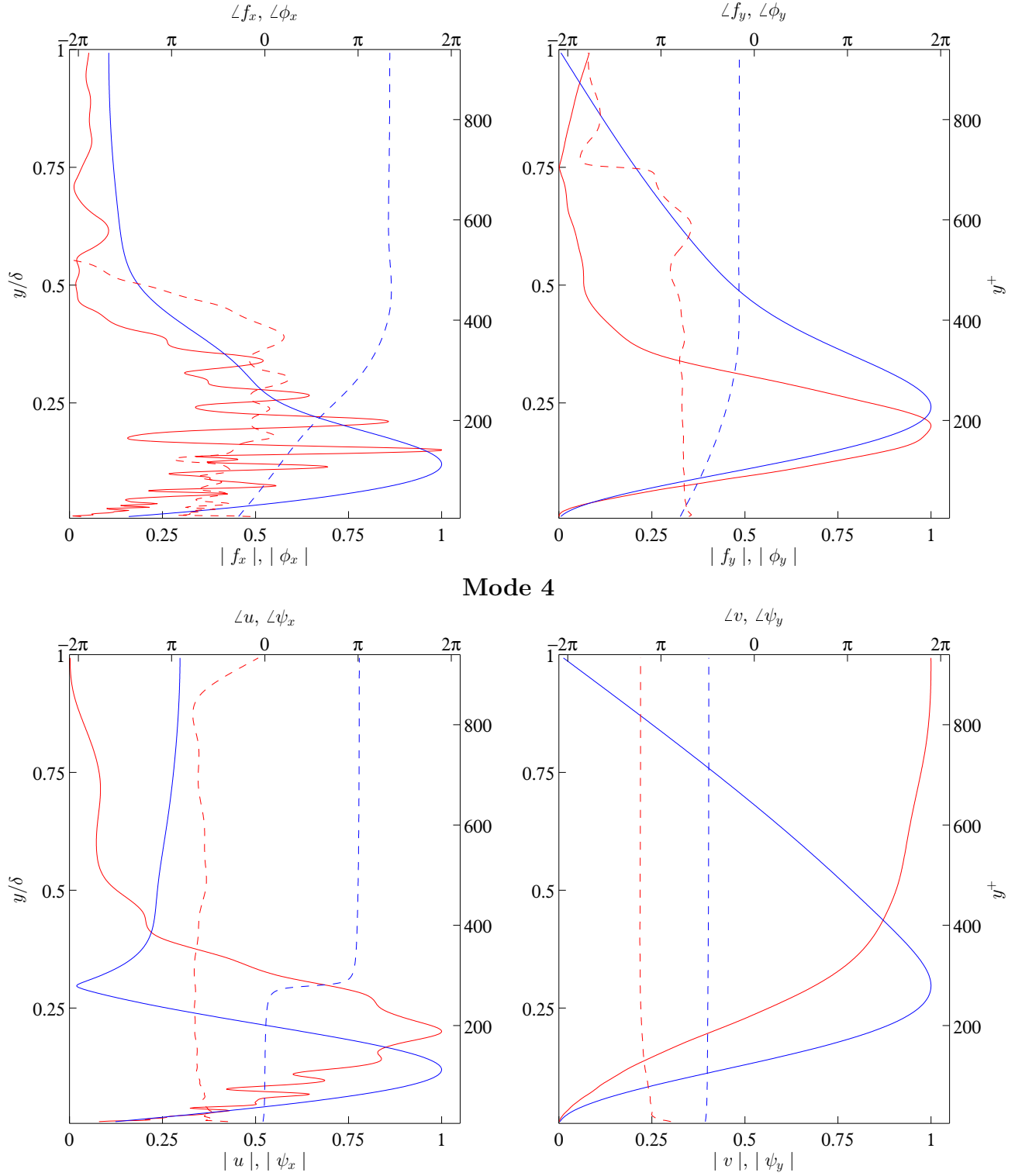


FIGURE 4.14: Comparison of the experimental forcing and response data (red) with rank-1 resolvent data (blue) for mode 4. Normalized magnitude (solid lines) and phase (dashed lines) variation with wall-normal distances is shown for x and y components of forcing (top panels) and velocity response (bottom panel). All the mode amplitudes shown here are in normalized forms.

structure of the forcing vector $\hat{\mathbf{f}}$. If the structure of the imposed forcing is such that a significant portion of its energy lies orthogonal to the rank-1 mode, then a higher rank model is essential to capture the entire forcing-response dynamics. The above exercise nonetheless serves as a useful ‘first-order’ analysis of the problem.

Chapter 5

Concluding Remarks

The present work demonstrates the effectiveness of a forcing-response type approach towards understanding the dynamical structure of wall turbulence. Deterministic external inputs to the flow provide the ability to highlight specific scales, and then carefully study the nature of their non-linear coupling with other scales of turbulence. Recent advances in the study of large- and small-scale interactions, and the increasingly clear significance of large-scale activity in the overall flow dynamics served as motivation for application of forcing at the large scales.

The large- and small-scale correlation coefficient, popularly termed amplitude modulation coefficient, was formulated as a measure of phase among sets of scales in triadic coupling. A direct relationship was also established with the skewness statistic of fluctuations, thereby providing a simple explanation for the somewhat puzzling similarity noted between the two quantities in recent literature. The natural large- and small-scale phase relations in the flow were then experimentally altered in a deterministic manner by introducing a synthetic large-scale mode in the flow. A clear manifestation of the synthetic mode effect was seen on small-scale wavenumber pairs in direct triadic coupling. These experimental observations strongly suggest that a critical layer mechanism is at play in determining the relative placement of scales in the flow; modeling this phenomena directly from the governing equations is a subject of ongoing work (McKeon, Chung, Duvvuri & Jacobi). In continuation of the single synthetic mode experiments, simultaneous forcing of two large-scale modes in the flow offered a clear, and unique, demonstration of triadic response to direct non-linear interactions. The study of phase relations was extended to consider specific relationships between the synthetic forcing and response modes. A constant phase-offset behavior was noted between combinations of any two synthetic modes and the third mode of triadic consistency. A preliminary study of direct triadic interactions between the synthetic modes using a rank-1 model of the Navier-Stokes resolvent operator offered encouraging results.

Though the natural structure of wall turbulence is predominantly three-dimensional (3D) in space, spanwise-constant perturbations were chosen in the present work for ease in experimentation. The next step would be to investigate the behavior of 3D synthetic modes in the flow. In addition, the wall perturbation was used simply as a tool to excite large-scale modes in the flow, and the dynamics associated with the perturbation itself were not explicitly investigated in the present work. It would be worthwhile to perform a detailed study aimed at understanding the mechanism that sets the dominant streamwise length scale in flow downstream of the perturbation. With regard to the study of direct non-linear interactions between two synthetic modes, changing the structure of forcing that results from such interactions by altering the relative phase between the two forcing modes could possibly lead to interesting results, and provide further insight into the forcing-response dynamics of the system.

The long-term scientific goal of this line of investigation is to complement modeling efforts, and build a *closed* picture of the network of interacting scales in wall turbulence. At that point, the open question from an engineer's perspective would be the following: is it possible to design and implement *smart* external inputs to robustly alter the state of turbulence in desirable ways?

Bibliography

- ADRIAN, R. J. 2007 Hairpin vortex organization in wall turbulence. *Physics of Fluids* **19** (4), 041301.
- BANDYOPADHYAY, P. R. & HUSSAIN, A. K. M. F. 1984 The coupling between scales in shear flows. *Physics of Fluids* **27** (9), 2221–2228.
- BERKOOZ, G., HOLMES, P. & LUMLEY, J. L. 1993 The Proper Orthogonal Decomposition in the analysis of turbulent flows. *Annual Review of Fluid Mechanics* **25**, 539–575.
- BERNARDINI, M. & PIROZZOLI, S. 2011 Inner/outer layer interactions in turbulent boundary layers: A refined measure for the large-scale amplitude modulation mechanism. *Physics of Fluids* **23** (6), 061701.
- BRASSEUR, J. G. & WEI, C-H. 1994 Interscale dynamics and local isotropy in high Reynolds number turbulence within triadic interactions. *Physics of Fluids* **6** (2), 842–870.
- BROWN, G. L. & THOMAS, A. S. W. 1977 Large structure in a turbulent boundary layer. *Physics of Fluids* **20** (10), S243–S252.
- CANTWELL, B. J. 1981 Organized motion in turbulent flow. *Annual Review of Fluid Mechanics* **13**, 457–515.
- CHEN, C.-H. P. & BLACKWELDER, R. F. 1978 Large-scale motion in a turbulent boundary layer: a study using temperature contamination. *Journal of Fluid Mechanics* **89**, 1–31.
- CHUNG, D. & MCKEON, B. J. 2010 Large-eddy simulation of large-scale structures in long channel flow. *Journal of Fluid Mechanics* **661**, 341–364.
- CLAUSER, F. H. 1956 The turbulent boundary layer. *Advances in Applied Mechanics* **4**, 1–51.
- DAVIDSON, P. A., KANEDA, Y. & SREENIVASAN, K. R., ed. 2012 *Ten Chapters in Turbulence*. Cambridge UK: Cambridge University Press.

- DEGRAAFF, D. B. & EATON, J. K. 2000 Reynolds-number scaling of the flat-plate turbulent boundary layer. *Journal of Fluid Mechanics* **422**, 319–346.
- DUVVURI, S. & MCKEON, B. J. 2014 Phase relationships in presence of a synthetic large-scale in a turbulent boundary layer. In *44th AIAA Fluid Dynamics Conference, Atlanta GA*. Paper 2014-2883.
- DUVVURI, S. & MCKEON, B. J. 2015a Triadic scale interactions in a turbulent boundary layer. *Journal of Fluid Mechanics* **767**, R4.
- DUVVURI, S. & MCKEON, B. J. 2015b Small-scale phase organization through large-scale inputs in a turbulent boundary layer. In *9th International Symposium on Turbulence and Shear Flow Phenomena (TSFP), Melbourne, Australia*. Paper 3A-2.
- FAVRE, A. J., GAVIGLIO, J. J. & DUMAS, R. 1967 Structure of velocity spacetime correlations in a boundary layer. *Physics of Fluids* **10** (9), S138–S145.
- GANAPATHISUBRAMANI, B., HUTCHINS, N., MONTY, J. P., CHUNG, D. & MARUSIC, I. 2012 Amplitude and frequency modulation in wall turbulence. *Journal of Fluid Mechanics* **712**, 61–91.
- GUALA, M., HOMMEMA, S. E. & ADRIAN, R. J. 2006 Large-scale and very-large-scale motions in turbulent pipe flow. *Journal of Fluid Mechanics* **554**, 521–542.
- GUALA, M., METZGER, M. & MCKEON, B. J. 2011 Interactions within the turbulent boundary layer at high Reynolds number. *Journal of Fluid Mechanics* **666**, 573–604.
- GAD-EL HAK, M. 2000 *Flow Control: Passive, Active and Reactive Flow Management*. Cambridge UK: Cambridge University Press.
- HUSSAIN, A. K. M. F. & REYNOLDS, W. C. 1970 The mechanics of an organized wave in turbulent shear flow. *Journal of Fluid Mechanics* **41**, 241–258.
- HUSSAIN, A. K. M. F. & REYNOLDS, W. C. 1972 The mechanics of an organized wave in turbulent shear flow. Part 2. Experimental results. *Journal of Fluid Mechanics* **54**, 241–261.
- HUTCHINS, N. & MARUSIC, I. 2007a Large-scale influences in near-wall turbulence. *Philosophical Transactions of the Royal Society A* **365**, 647–664.
- HUTCHINS, N. & MARUSIC, I. 2007b Evidence of very long meandering features in the logarithmic region of turbulent boundary layers. *Journal of Fluid Mechanics* **579**, 1–28.

- HUTCHINS, N., MONTY, J. P., GANAPATHISUBRAMANI, B., NG, H. C. N. & MARUSIC, I. 2011 Three-dimensional conditional structure of a high-Reynolds-number turbulent boundary layer. *Journal of Fluid Mechanics* **673**, 255–285.
- HUTCHINS, N., NICKELS, T. B., MARUSIC, I. & CHONG, M. S. 2009 Hot-wire spatial resolution issues in wall-bounded turbulence. *Journal of Fluid Mechanics* **635**, 103–136.
- JACOBI, I. 2012 New perspectives on the impulsive roughness-perturbation of a turbulent boundary layer. PhD thesis, California Institute of Technology.
- JACOBI, I. & MCKEON, B. J. 2011*a* New perspectives on the impulsive roughness-perturbation of a turbulent boundary layer. *Journal of Fluid Mechanics* **677**, 179–203.
- JACOBI, I. & MCKEON, B. J. 2011*b* Dynamic roughness perturbation of a turbulent boundary layer. *Journal of Fluid Mechanics* **688**, 258–296.
- JACOBI, I. & MCKEON, B. J. 2013 Phase relationships between large and small scales in the turbulent boundary layer. *Experiments in Fluids* **54** (3), 1481.
- KIM, K. C. & ADRIAN, R. J. 1999 Very large-scale motion in the outer layer. *Physics of Fluids* **11** (2), 417–422.
- KOVASZNAY, L. S. G., KIBENS, V. & BLACKWELDER, R. F. 1970 Large-scale motion in the intermittent region of a turbulent boundary layer. *Journal of Fluid Mechanics* **41**, 283–325.
- LUHAR, M., SHARMA, A. S. & MCKEON, B. J. 2014 On the structure and origin of pressure fluctuations in wall turbulence: predictions based on the resolvent analysis. *Journal of Fluid Mechanics* **751**, 38–70.
- MARUSIC, I., MATHIS, R. & HUTCHINS, N. 2010*a* Predictive model for wall-bounded turbulent flow. *Science* **329**, 193–196.
- MARUSIC, I., MCKEON, B. J., MONKEWITZ, P. A., NAGIB, H. M., SMITS, A. J. & SREENIVASAN, K. R. 2010*b* Wall-bounded turbulent flows at high Reynolds numbers: Recent advances and key issues. *Physics of Fluids* **22** (6), 065103.
- MARUSIC, I., MONTY, J. P., HULTMARK, M. & SMITS, A. J. 2013 On the logarithmic region in wall turbulence. *Journal of Fluid Mechanics* **716**, R3.
- MASLOWE, S. A. 1986 Critical layers in shear flows. *Annual Review of Fluid Mechanics* **18**, 405–432.

- MATHIS, R., HUTCHINS, N. & MARUSIC, I. 2009a Large-scale amplitude modulation of the small-scale structures in turbulent boundary layers. *Journal of Fluid Mechanics* **628**, 311–337.
- MATHIS, R., MARUSIC, I., HUTCHINS, N. & SREENIVASAN, K. R. 2011 The relationship between the velocity skewness and the amplitude modulation of the small scale by the large scale in turbulent boundary layers. *Physics of Fluids* **23** (12), 121702.
- MATHIS, R., MONTY, J. P., HUTCHINS, N. & MARUSIC, I. 2009b Comparison of large-scale amplitude modulation in turbulent boundary layers, pipes, and channel flows. *Physics of Fluids* **21** (111703).
- MCKEON, B. J., CHUNG, D., DUVVURI, S. & JACOBI, I. (in preparation) Interactions between scales in wall turbulence: phase relationships, amplitude modulation and the importance of critical layers.
- MCKEON, B. J. & SHARMA, A. S. 2010 A critical-layer framework for turbulent pipe flow. *Journal of Fluid Mechanics* **658**, 336–382.
- MCKEON, B. J., SHARMA, A. S. & JACOBI, I. 2013 Experimental manipulation of wall turbulence: a systems approach. *Physics of Fluids* **25** (3), 031301.
- MILLIKAN, C. B. 1938 A critical discussion of turbulent flows in channels and circular tubes. In *Proceedings of the Fifth International Congress of Applied Mechanics*.
- MOARREF, R., SHARMA, A. S., TROPP, J. A. & MCKEON, B. J. 2013 Model-based scaling of the streamwise energy density in high-Reynolds-number turbulent channels. *Journal of Fluid Mechanics* **734**, 275–316.
- MONTY, J. P., HUTCHINS, N., NG, H. C. N., MARUSIC, I. & CHONG, M. S. 2009 A comparison of turbulent pipe, channel and boundary layer flows. *Journal of Fluid Mechanics* **632**, 431–442.
- MONTY, J. P., STEWART, J. A., WILLIAMS, R. C. & CHONG, M. S. 2007 Large-scale features in turbulent pipe and channel flows. *Journal of Fluid Mechanics* **589**, 147–156.
- NAGIB, H. M., CHAUHAN, K. A. & MONKEWITZ, P. A. 2007 Approach to an asymptotic state for zero pressure gradient turbulent boundary layers. *Philosophical Transactions of the Royal Society A* **365**, 755–770.
- PERRY, A. E. & CHONG, M. S. 1982 On the mechanism of wall turbulence. *Journal of Fluid Mechanics* **119**, 173–217.

- RAO, K. N., NARASIMHA, R. & NARAYANAN, M. A. B. 1971 The ‘bursting’ phenomenon in a turbulent boundary layer. *Journal of Fluid Mechanics* **48**, 339–352.
- REYNOLDS, W. C. & HUSSAIN, A. K. M. F. 1972 The mechanics of an organized wave in turbulent shear flow. Part 3. Theoretical models and comparisons with experiments. *Journal of Fluid Mechanics* **54**, 263–288.
- ROBINSON, S. K. 1991 Coherent motions in the turbulent boundary layer. *Annual Review of Fluid Mechanics* **23**, 601–639.
- ROSHKO, A. 1976 Structure of turbulent shear flows: a new look. *AIAA Journal* **14** (10), 1349–1357.
- SCHLATTER, P. & ÖRLU, R. 2010 Quantifying the interaction between large and small scales in wall-bounded turbulent flows: A note of caution. *Physics of Fluids* **22** (5), 051704.
- SCHLICHTING, H. 1968 *Boundary-Layer Theory*. New York: McGraw-Hill.
- SCHMID, P. J. & HENNINGSON, D. S. 2001 *Stability and Transition in Shear Flows*. New York: Springer-Verlag.
- SCHUBAUER, G. B. & SKRAMSTAD, H. K. 1947 Laminar boundary-layer oscillations and transition on a flat plate. *Journal of Research of the National Bureau of Standards* **38**, research paper 1722.
- SHARMA, A. S. & MCKEON, B. J. 2013 On coherent structure in wall turbulence. *Journal of Fluid Mechanics* **728**, 196–238.
- SMITS, A. J. & MARUSIC, I. 2013 The turbulent boundary layer. *Physics Today* **66** (9), 25–30.
- SMITS, A. J., MCKEON, B. J. & MARUSIC, I. 2011 High-Reynolds number wall turbulence. *Annual Review of Fluid Mechanics* **43**, 353–375.
- TAYLOR, G. I. 1938 The spectrum of turbulence. *Proceedings of the Royal Society of London A* **164** (919), 476–490.
- TENNEKES, H. & LUMLEY, J. L. 1972 *A First Course in Turbulence*. Cambridge MA: The MIT Press.
- TOWNSEND, A. A. 1976 *The Structure of Turbulent Shear Flow*. Cambridge UK: Cambridge University Press.
- VALLIKIVI, M., GANAPATHISUBRAMANI, B. & SMITS, A. J. 2015 Spectral scaling in boundary layers and pipes at very high Reynolds numbers. *Journal of Fluid Mechanics* **771**, 303–326.

- YEUNG, P. K. & BRASSEUR, J. G. 1991 The response of isotropic turbulence to isotropic and anisotropic forcing at the large scales. *Physics of Fluids A* **3** (5), 884–897.
- YEUNG, P. K., BRASSEUR, J. G. & WANG, Q. 1995 Dynamics of direct large-small scale couplings in coherently forced turbulence: concurrent physical- and fourier-space views. *Journal of Fluid Mechanics* **283**, 43–95.

Appendix A

A.1 Skewness and Amplitude Modulation Coefficient

Skewness Triple Sum

With the use of the following trigonometric identity

$$\cos(a) \cos(b) \cos(c) = \frac{1}{4} \{ \cos(-a + b + c) + \cos(a + b - c) + \cos(a - b + c) - \cos(a + b + c) \}, \quad (\text{A.1})$$

equation 3.4 is written as

$$\begin{aligned} \sigma^3 S = & \sum_{l=1}^{\infty} \sum_{m=1}^{\infty} \sum_{n=1}^{\infty} \frac{\alpha_l \alpha_m \alpha_n}{4} \times \\ & \{ \langle \cos[(-k_l + k_m + k_n)x + (-\phi_l + \phi_m + \phi_n)] \rangle + \langle \cos[(k_l + k_m - k_n)x + (\phi_l + \phi_m - \phi_n)] \rangle \\ & + \langle \cos[(k_l - k_m + k_n)x + (\phi_l - \phi_m + \phi_n)] \rangle - \langle \cos[(k_l + k_m + k_n)x + (\phi_l + \phi_m + \phi_n)] \rangle \}. \end{aligned} \quad (\text{A.2})$$

Noting that $\langle \cos(kx + \phi) \rangle = 0$ if $k \neq 0$, it is easy to see that the non-zero contributions from the above triple sum come from combinations of k_l, k_m, k_n only if they are triadically consistent. A distinction is made between the two types of triadic interactions:

- $k_l < k_m < k_n$ with $k_l + k_m = k_n$, *i.e.* sets of triads $\{k_l, k_m, k_n\}$ with $k_l \neq k_m \neq k_n$;
- $k_l = k_m = k_n/2$, *i.e.* pairs of wavenumbers $\{k_l, k_n\}$ with $k_n = 2k_l$.

For a given set of triadic wavenumbers $\{k_l, k_m, k_n\}$, we get six non-zero contributions of the form $\cos(\phi_l + \phi_m - \phi_n)$ from the triple sum, and only three non-zero contributions when wavenumbers pairs $\{k_l, k_n\}$ with $k_n = 2k_l$ are considered. This gives the multiplicative factors of 6 and 3 for the first and second set of RHS terms respectively in equation 3.5.

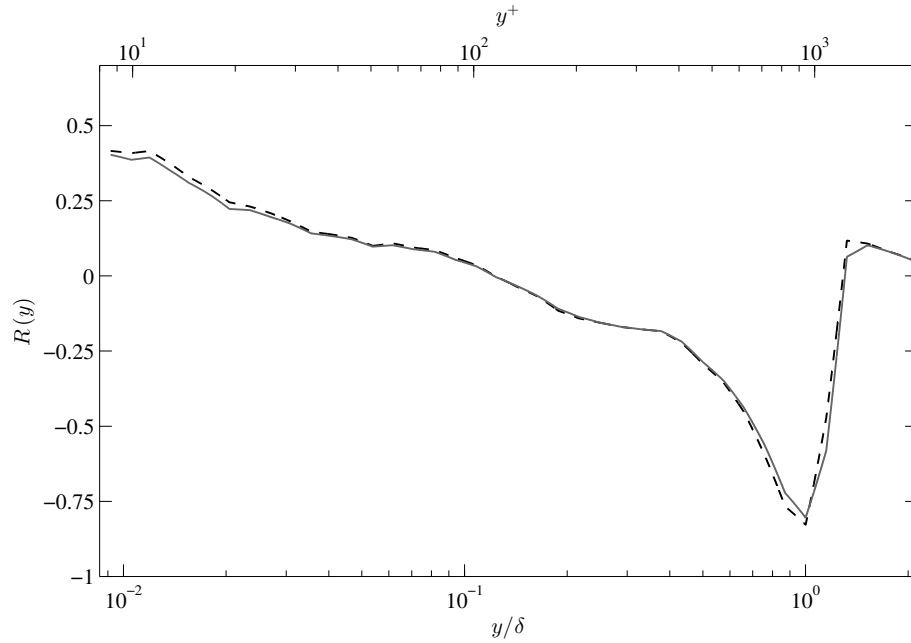


FIGURE A.1: A comparison of the amplitude modulation coefficient R calculated using two different envelope functions for the same experimental data set (with a single synthetic large-scale mode at $x = 2.7 \delta_1$). Dashed curve was obtained using $\sqrt{\mathcal{E}(x)}$ as the envelope function following [Mathis et al. \(2009a\)](#), and the solid curve was obtained using $\mathcal{E}(x)$ per the present description.

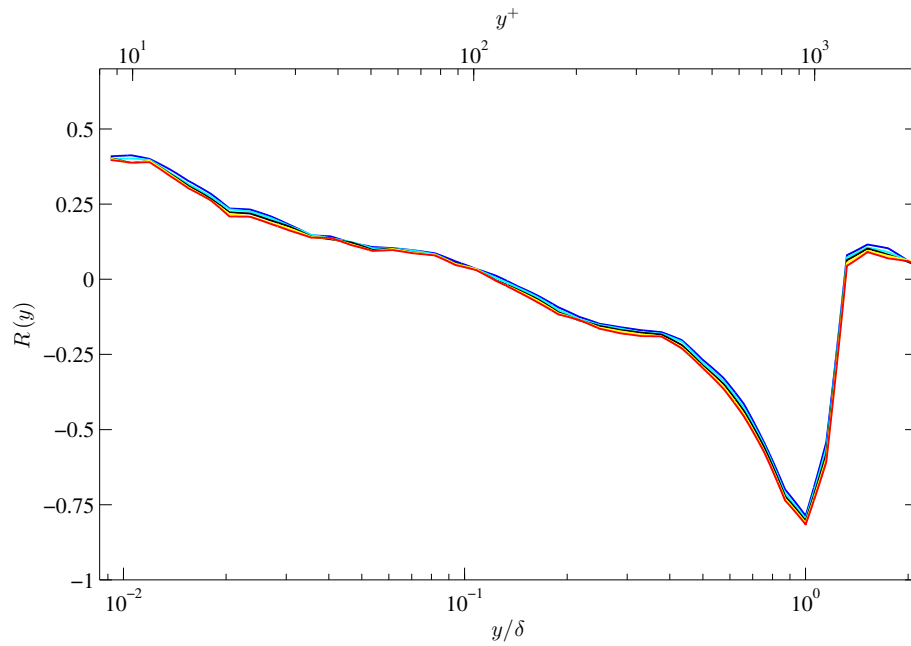


FIGURE A.2: A comparison of the amplitude modulation coefficient R calculated using five different large and small scale filter cut-offs (λ_γ) for the same experimental data set (with a single synthetic large-scale mode at $x = 2.7 \delta_1$). The figure demonstrates the robustness of R to the exact choice of the filter cut-off. Plot legend: blue curve, $\lambda_\gamma = 4 \delta$; cyan curve, $\lambda_\gamma = 4.5 \delta$; black curve, $\lambda_\gamma = 5 \delta$; yellow curve, $\lambda_\gamma = 5.5 \delta$; red curve, $\lambda_\gamma = 6 \delta$.

Envelope Function \mathcal{E} and Covariance $\langle \mathcal{E}_L u_L \rangle$

Noting that $\mathcal{H}[\cos(x)] = \sin(x)$, where $\mathcal{H}(\cdot)$ denotes the Hilbert transform, we have from equation 3.6

$$\mathcal{H}[u_S(x)] = \alpha_\gamma \sin(k_\gamma x + \phi_\gamma) \dots + \alpha_m \sin(k_m x + \phi_m) \dots + \alpha_n \sin(k_n x + \phi_n) + \dots \quad (\text{A.3})$$

The envelope function \mathcal{E} for the small-scale signal u_S is then given by

$$\begin{aligned} \mathcal{E}(x) &= u_S^2(x) + \mathcal{H}^2(x) \\ &= \sum_{m=\gamma}^{\infty} \alpha_m^2 + \sum_{\substack{\forall m,n \\ k_\gamma < k_m < k_n}} 2\alpha_m \alpha_n \{ \sin(k_m x + \phi_m) \sin(k_n x + \phi_n) + \cos(k_m x + \phi_m) \cos(k_n x + \phi_n) \}. \end{aligned} \quad (\text{A.4})$$

Removing the mean term from the above expression and using the trigonometric identity $\sin(a) \sin(b) + \cos(a) \cos(b) = \cos(b - a)$, \mathcal{E} is re-written as

$$\mathcal{E}(x) = \sum_{\substack{\forall m,n \\ k_\gamma < k_m < k_n}} 2\alpha_m \alpha_n \cos[(k_n - k_m)x + (\phi_n - \phi_m)]. \quad (\text{A.5})$$

Prior to correlating $\mathcal{E}(x)$ with $u_L(x)$, we large-scale-pass $\mathcal{E}(x)$ through the spatial filter with cut-off at k_γ . This implies that filtered $\mathcal{E}(x)$, denoted by $\mathcal{E}_L(x)$, and $u_L(x)$ have spectral content in the same wavenumber range, *i.e.* 0 to k_γ . $\mathcal{E}_L(x)$ is then written as

$$\mathcal{E}_L(x) = \sum_{\substack{\forall m,n \\ 0 < k_n - k_m < k_\gamma}} 2\alpha_m \alpha_n \cos[(k_n - k_m)x + (\phi_n - \phi_m)]. \quad (\text{A.6})$$

We now correlate $\mathcal{E}_L(x)$ and $u_L(x)$; their covariance is given by

$$\langle \mathcal{E}_L u_L \rangle = \langle \left\{ \sum_{\substack{\forall m,n \\ 0 < k_n - k_m < k_\gamma}} 2\alpha_m \alpha_n \cos[(k_n - k_m)x + (\phi_n - \phi_m)] \right\} \left\{ \sum_{l=1}^{\gamma-1} \alpha_l \cos(k_l x + \phi_l) \right\} \rangle. \quad (\text{A.7})$$

Using the trigonometric identity $2 \cos(a) \cos(b) = \cos(a - b) + \cos(a + b)$, we have

$$\begin{aligned}
\langle \mathcal{E}_L u_L \rangle = & \\
& \sum_{\substack{\forall l, m, n | \\ 0 < k_l < k_\gamma \\ 0 < k_n - k_m < k_\gamma}} \langle \alpha_l \alpha_m \alpha_n \{ \cos[(k_l + k_m - k_n)x + (\phi_l + \phi_m - \phi_n)] + \cos[(k_l - k_m + k_n)x + (\phi_l - \phi_m + \phi_n)] \} \rangle.
\end{aligned} \tag{A.8}$$

Noting again that $\langle \sin(kx + \phi) \rangle = 0$ if $k \neq 0$, and that $k_l - k_m + k_n$ is always positive, it is easily seen that the non-zero contributions to the covariance come from combinations of k_l, k_m, k_n only if they are triadically consistent, *i.e.* $k_n - k_m = k_l$. Hence, the covariance is written as a triple sum among all triadic sets of k_l, k_m, k_n with the condition that $0 < k_l < k_\gamma$ and $k_m, k_n > k_\gamma$

$$\langle \mathcal{E}_L u_L \rangle = \sum_{\substack{\forall l, m, n | \\ k_n - k_m = k_l \\ 0 < k_l < k_\gamma \\ k_m, k_n > k_\gamma}} \alpha_l \alpha_m \alpha_n \cos(\phi_l + \phi_m - \phi_n). \tag{A.9}$$

Equation 3.8 then follows from the above expression for the covariance.

A comparison of the amplitude modulation coefficient R calculated using two slightly different techniques discussed in section 3.3.2 is presented in figure A.1. As expected, differences in the values of R are minimal. The robustness of R to the exact choice of the filter cut-off (λ_γ), mentioned in section 3.3.4, is demonstrated in figure A.2 using experimental data.

A.2 Triadic Small-Scale Envelope

For a specific set of small-scale triadic wavenumbers k_m, k_n with a velocity signal $u_{mn} = \alpha_m \cos(k_m x + \phi_m) + \alpha_n \cos(k_n x + \phi_n)$, an envelope function is written as

$$\begin{aligned}
A_{mn}(x) &= u_{mn}^2(x) + \mathcal{H}^2(x) \\
&= \alpha_m^2 + \alpha_n^2 + 2\alpha_m \alpha_n \{ \cos(k_m x + \phi_m) \cos(k_n x + \phi_n) + \sin(k_m x + \phi_m) \sin(k_n x + \phi_n) \}.
\end{aligned} \tag{A.10}$$

Removing the mean terms and using the triadic condition, the above expression gives equation 3.11

$$\begin{aligned}
A_{mn}(x) &= 2\alpha_m \alpha_n \cos[(k_n - k_m)x + \phi_n - \phi_m] \\
&= 2\alpha_m \alpha_n \cos[\tilde{k}x + \phi_n - \phi_m].
\end{aligned}$$

Now considering the quantity $\widetilde{u_S^2} = \widetilde{\mathcal{E}}$ (square of the small-scale signal u_S phase-averaged with respect to the input forcing that generates the synthetic scale). Recollecting u_S from equation 3.6 as

$$u_S = \alpha_\gamma \cos(k_\gamma x + \phi_\gamma) + \dots + \alpha_m \cos(k_m x + \phi_m) \dots + \alpha_n \cos(k_n x + \phi_n) \dots,$$

we have

$$\begin{aligned} u_S^2 &= \sum_{\substack{\forall m,n \\ k_\gamma < k_m, k_n}} \alpha_m \alpha_n \cos(k_m x + \phi_m) \cos(k_n x + \phi_n) \\ &= \sum_{\substack{\forall m,n \\ k_\gamma < k_m, < k_n}} \alpha_m \alpha_n \{ \cos[(k_n - k_m)x + (\phi_n - \phi_m)] + \cos[(k_n + k_m)x + (\phi_n + \phi_m)] \}. \end{aligned} \quad (\text{A.11})$$

And finally, the phase-averaging procedure picks out from u_S^2 the \widetilde{k} components that arise when the triadic condition $\widetilde{k} = k_n - k_m$ is satisfied. This gives equation 3.12

$$\widetilde{\mathcal{E}} = \sum_{\substack{\forall m,n \\ k_n - k_m = \widetilde{k} \\ k_m, k_n > k_\gamma}} \alpha_m \alpha_n \cos(\widetilde{k}x + \phi_n - \phi_m).$$

Appendix B

B.1 Forcing from Two-Mode Interactions

Consider the three-dimensional velocity field $\mathbf{u}_{12} = (u_{12}, v_{12}, w_{12})$ consisting of only two scales – the 2D forcing modes at wavenumbers $\tilde{\mathbf{k}}_1$ and $\tilde{\mathbf{k}}_2$. We write

$$\begin{aligned} u_{12} &= \tilde{u}_1 + \tilde{u}_2 &= \frac{1}{2} \hat{u}_1(y) e^{i(\tilde{k}_{x1}x - \tilde{\omega}_1 t)} + \frac{1}{2} \hat{u}_2(y) e^{i(\tilde{k}_{x2}x - \tilde{\omega}_2 t)} + \text{c.c.}, \\ v_{12} &= \tilde{v}_1 + \tilde{v}_2 &= \frac{1}{2} \hat{v}_1(y) e^{i(\tilde{k}_{x1}x - \tilde{\omega}_1 t)} + \frac{1}{2} \hat{v}_2(y) e^{i(\tilde{k}_{x2}x - \tilde{\omega}_2 t)} + \text{c.c.}, \\ w_{12} &= 0. \end{aligned} \tag{B.1}$$

The interaction between the two modes (scales) results in forcing $\mathbf{f} = -(\mathbf{u}_{12} \cdot \nabla)\mathbf{u}_{12}$ which consists of two triadic components at wavenumbers $\tilde{\mathbf{k}}_3 = \tilde{\mathbf{k}}_1 + \tilde{\mathbf{k}}_2$ and $\tilde{\mathbf{k}}_4 = \tilde{\mathbf{k}}_1 - \tilde{\mathbf{k}}_2$,

$$\mathbf{f} = - \left(\left\{ u_{12} \frac{\partial u_{12}}{\partial x} + v_{12} \frac{\partial u_{12}}{\partial y} \right\}, \left\{ u_{12} \frac{\partial v_{12}}{\partial x} + v_{12} \frac{\partial v_{12}}{\partial y} \right\}, 0 \right) = \tilde{\mathbf{f}}_{\mathbf{k}_3} + \tilde{\mathbf{f}}_{\mathbf{k}_4}.$$

The two components $\tilde{\mathbf{f}}_{\mathbf{k}_3}$ and $\tilde{\mathbf{f}}_{\mathbf{k}_4}$ of \mathbf{f} above follow from equation B.1 as

$$\begin{aligned} -\tilde{\mathbf{f}}_{\mathbf{k}_3} &= \frac{1}{4} \left(\left\{ i \hat{u}_1 \hat{u}_2 (\tilde{k}_{x1} + \tilde{k}_{x2}) + (\hat{u}'_2 \hat{v}_1 + \hat{u}'_1 \hat{v}_2) \right\}, \left\{ i (\tilde{k}_{x2} \hat{u}_1 \hat{v}_2 + \tilde{k}_{x1} \hat{u}_2 \hat{v}_1) + (\hat{v}_1 \hat{v}_2)' \right\}, 0 \right) e^{i(\tilde{k}_{x3}x - \tilde{\omega}_3 t)} + \text{c.c.} \\ -\tilde{\mathbf{f}}_{\mathbf{k}_4} &= \frac{1}{4} \left(\left\{ i \hat{u}_1 \hat{u}_2^* (\tilde{k}_{x1} - \tilde{k}_{x2}) + (\hat{v}_1 \hat{u}'_2 + \hat{u}'_1 \hat{v}_2^*) \right\}, \left\{ i (\tilde{k}_{x1} \hat{u}_2^* \hat{v}_1 - \tilde{k}_{x2} \hat{u}_1 \hat{v}_2^*) + (\hat{v}_1 \hat{v}_2^*)' \right\}, 0 \right) e^{i(\tilde{k}_{x4}x - \tilde{\omega}_4 t)} + \text{c.c.} \end{aligned}$$

Note that $(\cdot)'$ and $(\cdot)^*$ in the above expressions denote $d(\cdot)/dy$ and complex conjugate respectively. $\tilde{\mathbf{f}}_{\mathbf{k}_3}$ and $\tilde{\mathbf{f}}_{\mathbf{k}_4}$ calculated using experimental data for $\tilde{u}_1, \tilde{v}_1, \tilde{u}_2, \tilde{v}_2$ are shown in figures [4.13](#) and [4.14](#).